



Cite this: *Energy Adv.*, 2022, 1, 793

Received 5th May 2022,
Accepted 2nd October 2022

DOI: 10.1039/d2ya00106c

rsc.li/energy-advances

Recent progress in ZnCo_2O_4 and its composites for energy storage and conversion: a review

Josué M. Gonçalves, *^a Matheus I. da Silva,^a Murillo N. T. Silva,^b Paulo R. Martins, ^c Edson Nossol,^b Henrique E. Toma ^a and Lucio Angnes *^a

Transition metal oxides have attracted growing attention for application in energy storage and conversion technologies. In particular, spinel-based materials, such as ZnCo_2O_4 , exhibit structures suitable for performing as multifunctional electrodes in energy devices. In fact, great efforts have been dedicated to the design of micro- and nanomaterials based on ZnCo_2O_4 , using different synthesis approaches and controlled conditions. Consequently, interesting morphologies and structures have been recently obtained, exhibiting outstanding electrochemical performance. Hence, in this review we report a comprehensive survey of the progress of multifunctional ZnCo_2O_4 -based materials, focusing on the development of supercapacitor devices and batteries. The top 10 electrode materials for each application are highlighted, including key findings in the development of slurry-cast or binder-free electrodes. In addition, the main strategies in the design of ZnCo_2O_4 -based electrocatalysts for the oxygen evolution reaction (OER) and hydrogen evolution reaction (HER) are reviewed, including electrocatalysts capable of performing tetra-electron oxygen reduction reactions (ORRs).

1. Introduction

Clean, sustainable and efficient technologies for energy production, conversion, and storage are becoming crucial for the energy crisis which is confronting the world.¹ In this regard, the development of new electrode materials may play a primary role, impacting the performance of these energy systems.¹ Therefore, materials chemistry is becoming the key to the design of systems that can overcome the current challenges of our modern society. Among the emerging challenges, one can highlight the development of electrode materials capable of using solar energy and/or electricity to promote the oxygen evolution reaction (OER) and the hydrogen evolution reaction (HER) by electrochemical and/or photochemical water-splitting processes, respectively. This corresponds to the conversion of renewable energy into a high-energy-content chemical species, approaching the ultimate clean energy resource due to the zero emission of carbonaceous species.² Another challenging step is how to store energy more efficiently, especially in a faster way, *e.g.*, by assembling devices with high energy and power density. This is the case of hybrid supercapacitors (HSCs) combining

the outstanding power density of supercapacitive materials with the high-energy density of battery-type materials.³

Among the emerging materials recently studied, transition metal oxides (TMOs) deserve special consideration because of their rich redox chemistry and abundant density of active sites, in addition to their low cost, environmental friendliness, and excellent electrochemical performance.^{4,5} In fact, special attention has been given to spinel materials with a bimetallic oxide structure of the typical chemical formula AB_2O_4 . Spinels consist of cation A, typically charged as 2+, in tetrahedral sites (T_d), and cation B charged as 3+ occupying octahedral sites (O_h).⁶ The interest in this type of material is justified by its higher electrochemical activity, electrical conductivity, and more abundant redox reactions, compared with monometallic oxides of the types A_3O_4 and B_3O_4 .^{7,8}

It is also important to mention that among various spinel-type oxides, structures based on bimetallic cobaltite (MCo_2O_4 , where M = Mg, Ni, Zn, Cu, Fe, and Mn) have been most widely reported,⁹ as recently summarized in several review articles. In particular, one can highlight the use of nickel cobaltite spinel (NiCo_2O_4) in different applications such as in supercapacitors,^{9,10} batteries¹¹ and sensors.¹² Similarly, Gonçalves *et al.*⁸ summarized the main advances in MnCo_2O_4 -based materials for energy applications and the main strategies used for the design of these materials, including HSCs, LIBs and MABs, as well as the advancements achieved as electrocatalysts for water-splitting, more specifically for the HER and OER. Similarly, Wu and colleagues¹³ highlighted the current research

^a Instituto de Química, Universidade de São Paulo, Av. Prof. Lineu Prestes 748, 05508-000, São Paulo-SP, Brazil. E-mail: josuemartins@usp.br, luangnes@iq.usp.br

^b Institute of Chemistry, Federal University of Uberlândia, Av. João Naves de Ávila 2121, 38400-902, Uberlândia-MG, Brazil

^c Instituto de Química, Universidade Federal de Goiás, Av. Esperança s/n, 74690-900, Goiânia-GO, Brazil



progress regarding synthetic strategies for MgCo_2O_4 -based electrode materials and their applications in supercapacitors, Li-ion batteries, Mg-ion batteries, and some other rechargeable ion batteries. J. Sun, C. Xu & H. Chen¹⁴ reviewed the synthesis of CuCo_2O_4 -based electrode materials and their applications in supercapacitors, while Gao *et al.*¹⁵ briefly summarized the recent applications of FeCo_2O_4 (and CoFe_2O_4) in energy storage and conversion, as well as the current understanding of the mechanisms and especially the relevance of morphologies and structures and composites to the electrochemical performance.

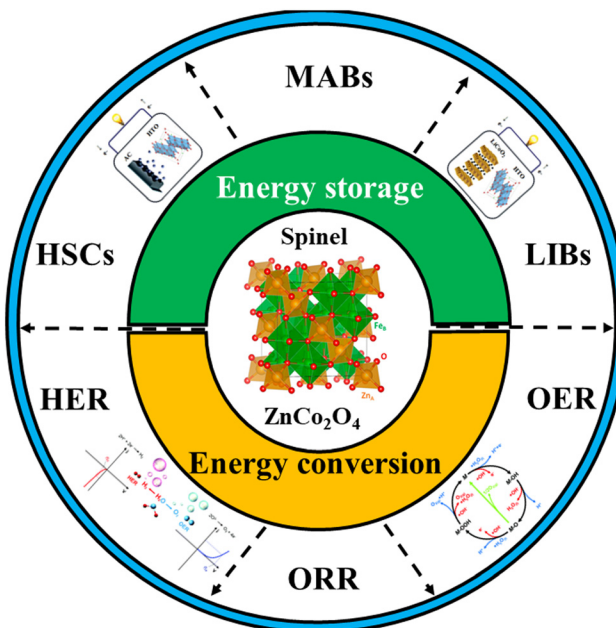
As shown above, several review articles show the progress made for Mg, Mn, Fe, Cu and especially Ni cobaltite. However, to our knowledge, more than 800 papers report the syntheses and/or use of ZnCo_2O_4 spinel for various applications, including sensor, and energy conversion and storage applications. Its multi-functionality and excellent electrochemical properties are closely related to its structure which presents a regular spinel structure where Zn^{2+} only replaces Co^{2+} in the T_d sites in Co_3O_4 , leaving the Co^{3+} content in the O_h sites unchanged, while Ni and Mn mainly occupy O_h sites in NiCo_2O_4 and MnCo_2O_4 .¹⁶ In fact, the effect of the oxidation state and cation distribution in the spinel on the electrocatalytic activity for the OER in an alkaline solution has been studied, and a comparison of the electrochemical and physicochemical behavior of MCo_2O_4 (where $\text{M} = \text{Mn, Fe, Co, Ni, and Zn}$) was made by M. Harada, F. Kotegawa, & M. Kuwa.¹⁶ Interestingly, their catalytic activity for the OER follows the order: $\text{ZnCo}_2\text{O}_4 > \text{NiCo}_2\text{O}_4 > \text{FeCo}_2\text{O}_4 > \text{Co}_3\text{O}_4 > \text{MnCo}_2\text{O}_4$. According to the authors, the active sites for the OER are M^{3+} species in the octahedral site, and their activities are significantly dependent on the $\text{Co}^{3+}/\text{Co}^{2+}$ and $\text{M}^{3+}/\text{M}^{2+}$ content ratios in the octahedral site as demonstrated according to XPS and *in situ* X-ray absorption fine structure (XAFS) measurements, demonstrating the importance of the presence of Zn^{2+} ions in ZnCo_2O_4 .¹⁶ Complementarily, ZnCo_2O_4 is a promising energy storage material which shows advantageous properties, including low cost, low-toxicity, different morphologies, high electrical conductivity,^{17,18} and high theoretical capacity in comparison with unitary ZnO and CoO and binary Co_3O_4 .¹⁷

Inspired by the above considerations, and despite being the second most reported cobaltite, as far as we know, there is no review work summarizing recent progress in ZnCo_2O_4 in energy applications. Therefore, in this review article we focus on ZnCo_2O_4 and its composites as electrode materials for energy technologies, including the main strategies used for the design (Scheme 1) of HSCs, LIBs and MABs, as well as the advancements as electrocatalysts for water-splitting (HER and OER) and the ORR. The pros and cons of using this spinel in the different devices are critically discussed, encompassing the perspectives and possible future directions.

2. Water-splitting and electrochemical energy storage systems

2.1. Water-splitting

Electrocatalytic water-splitting is an effective way to produce hydrogen with high purity.²² The overall reaction includes two



Scheme 1 Applications of ZnCo_2O_4 -based materials. Reproduced with permission.¹⁹ Copyright © 2018, The Author(s). Creative Commons CC BY license. Reproduced with permission.²⁰ Copyright Royal Society of Chemistry, 2017. Reproduced with permission.²¹ Copyright: © 2021 by the authors. Licensee MDPI, Basel, Switzerland (CC BY).

half reactions, *e.g.*, HER and OER, taking place, respectively, at the cathode and the anode,²³ as shown in Fig. 1A. In addition, the water splitting reactions are dependent on the pH, as expected for reactions involving protons,²³ as demonstrated by the equations presented in Fig. 1B. For instance, for the HER, there are two main steps on the electrode surface, described by the Volmer–Heyrovsky and Volmer–Tafel mechanisms proposed for acidic and basic solutions²⁴ (Fig. 1C). On the other hand, the OER is a more complex, requiring a high energy to overcome the sluggish kinetic barrier associated with the four-electron transfer process, and involves a larger overpotential²⁵ (Fig. 1C).

The electrocatalytic performance is usually measured by linear sweep voltammetry (LSV), cyclic voltammetry (CV)²⁵ and electrochemical chrono-methods where several parameters are used to classify catalysts according to their performance, and even to unravel the reaction mechanisms. Among the electrochemical activity criteria, the overpotential (η), Tafel slope and stability are the most used ones to study the performance of electrocatalysts based on metal oxides/hydroxides.

The overpotential (η) is one of the essential criteria to evaluate the activity of electrocatalysts. It represents the difference between the potentials for achieving a specific current density and the onset potential to start the reaction (HER = 0 V and OER = 1.23 V).²⁵ Generally, the overpotentials at a current density of 10 mA cm^{-2} (η_{10}) are used to compare the electrocatalytic activity between different catalysts. This corresponds to the equivalent efficiency of 12.3% for photoelectrochemical water splitting.²⁵ In practice, a catalyst providing an overpotential in the range of 300–400 mV is considered to be an excellent



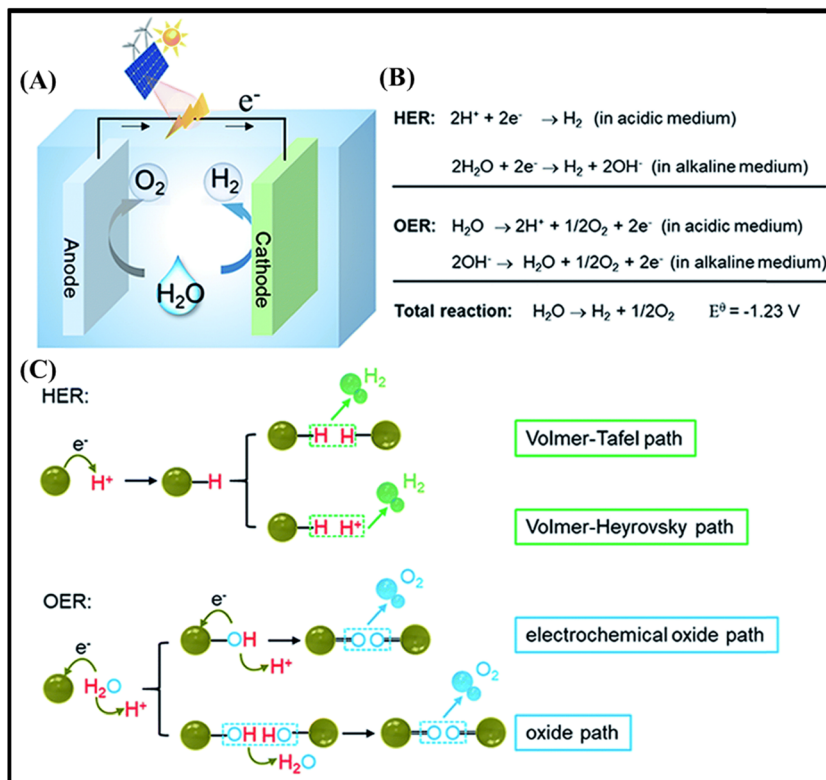


Fig. 1 (A) Scheme of a conventional water electrolyzer. (B) Water splitting reactions under acidic and alkaline conditions. (C) Proposed mechanisms of the HER and OER in an acidic aqueous solution. Reproduced with permission.²⁶ Copyright Marketplace™, Royal Society of Chemistry.

catalyst for the OER.^{27,28} However, η_{10} has a great influence on the loading mass even considering the same geometrical area; thus it cannot be the only criterion to evaluate the activity.²⁵ In this regard, Tafel analysis provides additional information to understand the reaction kinetics and mechanism, such as the magnitude of the slope, which helps in establishing the rate-determining step and the response sensitivity.²⁷ For instance, Tafel slopes of 120, 40 and 30 mV dec⁻¹ were observed, respectively, for the Volmer, Heyrovsky and Tafel determining rate steps. The smaller value of the Tafel slope means a faster electron-transfer kinetics of the electrocatalyst.^{22,24,25}

In addition to low overpotential and Tafel slope values, a good electrocatalyst should also be stable for long periods of time, under operating conditions. This evaluation can be performed by different techniques, including continuous CV cycling and LSV. The measurements allow comparing the overpotentials before and after cycling.²⁵ Another way to obtain information about the stability of electrocatalysts is by galvanostatic or potentiostatic electrolysis, registering the variation of potential or current density.²⁵

In summary, the overpotential (η), Tafel slope and stability are the main criteria to categorize electrocatalysts based on $ZnCo_2O_4$, for the OER and HER.

2.2. Electrochemical energy storage systems

In an effort to overcome past limitations, recent years have seen intense research efforts in energy storage areas, such as fuel

cells, capacitors, supercapacitors, and batteries. Electrochemical energy storage systems (EESs) play a critical role in renewable energy integration applications. They serve as energy sources to provide power supply and/or energy buffers to improve efficiency and the overall economy. This has triggered intensive research efforts in the past three decades, which have resulted in the advent of modern EESs such as batteries and supercapacitors.²⁹⁻³¹

2.2.1. Supercapacitor materials and devices. An important point that should be clarified in the initial evaluation of electrode materials is whether their electrochemical data correspond to a battery or a supercapacitor. Electrodes with a capacitor-like behavior present cyclic voltammograms (CVs) and linear potential responses during constant-current discharging (Fig. 2A–C). In contrast, the battery-type electrode presents CVs with defined oxidative and reductive peaks (Fig. 2G and H) and flat (plateau) galvanostatic charge/discharge (GCD) profiles (Fig. 2I). One criterion that could help the identification of the electrode's nature is the analysis of current *versus* scan rate curves. For battery-type materials, the peak current (i) will be proportional to the square root of the scanning rate ($i \sim v^{1/2}$), whereas for a capacitor-like electrode the current will be proportional to the scan rate ($i \sim v$).³²

Distinct from conventional capacitors, supercapacitors store charges electrochemically but show high-energy density compared to the former, with high rate capability and excellent cycling stability. According to their charge storage mechanisms,

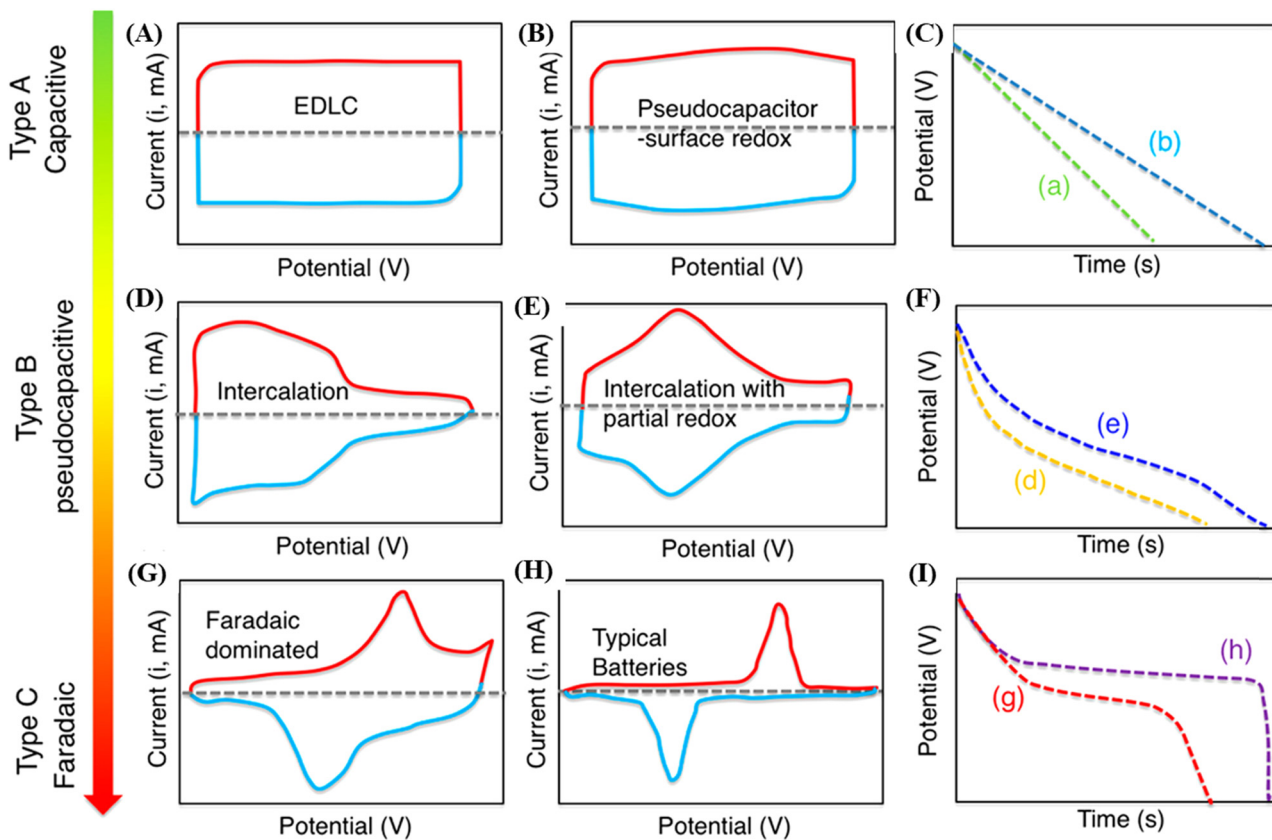


Fig. 2 Illustrative cyclic voltammograms (A, B, D, E, G and H) and the corresponding GCD curves (C, F and I) for different types of energy-storage materials. Electrochemical double-layer capacitors: CV profile (A) and the corresponding discharge curve (C). A pseudocapacitive electrode could present an electrochemical response of one, or a mix, of the following categories: (B and C) surface redox materials and (D-F) intercalation-type materials. Electrochemical profiles in (G-I) correspond to battery-like materials. Reproduced with permission.³² Copyright © 2018 American Chemical Society.

supercapacitors are divided into two categories, namely, electrochemical double-layer capacitors (EDLCs) and pseudocapacitors.³³ In EDLCs, the electrochemical behavior is due to the storage of charges at the electrode/electrolyte interface by establishing electrochemical double layers through a non-faradaic process (Fig. 2A and C.a). In pseudocapacitors, the electrochemical behavior in terms of current is neither totally capacitive nor entirely faradaic (like batteries). These electrodes present fast and reversible oxidation/reduction reactions through either intercalation or surface ion processes and quasi-rectangular CVs and quasi-linear GCD curves.³⁴ In surface-redox pseudocapacitors, the charge storage is mostly assigned to the charge transfers occurring at the surface of the material. As can be seen in Fig. 2B and C.b, the CV and the GCD characteristics for surface-redox pseudocapacitors present the linear dependency of the charge storage over the entire potential window, storing charges through surface faradaic and double layer mechanisms. Intercalation-type materials involve the core of the electrode materials and are expressed by the intercalation of charges between layers or in channels originating from the faradaic reaction and lack of phase changes during cycling (Fig. 2D-F).³⁵

EDLCs can reach fast charging/discharging rates and high cycling stability. However, the energy density of this type of material is relatively low, due to the deficient contact at the

electrode/electrolyte interface. On the other hand, the capacitance of pseudocapacitors is attributed to the fast and reversible redox process of materials, such as some transition metal oxides/hydroxides and conducting polymers. Hence, pseudocapacitors can provide higher specific capacitance but present lower power density,² due to the low conductivity of pseudocapacitive materials. In this way, one strategy to increase the performance of electrodes is the preparation of nanocomposites containing carbon structures.³⁶

The configuration of conventional supercapacitors is based on button cells or spiral-wound designs, which are composed of two collectors, two electrodes, and a separator, all soaked in electrolyte.³⁷ Distinct from the case of conventional supercapacitors, the development of materials in smart configurations (films, fibers, and micro-scale supercapacitors) has increased, aiming for the construction of thin, flexible, and even foldable devices. Thin-film electrodes are prepared with a layer of active material with its thickness varying from nanometers to micrometers, resulting in short charge and ion transport distances, and thus promoting fast physical or chemical processes during charge storage.³⁸ Fiber supercapacitors are commonly designed like 1D wires with diameters varying from micrometers to millimeters and constructed based on parallel, twisted, coaxial, or woven structures.³⁹ Micro-supercapacitors generally consist of a vertical structure composed

of two electrodes and electrolyte sandwiched in the middle of both or, in the case of the in-plane interdigital device architecture, electrodes are separated by an insulated gap, with no need for separators in the construction of the device. The electrolyte is subsequently deposited on the top of devices to guarantee ion transport between electrodes. The total size of micro-supercapacitors could be in the order of millimeters.^{36,40}

2.2.2. Rechargeable batteries. Unlike capacitors and supercapacitors, battery cells have high specific capacity values and high volumetric and gravimetric energy density values. In battery electrodes, during charging, ions are deintercalated (extracted) from the cathode and diffuse into the anode *via* the electrolyte medium, which is a conductor for ions and an insulator for the electrons generated at the cathode, while the electrons reach the anode *via* an external circuit, whereas discharging reverses this process. This is followed by faradaic charge transfer processes to generate the energy capacity (mA h kg⁻¹). Thus, the specific capacity obtained in battery electrodes is limited by solid-state ion diffusion, exhibiting relatively poor kinetics; however, the use of the entire bulk of the electrode for charge storage leads to very high energy density.^{29,41-43}

Among a number of different energy storage technologies, metal-ion batteries, in particular lithium-ion batteries (LIBs), have recently been accepted as the leading candidate for commercial EESSs. LIBs, as the main power source, dominate the portable device market due to their high energy density, high output voltage, long life and environmentally friendly operation.^{31,44} It is important to mention that many review works already published highlighting recent progress,⁴⁵⁻⁴⁷ issues and challenges facing rechargeable LIBs,⁴⁸ as well as rechargeable sodium-ion batteries (SIBs) as potential alternatives to current LIBs,⁴⁹ which can be used to obtain more detailed information about these EESSs.

On the other hand, metal-air batteries (MABs) are a family of electrochemical cells powered by metal oxidation and oxygen reduction; in this system oxygen is used as the active cathode material. This oxygen is obtained from air, which diffuses into the electrolyte from the atmosphere and undergoes reduction at the cathode, exhibiting a great advantage regarding theoretical energy density, which is about 3–30 times higher than those of commercial LIBs.⁵⁰⁻⁵²

In typical continuum-based models, the cathode material is considered as a porous medium and the structure is represented by several parameters, such as porosity, permeability, and tortuosity.⁵² In addition, it is necessary to design oxygen electrode catalysts with special structures for use in MABs to overcome the sluggish kinetics of the oxygen reduction reaction (ORR) and the oxygen evolution reaction (OER).⁵³⁻⁵⁵

3. ZnCo₂O₄-based materials for energy storage applications

3.1. ZnCo₂O₄-based electrode materials for supercapacitive applications

One of the best electrochemical performances is observed for RuO₂ as a supercapacitor electrode material, exhibiting a high

specific capacitance of 1580 F g⁻¹. However, because of its high cost and element scarcity, it becomes necessary to seek environmentally friendly and low-cost alternative electrode materials. Recently, transition metal oxides (TMOs) such as MnO₂, NiO, and Co₃O₄ have been studied as promising electrode materials for supercapacitor applications,⁵⁶ especially those based on doped-Co₃O₄. The bimetallic oxide ZnCo₂O₄ has recently attracted much attention because of its excellent electrochemical properties, with lower activation energy, higher conductivity and electroactivity in comparison with pristine Co₃O₄. It also exhibits high theoretical capacitance (2604 F g⁻¹), and is environmentally compatible and a cost-effective and abundant material. In addition, ZnCo₂O₄ presents a p-type semiconducting nature, which influences the electrical conductivity of the material, and shares the same Co₃O₄ spinel crystal structure. The replacement of Co²⁺ ions with Zn²⁺ ions, with Zn occupying the tetrahedral sites and Co occupying the octahedral sites, results in much richer redox reactions. However, ZnCo₂O₄ has the disadvantage of exhibiting an intrinsically poor electrical conductivity, involving large volume changes through the charge/discharge processes. This leads to some intrinsic electrical insulation, showing rapidly fading capacitance at higher current densities and during charge/discharge cycles, thus usually presenting low rate-capability and cycling stability.^{57,58}

Therefore, to overcome these limitations, rational design of suitable electrode materials is imperative, since the electrochemical performance strongly depends on their mechanical properties. To surpass the limitations of ZnCo₂O₄-based electrodes for supercapacitor applications, it is important to seek for an optimized morphology that can provide high active surface area, short lengths and high rates of ion and electron diffusion. Plenty of redox sites should be available. For this reason, pristine ZnCo₂O₄ has been synthesized as micro-particles,⁵⁹ microsheets,⁶⁰ microspheres,⁶¹⁻⁶⁴ microflowers,^{65,66} nanoparticles (NPs),^{67,68} nanocubes,⁶⁹ nanosheets,⁷⁰⁻⁷³ nanoplates,⁵⁶ nanoflowers,⁷⁴ nanorods,⁷⁵ nanospheres,⁷⁶ and nanotubes⁷⁷ to produce slurry-cast supercapacitive electrodes (Table 1).

Other strategies rely on the production of hybrid materials, such as composites and core@shell structures, which will be discussed later, and/or combining the morphology design and hybrid materials engineering with binder-free and self-supporting architectures. The use of binders to produce slurry-cast electrodes for supercapacitor applications significantly reduces the electronic conductivity, limits the active material availability, hinders the ion-diffusion, and increases the mass density as “dead-mass”. Additionally, after repetitive redox reactions, the material can lose the integrity and/or peel-off from the substrate, reducing the capacitance retention through several charge/discharge cycles. Therefore, the above-mentioned downsides can be resolved by the growth of ZnCo₂O₄ electroactive materials directly on the surfaces of electrode substrates, such as nickel foam (NF), carbon foam (CF) and carbon cloth (CC). These strategies not only avoid “dead-mass” but also greatly improve the electroactive surface area, and offer fast electron transportation and short ion diffusion paths. In addition, these strategies will decrease the resistance between the electroactive material and



Table 1 Relevant electrochemical parameters of pristine $Zn_xCo_{3-x}O_4$ -based slurry-cast electrodes and their performance in supercapacitive energy storage devices assembled with a suitable cathode material

Electrode material	Specific capacitance or specific capacity (V)/ref. electrode	Potential window (mV)	Rate capability/ current density range (mV s ⁻¹)	Stability retention/cycle numbers	Highest energy density (W h kg ⁻¹)	Highest power density (W kg ⁻¹)	Negative electrode material in SCs	Ref.
$ZnCo_2O_4$ nanocubes	434 F g ⁻¹ at 5 mV s ⁻¹	-0.5 to 0.5 Ag/AgCl	9.9%/5-50 (mV s ⁻¹)	—	—	—	—	69
Peony-like $ZnCo_2O_4$ nanoparticles	440 F g ⁻¹ at 1 A g ⁻¹	0.0-0.55/SCE	67.7%/1-10	155.6%/3000	29.76 at 398.53 W kg ⁻¹	—	AC	68
Mesoporous $ZnCo_2O_4$ nanosheets	3.3 F cm ⁻² at 1.01 mA cm ⁻²	0.0-0.35/SCE	59.8%/1-10	96.5%/5000	33.98 at 800 W kg ⁻¹	4800 at 16.67 W h kg ⁻¹	AC	70
Hollow $ZnCo_2O_4$ microspheres	78.89 mA h g ⁻¹ at 1 A g ⁻¹	0.0-0.5/SCE	56%/1-10	1.45%/2000	27.78 at 158.5 W kg ⁻¹	920.8 at 12.62 W h kg ⁻¹	AC	62
Porous $Zn_{1.36}Co_{1.64}O_4$ nanoplates	805.3 F g ⁻¹ at 1 A g ⁻¹	0.0-0.5Ag/AgCl	56%/1-25	88%/5100	—	—	Symmetric	56
$ZnCo_2O_4$ nanosheets	290.5 F g ⁻¹ at 0.5 A g ⁻¹	0.0-0.45Ag/AgCl	64.3%/0.5-10	—	0.46 at 22.44 W kg ⁻¹	107.53 at 0.21 W h kg ⁻¹	Symmetric	71
$ZnCo_2O_4$ microparticles	158 F g ⁻¹ at 5 mV s ⁻¹	-0.4 to 0.6/SCE	7.6%/5-200	75%/1000	—	—	—	59
Urchin-like $ZnCo_2O_4$ microspheres	677 F g ⁻¹ at 1 A g ⁻¹	0.0-0.45/SCE	77.5%/1-15	107.3%/5000	—	—	—	64
Porous $ZnCo_2O_4$ microflowers	689 F g ⁻¹ at 1 A g ⁻¹	0.0-0.44/SCE	81.3%/1-15	98.7%/5000	—	—	—	65
Porous $ZnCo_2O_4$ microspheres	126 F g ⁻¹ at 1 A g ⁻¹	0.0-0.6/SCE	77.7%/1-7	—	—	—	—	61
Sphere-like $ZnCo_2O_4$ nanoparticles	843 F g ⁻¹ at 1 A g ⁻¹	0.0-0.45Ag/AgCl	72.7%/1-3	97%/5000	26.28 at 716 W kg ⁻¹	3850 at 3.85 W h kg ⁻¹	AC	67
Porous $ZnCo_2O_4$ nanosheets	3.07 F cm ⁻² at 1.04 mA cm ⁻²	0.0-0.35/SCE	61.2%/1.04-10.4	96.3%/5000	42.83 at 425 W kg ⁻¹	8500 at 12.99 W h kg ⁻¹	AC	72
Sheet-like $ZnCo_2O_4$ microstructures	16.13 mF cm ⁻² at 10 μ A cm ⁻²	0.0-0.4Ag/AgCl	19.9%/10-1000	170%/1000	—	—	—	60
Mesoporous $ZnCo_2O_4$ microflowers	680 F g ⁻¹ at 1 A g ⁻¹	0.0-0.4Ag/AgCl	89.4%/0.35-1	90%/2000	—	—	—	66
Porous $Zn_{1.5}Co_{1.5}O_{4-\delta}$ nanoflowers	763.32 F g ⁻¹ at 1 A g ⁻¹	0.0-0.5Hg/HgO	55.31%/1-30	89.42%/20000	40.49 at 397.37 W kg ⁻¹	50.080 at 20.87 W h kg ⁻¹	AC	74
Rod-like $ZnCo_2O_4$ nanoparticles	135 F g ⁻¹ at 1 A g ⁻¹	0.0-0.45Ag/AgCl	—	—	—	—	—	75
$ZnCo_2O_4$ microspheres	460 F g ⁻¹ at 1 A g ⁻¹	0.0-0.45Ag/AgCl	54.8%/1-5	16.5%/1000	—	—	—	63
Mesoporous $ZnCo_2O_4$ nanosheets	835.26 F g ⁻¹ at 1 A g ⁻¹	0-0.38/SCE	35.6%/1-10	73.28%/1000	—	—	—	73
Porous sphere-like $ZnCo_2O_4$ nanoparticles	420 F g ⁻¹ at 0.5 A g ⁻¹	-0.1 to 0.45Hg/HgO	~71.4%/0.5-10	—	28.6 at 100 W kg ⁻¹	2500 at 18 W h kg ⁻¹	NPC	76
Hollow $ZnCo_2O_4$ nanotubes	362 F g ⁻¹ (181 C g ⁻¹) at 0.5 A g ⁻¹	0.0-0.5/SCE	75.1%/0.5-10	97.4%/10000	10.42 at 375.12 W kg ⁻¹	7503.75 at 6.67 W h kg ⁻¹	AC	77

current collector, provide efficient ion-diffusion channels, ensure excellent mechanical strength, enhance the electrical conductivity and accommodate the volume changes through cycling. Therefore, the challenge to fabricating highly efficient binder-free electrode materials capable of storing rapidly larger amounts of energy, at low cost, can be solved by using ZnCo_2O_4 -modified electrodes. Hence, binder-free electrodes based on pristine ZnCo_2O_4 nanorods,^{78,79} nanobelts,⁸⁰ nanoribbons,⁸¹ nano-flowers,⁸² nanoflakes,^{83,84} nanosheets,⁸⁵⁻⁸⁹ nanomuscles,⁹⁰ nanowires,^{65,91} nanoleaves,⁹² nanocubes,⁹³ micro-urchins,^{94,95} and nanoneedles⁸⁹ were also reviewed for supercapacitor applications (Table 2) and will be discussed along with slurry-cast electrodes according to their morphology.

3.1.1. Pristine ZnCo_2O_4 electrode materials. The micro/nano-structured ZnCo_2O_4 electrode materials discussed in this review article have been prepared *via* different synthetic strategies and, therefore, present distinct electrochemical performances according to their morphologies in both slurry-cast and binder-free electrodes. As expected, in general, less bulky morphologies with higher surface area and lower thickness present higher supercapacitive performance, due to the improved availability of active sites and thus the reduced amount of “dead-mass” of ZnCo_2O_4 . Furthermore, the production of 2D, 1D, hollow and/or porous pristine ZnCo_2O_4 structures is another important factor, increasing the surface area and cycle stability. It allowed enhancing even further the active site availability and specific surface area and mass ratio, resulting in high charge/discharge capacitances even at high current densities.

In the case of Co_3O_4 -based materials, the direct comparison between different MCo_2O_4 materials can only be understood by further analyzing their morphologies instead of just their composition, as reported by Merabet *et al.*⁵⁹ ($\text{M} = \text{Zn, Ni, Mn, and Cu}$) and Alqahtani *et al.*⁶¹ ($\text{M} = \text{Zn, Ni, Mn, Cu, and Fe}$). Both author groups synthesized sphere-like ZnCo_2O_4 microparticles for slurry-cast electrodes, but different morphologies were obtained for other MCo_2O_4 species, impacting their performance. Since their sphere-like ZnCo_2O_4 microparticles presented bulkier morphologies and lower electroactive surface, they exhibited the lowest electrochemical performance, delivering 158 F g^{-1} at 5 mV s^{-1} ⁵⁹ and 126 F g^{-1} at 1 A g^{-1} .⁶¹

Notwithstanding, there are some structural strategies that can be applied to optimize 3D ZnCo_2O_4 morphologies for slurry-cast electrodes, *e.g.*, nanocubes (434 F g^{-1} at 5 mV s^{-1}),⁶⁹ sphere-like NPs (843 F g^{-1} at 1 A g^{-1}),⁶⁷ and rod-like NPs (135 F g^{-1} at 1 A g^{-1}).⁷⁵ However, even though nanocubes⁶⁹ and sphere-like NPs⁶⁷ presented cycling stability (97% after 5000 cycles) and relatively good specific capacitance in comparison to bulk microspheres⁵⁹ and nanorods,⁷⁵ they showed poor rate capability. Nonetheless, the overall stability can be further enhanced by producing hollow (78.89 mA h g^{-1} at 1 A g^{-1}),⁶² and porous microspheres (460 F g^{-1} at 1 A g^{-1}),⁶³ and 420 F g^{-1} at 0.5 A g^{-1}).⁷⁶ Differently from bulk and smooth micro-particles⁵⁹ (Fig. 3A), which presented 75% of their initial specific capacitance after 1000 cycles, the initial specific capacity of hollow ZnCo_2O_4 microspheres⁶² (Fig. 3B) increased to

145% after 2000 cycles, while porous microspheres⁶³ (Fig. 3C) delivered 165% of their initial specific capacitance after 1000 cycles. These results suggest that porous and hollow particles show superior cycling performance due to the facile mass transfer from the interconnected structure of NPs and the void/space in between the particles, alleviating the strain effects of the volume changes during charge/discharge processes. As for binder-free electrodes, there are ZnCo_2O_4 connected nanomuscle network microstructures uniformly grown onto NF (1156.3 F g^{-1} at 1 A g^{-1}),⁹⁰ which originate from agglomerated nanosheets and present a highly porous 3D structure. This can partially buffer the strain effect through the charge-discharge processes, improve the specific surface area and active site availability, and lower the interior resistance, facilitating electron transfer and resulting in such high specific capacitance.

Aside from 3D ZnCo_2O_4 NPs, the literature has reported a series of 2D-structured ZnCo_2O_4 , such as micro-⁶⁰ and nanosheets,^{70-73,85-89} nanoplates,⁵⁶ nanoflakes,^{83,84} nanoleaves,⁹² nanobelts,⁸⁰ nanoribbons,⁸¹ and those based on radial growth of nanosheets, *i.e.*, micro-^{65,66} and nanoflowers.^{74,82} In addition, there are 1D-structured ZnCo_2O_4 , such as urchin-like microspheres,⁶⁴ nanorods^{75,78,79} and nanotubes.⁷⁷ Two-dimensional sheet-like morphologies are known to be generally more suitable than traditional bulk (3D) materials for supercapacitor applications, once they present high specific surface area, higher surface area-to-volume ratios, and shorter ion transportation channels due to their greatly reduced thickness in one dimension, thus improving the availability of electroactive sites for redox reactions, electrical conductivity, cycling stability and ion-diffusion rates.^{56,60,70-73}

All sheet-like ZnCo_2O_4 materials for slurry-cast electrodes encountered in this review had superior capacitance retention through cycling in comparison to bulk spherical and cubic ZnCo_2O_4 nanoparticles due to their more stable morphology. However, they also presented some limitations in rate capability, with a significant decrease in specific capacitance at increasing current density. Presumably, the electrolyte ions have insufficient time to diffuse into the electrode material and to access the active sites at higher scan rates. Even though the highest specific capacitance between slurry-cast electrodes of 835.26 F g^{-1} at 1 A g^{-1} was achieved by mesoporous ZnCo_2O_4 nanosheets produced by Xiao *et al.*⁷³ (Fig. 4A), similar results were achieved with porous $\text{Zn}_{1.36}\text{Co}_{1.64}\text{O}_4$ nanoplates (805.3 F g^{-1} at 1 A g^{-1}),⁵⁶ as well as with mesoporous ZnCo_2O_4 nanosheets (3.3 F cm^{-2} at 1.01 mA cm^{-2}) and porous ZnCo_2O_4 nanosheets (3.07 F cm^{-2} at 1.04 mA cm^{-2}).⁷² In fact, these results are attributed to their porosity and nanosized morphology. Smooth ZnCo_2O_4 nanosheets⁷¹ delivered only 290.5 F g^{-1} at 0.5 A g^{-1} and ZnCo_2O_4 microsheets⁶⁰ delivered the poorest areal capacitance (16.13 mF cm^{-2} at 10 $\mu\text{A cm}^{-2}$) among all materials, along with rather low rate-capability, owing to their inferior specific surface area and the lower availability of electroactive sites, especially at higher current densities.

When assembled in binder-free electrodes, on the other hand, sheet-like ZnCo_2O_4 materials present superb specific capacitance, rate capability and cycling stability and are quite





Table 2 Relevant electrochemical parameters of pristine $Zn_xCo_{3-x}O_4$ -based binder-free electrodes and their performance in supercapacitive energy storage devices assembled with a suitable cathode material

Electrode material	Specific capacitance or specific capacity	Potential window (V)/ref. electrode	Rate capability/ current density range	Stability retention/cycle numbers	Highest energy density (W h kg ⁻¹)	Highest power density (W kg ⁻¹)	Negative electrode material in SCs	Ref.
$ZnCo_2O_4$ nano-rods on CC	5.18 F cm ⁻² at 5 mA cm ⁻²	0–0.6/Ag/AgCl	59.8%/5–100	92.8%/3000	2.3 mW h cm ⁻² at 7.82 mW cm ⁻²	—	PPy/CC	78
$ZnCo_2O_4$ nano-belt-decorated CC	1197.14 F g ⁻¹ at 2 A g ⁻¹	0–0.7/Ag/AgCl	75.2%/2–10	95.01%/5000	79.48 at 894.24 W kg ⁻¹	8900 at 62.1 W h kg ⁻¹	AC/CC	80
Porous $ZnCo_2O_4$ nanoribbons on NF	1957.7 F g ⁻¹ at 3 mA cm ⁻²	0–0.5/SCE	61.7%/3–60	84%/3000	—	—	—	81
$ZnCo_2O_4$ nano-flowers on NF	1657 F g ⁻¹ at 1 A g ⁻¹ ~41 mA h g ⁻¹ at 2 A cm ⁻²	0–0.5/Hg/HgO 0–0.35/SCE	~45%/1–16 ~36%/2–20	89%/2000 94.8%/2000	40 at 1016 W kg ⁻¹	~11 000 at ~22 W h kg ⁻¹	Symmetric	82
Flake-like $ZnCo_2O_4$ nano-structures on CC	1848.9 F g ⁻¹ (832 C g ⁻¹) at 5 A g ⁻¹	0–0.45/Ag/AgCl	88.6%/5–15	85.5%/5000	20.31 at 855 W kg ⁻¹	4250 at 10.2 W h kg ⁻¹	AC/NF	83
Ultra-thin $ZnCo_2O_4$ curved sheets on NF	1156.3 F g ⁻¹ 462.5 C g ⁻¹ at 1 A g ⁻¹	0–0.4/Ag/AgCl	71.5%/1–8	97.4%/5000	—	—	—	85
$ZnCo_2O_4$ nano-muscle networks on NF	2049 F g ⁻¹ at 2 A cm ⁻²	0–0.5/SCE	83.6%/2–30	88.8%/3000	37.5 at 358.2 W kg ⁻¹ 28.8 mW h cm ⁻² at 3 W cm ⁻²	4776.1 at 19.9 W h kg ⁻¹	AC/NF $Fe_2O_3/3D\text{-Ni}$	90
$ZnCo_2O_4$ nano-wires on NF	1170 F g ⁻¹ at 2 A g ⁻¹	0–0.6/Ag/AgCl	51.3%/2–30	95%/3000	50.7 at 187.6 W kg ⁻¹	2950.4 at 37.7 W h kg ⁻¹	AC/NF	96
$ZnCo_2O_4$ nano-flake-decorated porous 3D-Ni	3.19 F cm ⁻² at 2 mA cm ⁻²	0–0.5/Hg/HgO	83.9%/2–30	72.5%/2500	—	—	Fe ₂ O ₃ /3D-Ni	84
Porous $ZnCo_2O_4$ nanosheet networks on NF	1700 F g ⁻¹ at 1 A g ⁻¹	0–0.4/SCE	~36.8%/1–10	110%/8000	63 at 795.5 W kg ⁻¹	—	AC/NF	86
Leaf-like $ZnCo_2O_4$ nano-structures on NF	2040 F g ⁻¹ at 20 A g ⁻¹	0–0.5/SCE	47.7%/50–200 (mV s ⁻¹)	92%/1000	—	—	AC/NF	92
$ZnCo_2O_4$ intertwined heterostructured nanocubes on NF	127.8 F g ⁻¹ at 1 mA cm ⁻²	0–0.5/Ag/AgCl	64%/1–10	80.7%/3000	—	—	—	93
Urchin-like $ZnCo_2O_4$ microspheres on FSSM	1527.2 F g ⁻¹ at 1 A g ⁻¹	0–0.5/Hg/HgO	78.8%/1–10	86%/2000	69.2 at 774.6 W kg ⁻¹	7742.2 at 35.7 W h kg ⁻¹	AC/NF	94
Porous $ZnCo_2O_4$ micro-urchins on NF	1750 F g ⁻¹ at 1.5 A g ⁻¹	0–0.8/Ag/AgCl	72%/1.5–10	96.8%/3000	117.92 at 1490.4 W kg ⁻¹	13 520 at 76.69 W h kg ⁻¹	NPC/CC	91
$ZnCo_2O_4$ intertwined nanoshets on CC	315 F g ⁻¹ at 2 A g ⁻¹	0–0.35/Ag/AgCl	92.4%/2–10	87.09%/6000	25.45 at 3620 W kg ⁻¹	~6050 at ~5 W h kg ⁻¹	$Fe_2O_3/FSSM$	87
$ZnCo_2O_4$ nano-rods on FSSM	400 F g ⁻¹ at 1 A g ⁻¹	0–0.45/SCE	81.8%/1–10	93%/5000	14.1 at 375 W kg ⁻¹	6000 at 4.4 W h kg ⁻¹	N-doped AC/NF	79
$ZnCo_2O_4$ nano-sheets on NF	390 F g ⁻¹ at 1 A g ⁻¹	0.1–0.5/Hg/HgO	69%/1–16	82.5%/10 000	1.27 mW h cm ⁻² at 14.18 W cm ⁻²	62.27 at 0.66 mW h cm ⁻²	AC/NF	88
Porous $ZnCo_2O_4$ micro-urchins on NF	1000 F g ⁻¹ at 20 A g ⁻¹	0–0.5/SCE	52.6%/10–50	93%/5000	—	—	—	95
Porous $Al_{0.5}Zn_{0.5}Co_2O_4$ nanosheets on NF	~1200 F g ⁻¹ at 20 A g ⁻¹	0–0.5/SCE	56.7%/10–50	95%/5000	—	—	—	89

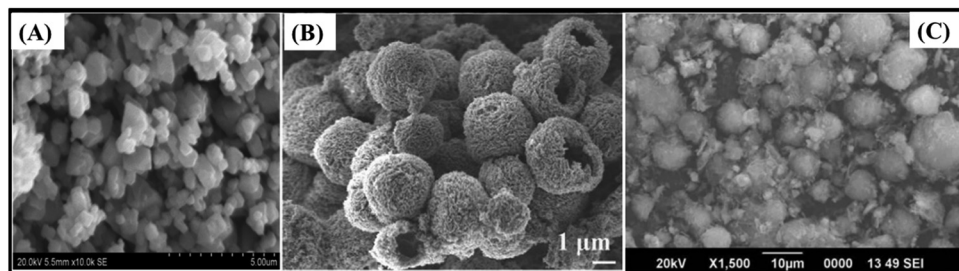


Fig. 3 (A) SEM image of bulk ZnCo_2O_4 microparticles. Reproduced with permission.⁵⁹ Copyright © 2018 Elsevier Ltd and Techna Group S.r.l. All rights reserved. (B) SEM image of hollow ZnCo_2O_4 microspheres. Reproduced with permission.⁶² Copyright © 2018 Elsevier Ltd. All rights reserved. (C) SEM image of porous ZnCo_2O_4 microspheres. Reproduced with permission.⁶³ Copyright © 2018, Springer-Verlag GmbH Germany, part of Springer Nature.

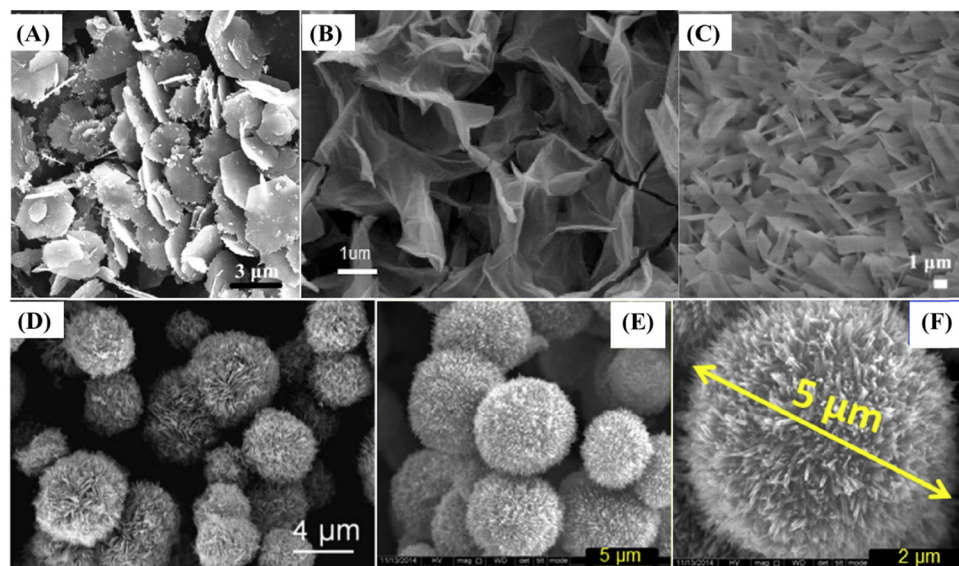


Fig. 4 (A) SEM image of mesoporous ZnCo_2O_4 nanosheets. Reproduced with permission.⁷³ Copyright © 2017, Springer-Verlag GmbH Germany, part of Springer Nature. (B) FESEM image of ultra-thin ZnCo_2O_4 curved nanosheets/NF. Reproduced with permission.⁸⁵ Copyright © 2019 Elsevier Ltd. All rights reserved. (C) SEM image of porous ZnCo_2O_4 nanoribbons/NF. Reproduced with permission.⁸¹ Copyright © 2017 Elsevier Ltd. All rights reserved. (D) SEM image of porous ZnCo_2O_4 microflowers. Reproduced with permission.⁶⁵ Copyright © 2019 Elsevier Ltd and Techna Group S.r.l. All rights reserved. (E and F) SEM images of ZnCo_2O_4 nanoflowers/NF. Reproduced with permission.⁸² Copyright © 2017 Elsevier Ltd. All rights reserved.

competitive.^{80,81,83–89,92} Nanosheets are the most studied 2D morphology of ZnCo_2O_4 ,^{85–88} featuring porous nanosheet networks on NF (3.19 F cm^{-2} at 2 mA cm^{-2}),⁸⁶ intertwined nanosheet arrays on CC (1750 F g^{-1} at 1.5 A g^{-1}),⁸⁷ and NF (400 F g^{-1} at 1 A g^{-1}),⁸⁸ ultra-thin curved nanosheet arrays on NF (1848.9 F g^{-1} at 5 A g^{-1})⁸⁵ (Fig. 4B). These materials presented high rate-capabilities and cycling stabilities, besides porous nanosheet networks on NF,⁸⁶ with a capacitance retention of 72.5% after 2500 cycles. Such good rate capabilities are achieved owing to the nanosheet array arrangements with adequate space between individual nanosheets, composed of many NPs and pores^{85,86,88} or intertwined nanosheets,⁸⁷ which facilitates the transport path for ion-diffusion in charge/discharge processes.

Other binder-free electrodes based on 2D ZnCo_2O_4 materials were also produced in recent years, *i.e.* nanobelts (1197.14 F g^{-1} at 2 A g^{-1}),⁸⁰ nanoribbons (1957.7 F g^{-1} at 3 mA cm^{-2}),⁸¹

flake-like nanostructures ($\sim 41 \text{ mA h g}^{-1}$ at 2 A cm^{-2}),⁸³ nanoflakes (1170 F g^{-1} at 2 A g^{-1}),⁸⁴ nanoleaves (1700 F g^{-1} at 1 A g^{-1}),⁹² and porous $\text{Al}_{0.5}\text{Zn}_{0.5}\text{Co}_2\text{O}_4$ nanosheet arrays on NF ($\sim 1200 \text{ F g}^{-1}$ at 20 A g^{-1}).⁸⁹

ZnCo_2O_4 nanobelts-decorated CC⁸⁰ had a similar structure to interconnected nanosheets and thus provided similar performance to ZnCo_2O_4 nanosheet materials,^{85–88} while flake-like ZnCo_2O_4 nanostructures on CC,⁸³ leaf-like ZnCo_2O_4 nanostructures on NF⁹² and $\text{Al}_{0.5}\text{Zn}_{0.5}\text{Co}_2\text{O}_4$ nanosheet arrays on NF⁸⁹ presented poor rate capabilities despite their high cycling stabilities. The trimetallic oxide-based electrode delivered slightly better performance than pristine ZnCo_2O_4 micro-urchin arrays on NF produced in the same work (approximately 1000 F g^{-1} at 20 A g^{-1}) due to the incorporation of a third metallic center that can enhance even further the ZnCo_2O_4 electrochemical behavior. The leaf-like ZnCo_2O_4 nanostructures on NF⁹² delivered high initial specific capacitance, due



to their high specific surface area and electroactive site availability, but limited morphology for fast ion-diffusion. The poor specific capacity of flake-like ZnCo_2O_4 nanostructures on CC⁸³ seems to be caused by their smooth surface and low specific surface area.

On the other hand, porous ZnCo_2O_4 nanoribbon arrays on NF⁸¹ (Fig. 4C) not only delivered the highest specific capacitance among binder-free 2D ZnCo_2O_4 -modified electrodes, but also demonstrated a good rate capability of 61.7% upon a 20-fold current density increase. In this case, good cycling stability was noticed, maintaining 84% of the initial specific capacitance after 3000 cycles, attributed to the appropriately spaced and highly porous nanoribbon arrays, which provided multiple and facile channels for fast ion-diffusion.

Compared with 2D nanomaterials based on radial growth of nanosheets, *i.e.*, micro-^{65,66} and nanoflowers,⁷⁴ slurry-cast electrodes presented even better rate capability, high specific capacitance and cycling stability. Mesoporous ZnCo_2O_4 micro-flowers⁶⁶ (680 F g^{-1} at 1 A g^{-1}), porous ZnCo_2O_4 micro-flowers⁶⁵ (689 F g^{-1} at 1 A g^{-1}) and porous $\text{Zn}_{1.5}\text{Co}_{1.5}\text{O}_{4-\delta}$ nanoflowers⁷⁴ (763.32 F g^{-1} at 1 A g^{-1}) (Fig. 4D) presented 89.4% (0.35 to 1 A g^{-1}), 81.3% (1 to 15 A g^{-1}) and 55.31% (1 to 30 A g^{-1}) capacitance retention, respectively.

Micro- and nanoflower NPs combine the benefits of strongly interconnected sheet-like structures with a highly porous and hierarchical structure. They also present high specific surface area, promoting reduced mechanical stress. This arises from the huge volumetric expansion during the charge/discharge processes, facilitating electrolyte penetration and ion diffusion into the electroactive material. There is a high availability of electroactive sites even at high current densities and numerous charge/discharge cycles. The binder-free electrode with radial growth of ZnCo_2O_4 nanoflowers on an NF electrode⁸² (Fig. 4E

and F) delivered 1657 F g^{-1} at 1 A g^{-1} , and was designed along with a flake-like ZnCo_2O_4 -modified NF electrode, which delivered 1803 F g^{-1} at 1 A g^{-1} . They presented, respectively, $\sim 45\%$ and $\sim 33.3\%$ rate capability at 16 A g^{-1} , which makes ZnCo_2O_4 nanoflowers on the NF electrode a better candidate for supercapacitive applications even though they still present low specific capacitance retention at higher current densities. Presumably, nanoflower structures are more stable under high current conditions and repeated charge/discharge cycles. The abundance of ion-diffusion channels can improve the electrolyte and electron transport. However, it is still very limited, and the parallelly grown structures can be more suitable for binder-free electrodes in comparison to those radially grown.

There are also some recent works about pristine 1D structured ZnCo_2O_4 . These structures can have some advantages, exhibiting optimal specific surface area and material mass ratios which are only surpassed by typical 0D materials, such as quantum-dots. In this case, it is important to mention their extremely reduced length in two dimensions, shorter ion diffusion lengths and facile electrical transport exclusively in the axial direction. Also relevant are the quantum confinement effects, altering the material properties in such a way that photons can be absorbed at one wavelength and transmitted at another.⁹⁷ These advantages can be further enhanced in slurry-cast electrodes by producing hollow nanotubes (362 F g^{-1} at 0.5 A g^{-1})⁷⁷ (Fig. 5A), with low density, superior specific surface area and shorter ion transport path. Alternatively, urchin-like microspheres (677 F g^{-1} at 1 A g^{-1})⁶⁴ (Fig. 5B) with radially grown porous nanorods have almost the same benefits of porous micro-flowers, both with high rate capability and capacitance retention through cycling for slurry-cast electrodes.

Binder-free electrodes, ZnCo_2O_4 nanorods/CC (5.18 F cm^{-2} at 5 mA cm^{-2}),⁷⁸ nanorods/flexible stainless-steel mesh (FSSM)

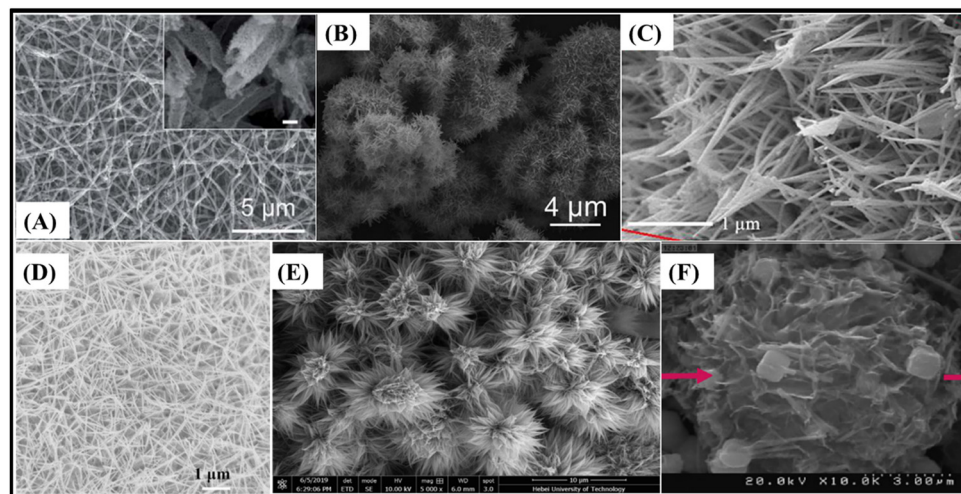


Fig. 5 SEM images of (A) hollow ZnCo_2O_4 nanotubes,⁷⁷ (B) urchin-like ZnCo_2O_4 microspheres,⁶⁴ (C) ZnCo_2O_4 nanorods/CC,⁷⁸ (D) ZnCo_2O_4 nanowire arrays/NF,⁹⁶ (E) porous ZnCo_2O_4 micro-urchins/NF⁹¹ and (F) ZnCo_2O_4 intertwined heterostructured nanocubes/NF.⁹³ Panel A: Reproduced with permission.⁷⁷ Attribution 3.0 Unported (CC BY 3.0), Royal Society of Chemistry. Panel B: Reproduced with permission.⁶⁴ Copyright © 2018 Elsevier Ltd and Techna Group S.r.l. All rights reserved. Panel C: Reproduced with permission.⁷⁸ Copyright © 2018 Elsevier B.V. All rights reserved. Panel D: Reproduced with permission.⁹⁶ Panel E: Reproduced with permission.⁹¹ Copyright © 2019, Springer-Verlag GmbH Germany, part of Springer Nature. Panel F: Reproduced with permission.⁹³ Copyright © 2019 Korean Physical Society. Published by Elsevier B.V. All rights reserved.



(315 F g⁻¹ at 2 A g⁻¹),⁷⁹ nanowires (2049 F g⁻¹ at 2 A cm⁻²),⁶⁵ micro-urchins/FSSM (127.8 F g⁻¹ at 1 mA cm⁻²),⁹⁴ micro-urchins/NF (390 F g⁻¹ at 1 A g⁻¹),⁹⁵ and two porous ZnCo₂O₄ micro-urchins on NF electrodes (1000 F g⁻¹ at 20 A g⁻¹,⁸⁹ 1527.2 F g⁻¹ at 1 A g⁻¹)⁹¹ were also assembled. The ZnCo₂O₄ nano-rod arrays on CC⁷⁸ (Fig. 5C) presented one of the highest rate capabilities based on 1D-morphology, with 59.8% capacitance retention and a 20-fold current density increase, along with a good areal capacitance. The other nanorod-modified electrode, ZnCo₂O₄ nano-rod arrays on FSSM,⁷⁹ delivered not only low specific capacitance but also good rate-capability. This is attributed to the uniform thickness, length, and parallel oriented distribution of ZnCo₂O₄ nanorods with suitable spaces between them, allowing rapid ion-diffusion and active site availability. Nanowire arrays of ZnCo₂O₄ on NF⁹⁶ (Fig. 5D) share almost the same properties of nanorod-modified electrodes, but instead they deliver one of the highest specific capacitances and rate-capabilities among all pristine 1D ZnCo₂O₄-modified binder-free electrodes, with 83.6% capacitance retention after a 15-fold increase in current density. They also exhibit the unusually high cycling stability observed for binder-free electrodes (88.8%, 3000 cycles). This superior performance is inferred to be caused by the higher length of the nanowires in comparison to nanorods. As a result, an interconnective mesoporous structure with very high specific area, abundant available electroactive sites, and shortened distances of electron transportation is obtained. There are also suitable spaces between nanowires for allowing fast and effective ion-diffusion.

Interestingly, two of the reported micro-urchin architectures deliver relatively low specific capacitances for a binder-free ZnCo₂O₄-based electrode,^{94,95} although much higher than those of slurry-cast micro-urchin electrodes produced by a similar synthesis route.⁹⁵ Porous ZnCo₂O₄ micro-urchins on NF electrodes^{89,91} deliver good specific capacitances, due to their larger spatial and porous structure (Fig. 5E), which greatly improves electroactive site availability and promotes better charge transport and ion-diffusion. However, all these mentioned materials presented limited rate-capability as 2D-morphology-based microflowers, due to the lack of parallel orientation. There is no adequate space between the nanostructures for optimizing the electrolyte penetration. Additionally, by combining 1D and 2D features in cubic structures, ZnCo₂O₄ intertwined heterostructured nanocubes on an NF electrode⁹³ (Fig. 5F) were produced. They encompass mixed nanowires and nanosheets directly grown onto NF, with connective channels for electron transfer and suitable pores facilitating rapid ion-diffusion. This results in a high specific capacitance, *e.g.*, 2040 F g⁻¹, at a high current density of 20 A g⁻¹.

3.1.2. ZnCo₂O₄/transition metal-based material composite electrodes. Although pristine ZnCo₂O₄-based electrodes presented relatively good performance due to the increase in supercapacitive performance by morphology design, another strategy to improve their electrochemical performance is by increasing the electroactive site abundance and the specific surface area, combining ZnCo₂O₄ with other TMOs materials, such as MnO₂,⁹⁸ ZnO,⁹⁹⁻¹⁰² MnCo₂O₄,¹⁰³ NiCo₂O₄¹⁰⁴⁻¹⁰⁶ and

Ni₃V₂O₈¹⁰⁷ for slurry-cast electrodes (Table 3) or MnO₂,^{108,109} ZnO,¹¹⁰ NiO,¹¹¹ Co₃S₄,¹¹² ZnCo₂S₄¹¹³ and Zn-Co-S¹¹⁴ for binder-free electrodes (Table 4). These heterojunction-structured materials are composed of a base material that can provide better conductivity for charge and electron transfer and another material that can provide more active sites.¹⁰³ Following a similar strategy, great attention has been directed to core@shell architectures in binder-free electrodes, with ZnCo₂O₄ acting principally as the core material, due to its high electrical conductivity and facile morphological design using MnO₂,^{58,115} CdS,¹¹⁶ Ni₃S₂,¹¹⁷ Ni-Co-S,¹¹⁸ ZnCo₂S₄,¹¹³ Zn-Co-S,¹¹⁴ NiMoO₄,¹¹⁹⁻¹²¹ CoMoO₄,¹²² ZnWO₄,¹²³ NiWO₄,¹²⁴ Ni(OH)₂,^{125,126} and Co-Al LDH¹²⁷ as shell materials, and Co₃O₄ as a core material¹²⁸ (Table 5).

MnO₂ has been considered to be an ideal electrode active material owing to its superior electrochemical activity and high theoretical capacitance (about 1370 F g⁻¹); however, its poor conductivity still precludes practical application in high-performance energy storage devices. Nevertheless, the addition of MnO₂ NPs and nanostructures onto more conductive materials, such as ZnCo₂O₄, can further enhance the electrochemical performance of nanocomposite-based electrodes. As a result, a MnO₂ NP-decorated ultrathin ZnCo₂O₄ nanosheet slurry-cast electrode (286 F g⁻¹ at 1 A g⁻¹)⁹⁸ presents more electroactive sites and specific surface area in comparison to pristine ZnCo₂O₄. Consequently, it provides better transmission channels for electrons due to the superior electrical conduction and suitable morphology of ZnCo₂O₄ support, while the appropriate content of MnO₂ NPs further improves its electrochemical properties, acting as a highly active co-catalyst. Similarly, concerning binder-free electrodes, porous ZnCo₂O₄ nanoflakes of interconnected NPs, with sufficient space to serve as the backbone for the growth of MnO₂ nanosheets, were used to produce a ZnCo₂O₄/MnO₂ heterostructure on NF¹⁰⁸ (Fig. 6A). This drastically increased the availability of electroactive sites and specific surface area, but maintained the space needed for electrolyte diffusion at higher current densities. This new structure was able to deliver 2057 F g⁻¹ at 1 A g⁻¹ with a cycling stability of 96.5% after 5000 cycles and a rate capability of 65% after a 15-fold current density increase.

In fact, heterostructured nanosheet architectures are among the best for ZnCo₂O₄ composite-based binder-free electrodes due to their electrochemical stability, large specific surface area and optimal space between the nanosheets, which maximizes the availability of electroactive sites even at high current density. Therefore, ZnCo₂O₄@MnO₂ hierarchical nanosheet arrays on NF (2170 F g⁻¹ at 3 mA cm⁻²),⁵⁸ based on the growth of MnO₂ nanosheets onto porous ultrathin ZnCo₂O₄ nanosheets, delivered a high specific capacitance similarly to the ZnCo₂O₄/MnO₂ heterostructure on NF.¹⁰⁸ The capacitance retention was 117.5% after 2500 charge/discharge cycles, and the rate capability was 50.4% at 40 mA cm⁻², due to the slow diffusion of electrolyte between the spaces of abundant MnO₂ nanosheets. Moreover, such core@shell materials were also studied in 1D morphology as ZnCo₂O₄@MnO₂ nanowire arrays on NF (4.98 F cm⁻² at 2 mA cm⁻²)¹¹⁵ (Fig. 6B), encompassing





Table 3 Relevant electrochemical parameters of $Zn_xCo_{3-x}O_4$ -based composite materials for slurry-cast electrodes and their performance in supercapacitive energy storage devices assembled with a suitable cathode material

Electrode material	Specific capacitance or specific capacity	Potential window (V) ref. electrode	Rate capability/ current density range	Stability retention/cycle numbers	Highest energy density (W h kg ⁻¹)	Highest power density (W kg ⁻¹)	Negative electrode material in SCs	Ref.
$NiCo_2O_4/ZnCo_2O_4$ heterostructure	1870.9 F g ⁻¹ (1029 C g ⁻¹) at 1 A g ⁻¹	0-0.55/Hg/HgO	58.4%/1-20	91%/10/000	101.6 at 1600 W kg ⁻¹	15 500 at 11 W h kg ⁻¹	NACC	104
$ZnCo_2O_4/CNT$ nanoflowers	1203.8 F g ⁻¹ at 1 A g ⁻¹	0-0.625/Ag/AgCl	56.6%/1-20	87%/3000	24.46 at 750 W kg ⁻¹	—	AC	129
$ZnCo_2O_4/C$ nanofibers	327.5 F g ⁻¹ at 0.5 A g ⁻¹	0-0.4/SCE	27.5%/0.5-8	125%/1000	—	—	—	97
Snowflake-like $ZnCo_2O_4/ZnO$ microstructures	826.7 F g ⁻¹ (372 C g ⁻¹) at 1 A g ⁻¹	0-0.45/SCE	69.6%/1-15	68.7%/5000	—	—	—	99
Hydrangea-like $ZnCo_2O_4/Ni_3V_2O_8$ nanostructures	1734 F g ⁻¹ at 1 A g ⁻¹	0-0.5/SCE	90%/1-10	96%/8000	90 at 812 W kg ⁻¹	7909 at 75 W h kg ⁻¹	AC	107
CNP/ZnO/ZnCo ₃ O ₄ nanosheets	593.6 F g ⁻¹ at 0.25 A g ⁻¹	0-0.4/Ag/AgCl	18.3%/0.25-15	89%/1500	—	—	—	100
$ZnCo_2O_4/rGO$ ultrathin nanosheets	—	—	—	—	31.8 mW h cm ⁻³ at 8.3 mW h cm ⁻³	3880 mW h cm ⁻³ at 8.3 mW h cm ⁻³	Symmetric	130
Nanosheet-like $ZnCo_2O_4/N-GOPANI$ nanosheets	720 F g ⁻¹ at 1.5 A g ⁻¹	0-0.5/SCE	—	~96.4%/10/000	—	—	—	131
N-doped C supported P-ZnCo ₂ O ₄ nanosheets	1581.5 F g ⁻¹ at 1 A g ⁻¹	0-0.5/Hg/HgO	90.6%/1-10	—	47.8 at 800 W kg ⁻¹	—	AC	132
Porous $NiCo_2O_4/ZnCo_2O_4/Co_3O_4$ hollow nanocages	1892.5 F g ⁻¹ at 1 A g ⁻¹	0-0.4/SCE	64.1%/1-10	66%/2000	83.11 at 800 W kg ⁻¹	—	AC	105
Cauliflower-like AuNP/rGO-ZnCo ₂ O ₄	54.1 mA h g ⁻¹ at 25 mA cm ⁻²	0-0.5/SCE	—	97%/2000	—	2121 at 31 W h kg ⁻¹	AC	133
Marigold-like $ZnO/ZnCo_2O_4$ Heterostructured $NiCo_2O_4-$ $ZnCo_2O_4/rGO$ nanosheets	705.1 F g ⁻¹ at 0.3 A g ⁻¹	0-0.5/Ag/AgCl	89.4%/0.3-1	~90%/2500	—	—	—	101
$MWCNT/ZnCo_2O_4$ hexagonal nanoplates	2176.4 F g ⁻¹ (1197 C g ⁻¹) at 1 A g ⁻¹	0-0.55/Hg/HgO	58.2%/1-20	93.8%/5000	62 at 720 W kg ⁻¹	4540 at 7 W h kg ⁻¹	Symmetric	106
Nanosheet-based hollow $ZnO/ZnCo_2O_4/NiO$ microspheres	64 mA h g ⁻¹ at 1 A g ⁻¹	0-0.45/Ag/AgCl	76.6%/1-3	88.1%/2000	71 at 980 W kg ⁻¹	6040 at 17 W h kg ⁻¹	rGO	134
Ultrathin $ZnCo_2O_4/MnO_2$ nanosheets	1136.4 F g ⁻¹ at 1 A g ⁻¹	0-0.5/SCE	~31.2%/1-30	86.5%/5000	—	—	AC	102
Nanosheet-like $g-C_3N_4/ZnCo_2O_4$	286 F g ⁻¹ at 1 A g ⁻¹	0-0.5/Hg/HgO	61.5%/1-10	—	16.94 at 750 W kg ⁻¹	7500 at 11.3 W h kg ⁻¹	AC	98
PANI/ZnCo ₂ O ₄ nanoparticles	1386 F g ⁻¹ (154 mA h g ⁻¹) at 4 A g ⁻¹	0-0.4/Ag/AgCl	~66%/4-8	90%/2500	39 at 1478 W kg ⁻¹	—	Symmetric	135
$ZnCo_2O_4/MnCo_2O_4$ heterojunction nanosheets	867 F g ⁻¹ at 0.5 A g ⁻¹	0-0.4/Ag/AgCl	64%/0.5-4	98.9%/1000	—	7494 at 15.4 W h kg ⁻¹	Symmetric	136



Table 4 Relevant electrochemical parameters of $Zn_xCo_{3-x}O_4$ -based composite materials for binder-free electrodes and their performance in supercapacitive energy storage devices assembled with a suitable cathode material

Electrode material	Specific capacitance or specific capacity (V)/ref. electrode	Potential window (V)/ref. electrode	Rate capability/ current density range	Stability retention/cycle numbers	Highest energy density (W h kg ⁻¹)	Highest power density (W kg ⁻¹)	Negative electrode material in SCs	Ref.
Mesoporous $ZnCo_2O_4$ /NiO flower-like clusters on NF	2797 F g ⁻¹ at 1 A g ⁻¹	0–0.5/SCE	81.8%/1–10	~100%/3000	—	—	—	111
Porous $ZnCo_2O_4$ /MnO ₂ heterostructures on NF	2057 F g ⁻¹ at 1 A g ⁻¹	0–0.4/SCE	65%/1–15	96.5%/5000	69 at 400 W kg ⁻¹	4900 at 21.7 W h kg ⁻¹	AC/NF	108
$ZnCo_2O_4$ /rGO intertwined sheets on NF	3222 F g ⁻¹ at 1 A g ⁻¹	0–0.5/HgO/Hg	26.7%/1–20	65%/5000	49.1 at ~600 W kg ⁻¹	7625 at 18.8 W h kg ⁻¹	AC	137
$ZnCo_2O_4$ /NC hollow nanowall arrays on CT	~2003.8 F g ⁻¹ at ~1.79 A g ⁻¹	0.05–0.45/Ag/AgCl	74.7%/1.79–57.14	~99.4%/10 000	2.32 mW h cm ⁻³ at 33.3 mW cm ⁻³	166.7 mW h cm ⁻³ at 1.70 mW h cm ⁻³	Fe_3O_4 /rGO/CT	138
Sandwich-like $ZnCo_2O_4$ hollow spheres/rGO lamellar films	1075.4 F g ⁻¹ at 1 A g ⁻¹	0–0.4	—	89.3%/10 000	—	—	—	139
3D flower-like $ZnCo_2O_4$ /PVP NC $ZnCo_2O_4$ honey nest nanostructures	761 F g ⁻¹ at 0.35 A g ⁻¹ 1289 F g ⁻¹ at 3.5 A g ⁻¹	0–0.4/Ag/AgCl 0.2–0.45/Ag/AgCl	~89.4%/0.35–1 70%/3.5–20	90%/2000 86%/2000	— 41.9 at 1065.1 W kg ⁻¹	~14 900 at ~29 W h kg ⁻¹	—	66
Heterostructured $ZnCo_2O_4$ /NrGO on NF	1600 F g ⁻¹ at 1 A g ⁻¹	–0.2 to 0.4/SCE	78.1%/1–30	—	66.1 at 701 W kg ⁻¹	7016 at 43.66 W h kg ⁻¹	AC	140
$ZnCo_2O_4$ -decorated $ZnCo_2O_4$ MnO ₂ -doped NF nanosheets on rGO-doped NF	3405.2 F g ⁻¹ at 2 A g ⁻¹	0–0.5/SCE	64.9%/2–20	91.2%/5000	46.85 at 166.67 W kg ⁻¹	1666.67 at 17.13 W h kg ⁻¹	rGO/NF	141
$ZnCo_2O_4$ /Co ₃ S ₄ nanowires on NF	2.02 C g ⁻¹ at 0.8 A g ⁻¹	—	—	95.3%/6000	0.0798 at 1795 W kg ⁻¹	9760 at 0.0732 W h kg ⁻¹	—	112
Porous $ZnCo_2O_4$ nanosheets on rGO-doped NF	680 F g ⁻¹ at 1 A g ⁻¹	0–0.45/Hg/HgO	88%/1–5	95.6%/3000	31.25 at 375 W kg ⁻¹	3750 at 11.46 W h kg ⁻¹	AC	142
$ZnCo_2O_4$ /ZnO heterostructured nanorods on ITO	150 μ F cm ⁻² at 1.2 μ A cm ⁻² (UV-radiation)	0–0.6/symmetric SC	174%/off-on (UV)	—	11.8 10^{-3} μ W h cm ⁻² at 1.2 μ A cm ⁻² (UV)	—	Symmetric	110



Table 5 Relevant electrochemical parameters of $Zn_xCo_{3-x}O_4$ -based core@shell composite materials for binder-free electrodes and their performance in supercapacitive energy storage devices assembled with a suitable cathode material

Electrode material	Specific capacitance or specific capacity	Potential window (V)/ref. electrode	Rate capability/ current density range	Stability retention/cycle numbers	Highest energy density (W kg ⁻¹)	Highest power density (W kg ⁻¹)	Negative electrode material in SCs	Ref.
$ZnCo_2O_4$ @MnO ₂ nanowires on NF	4.98 F cm ⁻² at 2 mA cm ⁻²	0–0.45/SCE	~78.9%/2–16	106.2%/10 000 at 7150 W cm ⁻³	0.058 mW h cm ⁻³	—	AC	115
$ZnCo_2O_4$ @ Ni_3S_2 heterostructured nanowires on NF	2200 F g ⁻¹ at 2 A g ⁻¹	0–0.4/Ag/AgCl	55.7%/2–10	88.9%/1000	—	—	—	117
$ZnCo_2O_4$ @ $NiMoO_4$ heterostructured nanowires on NF	2316 F g ⁻¹ (1158 C g ⁻¹) at 10 mA cm ⁻²	0–0.5/SCE	75.3%/3–40	103.4%/5000	25.3 at 787.9 W kg ⁻¹	9467.5 at 18.4 W h kg ⁻¹	AC	119
$ZnCo_2O_4$ @ $NiMoO_4$ heterostructured nanowires on NF	1912 F g ⁻¹ at 1 A g ⁻¹	0–0.5/Ag/AgCl	55%/1–20	—	57.5 at 900 W kg ⁻¹	18 000 at 30 W h kg ⁻¹	CNT/NF	120
$ZnCo_2O_4$ @ $ZnWO_4$ heterostructured nanowires on NF	13.4 F cm ⁻² at 4 mA cm ⁻²	0–0.4/Ag/AgCl	28.1%/4–64	98.5%/5000	24 at 400 W kg ⁻¹	2001.07 at 16.68 W h kg ⁻¹	AC	123
$ZnCo_2O_4$ @ $ZnWO_4$ heterostructured nanosheets on NF	2192.2 F g ⁻¹ (1096.1 C g ⁻¹) at 10 mA cm ⁻²	0–0.5/SCE	73.8%/3–40	104.1%/5000	29.24 at 884.57 W kg ⁻¹	10526.32 at 20.76 W kg ⁻¹	AC	122
ZnO – $ZnCo_2O_4$ @ $Ni(OH)_2$ heterostructured nanowires on NF	1901.6 F g ⁻¹ (237.7 mA h g ⁻¹) at 2 A g ⁻¹	0–0.45/Ag/AgCl	85.7%/2–20	98.7%/5000	80.10 at 662.06 W kg ⁻¹	9200 at 64.75 W h kg ⁻¹	Fe_2O_3 /NF	125
$ZnCo_2O_4$ @ Ni – Co – S nanosheet-based microspheres on NF	1762.6 F g ⁻¹ at 1 A g ⁻¹	0–0.5/Hg/HgO	81.3%/1–50	81.4%/5000	37.1 at 433.1 W kg ⁻¹	5124.3 at 28.3 W h kg ⁻¹	AC	118
$ZnCo_2O_4$ @ Co – Al LDH nanowires on NF	2041 F g ⁻¹ at 1 A g ⁻¹	0–0.5/SCE	70%/1–10	—	50.1 at 400 W kg ⁻¹	6200 at 16.53 W h kg ⁻¹	AC	127
$rZnCo_2O_4$ @ $NiMoO_4$ – H_2O heterostructured nanowires on NF	3.53 F cm ⁻² at 1 mA cm ⁻²	0–0.5/Ag/AgCl	—	95.4%/5000	2.55 mW h cm ⁻³ at 0.033 W cm ⁻³	0.169 W cm ⁻³ at 0.39 mW h cm ⁻³	CNT	121
Porous $ZnCo_2O_4$ /C nanowires on NF	2340 F g ⁻¹ (7.02 F cm ⁻²) at 1 mA cm ⁻²	0–0.5/Hg/HgO	~57%/1–20	92.6%/10 000	35.75 at 73.17 W kg ⁻¹	~1900 at ~4.5 W h kg ⁻¹	AC	143
Porous $ZnCo_2O_4$ @ $Ni(OH)_2$ nanosheets on NF	1021.1 F g ⁻¹ (3.06 F cm ⁻²) at 1 mA cm ⁻²	0–0.5/SCE	55.3%/1–10	50.1%/5000	40.0 at 802.7 W kg ⁻¹	8020 at 17.6 W h kg ⁻¹	AC	126
$ZnCo_2O_4$ @PPy nanostructures on NF	1210 F g ⁻¹ (605 C g ⁻¹) at 1 A g ⁻¹	0–0.5/Ag/AgCl	56%/1–10	93.5%/9000	141.3 at 2700.5 W kg ⁻¹	~27 000 at ~90 W h kg ⁻¹	AC	57
$ZnCo_2O_4$ @ $NiWO_4$ heterostructures on NF	1782 F g ⁻¹ (2.14 F cm ⁻²) at 1 mA cm ⁻²	0–0.5/Hg/HgO	35.5%/1–10	95.4%/5000	42.2 at 716 W kg ⁻¹	3087 at 34.3 W h kg ⁻¹	AC	124
$ZnCo_2O_4$ @ MnO_2 hierarchical nanosheets on NF	2170 F g ⁻¹ (2.6 F cm ⁻²) at 3 mA cm ⁻²	0–0.5/SCE	50.4%/3–40	11.7.5% 2500	29.41 at 628.42 W kg ⁻¹	8378.38 at 6.98 W h kg ⁻¹	AC	58
Leaf-like $ZnCo_2O_4$ @PPy on NF	2507.0 F g ⁻¹ (3.75 F cm ⁻²) at 0.5 A g ⁻¹	0–0.5/Hg/HgO	~69%/0.5–20	83.22%/5000	44.15 at 850 W kg ⁻¹	4250 at 33.06 W h kg ⁻¹	AC	144
$ZnCo_2O_4$ @CdS nanoflowers on NF	5.91 F cm ⁻² (2.66 C cm ⁻²) at 25 mA	0–0.45/SCE	62.2%/25–40	—	—	—	—	116
Mesoporous Co_3O_4 @ $ZnCo_2O_4$ nanowires on NF	2255.5 F g ⁻¹ (1240.5 C g ⁻¹) at 2 mA cm ⁻²	0–0.55/Hg/HgO	59.0%/2–30	90.9%/3000	37.3 at 800 W kg ⁻¹	8000 at 21.3 W h kg ⁻¹	AC	128
Flower-like $ZnCo_2O_4$ @ $ZnCo_2S_4$ nanostructures on NF	1057.78 F g ⁻¹ at 1 A g ⁻¹	SCE	54.6%/1–10	—	127.4 at 2520 W kg ⁻¹	36497.16 at 40.55 W h kg ⁻¹	CNTs	113
$ZnCo_2O_4$ @ Zn – Co – S hybrid nanowires on CNTFs	~1.35 F cm ⁻² at 0.5 mA cm ⁻²	–0.1 to 0.6/SCE	—	—	32.01 μ W h cm ⁻² at 698.42 μ W h cm ⁻²	6999.99 μ W cm ⁻² at 12.38 μ W h cm ⁻²	H – Co_3O_4 / CoNC/ CNTFs	113

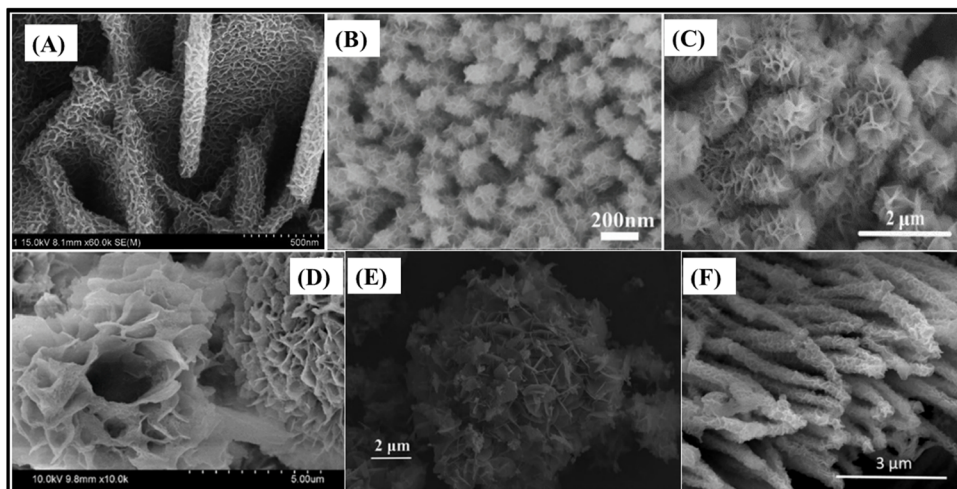


Fig. 6 SEM images of (A) porous $\text{ZnCo}_2\text{O}_4/\text{MnO}_2$ heterostructures/NF,¹⁰⁸ (B) $\text{ZnCo}_2\text{O}_4@\text{MnO}_2$ nanowires/NF,¹¹⁵ (C) mesoporous $\text{ZnCo}_2\text{O}_4/\text{NiO}$ flower-like clusters/NF,¹¹¹ (D) $\text{ZnCo}_2\text{O}_4@\text{CdS}$ nanoflowers/NF,¹¹⁶ (E) hydrangea-like $\text{ZnCo}_2\text{O}_4/\text{Ni}_3\text{V}_2\text{O}_8$ nanostructures/NF¹⁰⁷ and (F) $\text{ZnCo}_2\text{O}_4@\text{Ni}_3\text{S}_2$ heterostructured nanowires/NF.¹¹⁷ Panel A: Reproduced with permission.¹⁰⁸ Copyright © 2018 Elsevier Ltd. All rights reserved. Panel B: Reproduced with permission.¹¹⁵ Copyright Marketplace™, Royal Society of Chemistry. Panel C: Reproduced with permission.¹¹¹ Copyright © 2018 Elsevier Ltd. All rights reserved. Panel D: Reproduced with permission.¹¹⁶ Copyright © 2020 Korean Physical Society. Published by Elsevier B.V. All rights reserved. Panel E: Reproduced with permission.¹⁰⁷ Copyright © 2019 Elsevier Ltd and Techna Group S.r.l. All rights reserved. Panel F: Reproduced with permission.¹¹⁷ Copyright © 2017 Elsevier B.V. All rights reserved.

smooth ZnCo_2O_4 nanowires uniformly covered with a porous MnO_2 thin film. This largely increased the specific surface area of the electrode, delivering 5 times more specific capacitance than that of pristine ZnCo_2O_4 nanowires, in addition to exhibiting much better cycling stability (106.2% vs. 87.7% after 10 000 cycles) and rate capability (~78.9% vs. 57.4% at 16 mA cm^{-2}).

Binder-free electrodes were studied in recent years, using the same strategy of designing decorated nanocomposites, $\text{ZnCo}_2\text{O}_4/\text{Co}_3\text{S}_4$ nanowire arrays on NF (2.02 C g^{-1} at 0.8 A g^{-1})¹¹² and mesoporous $\text{ZnCo}_2\text{O}_4/\text{NiO}$ flower-like clusters on NF (2797 F g^{-1} at 1 A g^{-1}),¹¹¹ as well as slurry-cast electrodes and $\text{ZnCo}_2\text{O}_4@\text{CdS}$ nanoflowers on NF (5.91 F cm^{-2} at 25 mA).¹¹⁶ Mesoporous $\text{ZnCo}_2\text{O}_4/\text{NiO}$ flower-like clusters on NF¹¹¹ (Fig. 6C) make use of highly electroactive NiO nanosheets, with a theoretical specific capacitance of 3750 F g^{-1} , assembled onto ZnCo_2O_4 microspheres. In this case, the NiO nanosheets form flower-like clusters, and relieve the internal stress and restrain the capacitance decay through the charge-discharge processes. In addition, they help in reducing the ion-diffusion path length and increasing the specific surface area. As a result, very high specific capacitance and overall stability are achieved, with a retention of 81.8% upon a 10-fold current density increase and ~100% after 3000 cycles. CdS is another highly electroactive semiconductor candidate for supercapacitive applications due to its excellent conductivity and high theoretical capacity of 1675 F g^{-1} . Therefore, it is assembled with CdS nanoparticles as the coating shell and ZnCo_2O_4 nanoflowers as the core (Fig. 6D),¹¹⁶ delivering more than 10 times the specific capacitance of pristine ZnCo_2O_4 nanoflowers. There is a low rate capability, mainly due to the intrinsically low electrolyte diffusion at higher current densities for the flower-like structured binder-free electrode, and

also some limitation of ion-diffusion through the CdS nanoparticle shell.

In addition, $\text{Ni}_3\text{V}_2\text{O}_8$ and Ni_3S_2 have also been used for supercapacitive applications owing to their high performance and capacity. In fact, slurry-cast hydrangea-like $\text{ZnCo}_2\text{O}_4/\text{Ni}_3\text{V}_2\text{O}_8$ nanostructures composed of ZnCo_2O_4 nanospheres and $\text{Ni}_3\text{V}_2\text{O}_8$ nanosheets¹⁰⁷ (Fig. 6E) present nanoflower-like heterostructures that can provide open space for ion-diffusion pathways, exposing various redox active sites for electrochemical reactions and electron transport, delivering 1734 F g^{-1} at 1 A g^{-1} . It also presents superior cycling stability and rate capability, retaining 96% of its initial specific capacitance after 8000 cycles and 90% from 1 to 10 A g^{-1} . The binder-free core@shell $\text{ZnCo}_2\text{O}_4@\text{Ni}_3\text{S}_2//\text{NF}$ electrode (2200 F g^{-1} at 2 A g^{-1})¹¹⁷ (Fig. 6F) exhibits interconnected Ni_3S_2 nanosheets coated on the surfaces of the highly ordered and dense ZnCo_2O_4 nanowire arrays. It delivered high specific capacitance because of the two-dimensional (2D) nanosheet coating, which largely increases the specific surface area. However, 55.7% rate capability at 5-fold current density is due to the reduced space between nanowires that limits the electrolyte diffusion at higher current densities.

Zinc oxide (ZnO), an n-type semiconductor with a wide band gap (~3.37 eV), can synergize well with ZnCo_2O_4 , a p-type semiconductor, to produce $\text{ZnCo}_2\text{O}_4/\text{ZnO}$ heterostructures with p-n junctions. The n-type region has a high electron concentration and the p-type, a high hole concentration; so electrons diffuse from the n-type side to the p-type side. Therefore, the electrons generated at ZnO sites in charge/discharge cycles can rapidly diffuse into the ZnCo_2O_4 matrix, potentially enhancing the overall electronic conduction of the composite. All $\text{ZnCo}_2\text{O}_4/\text{ZnO}$ composites used in slurry-cast electrodes found in the

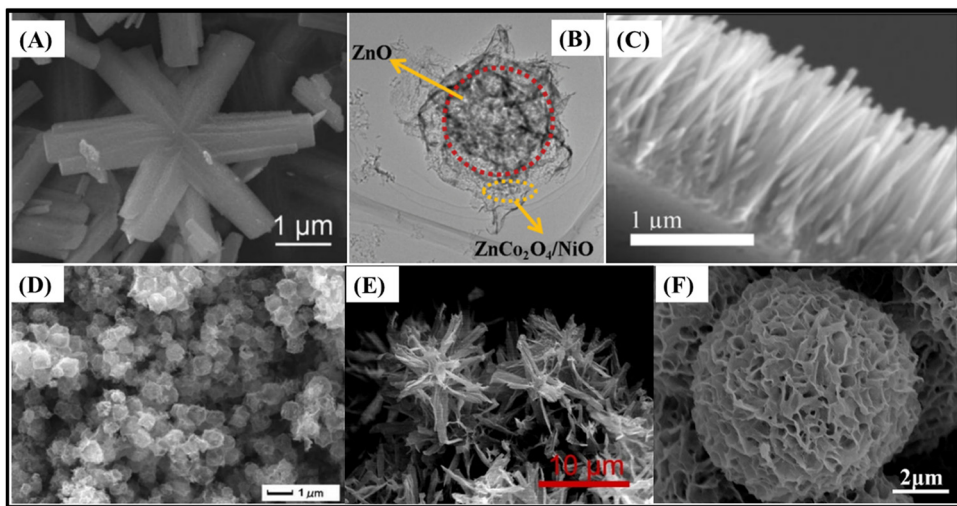


Fig. 7 (A) SEM image of snowflake-like $\text{ZnCo}_2\text{O}_4/\text{ZnO}$ microstructures.⁹⁹ (B) TEM image of nanosheet-based hollow $\text{ZnO}/\text{ZnCo}_2\text{O}_4/\text{NiO}$ microspheres,¹⁰² and SEM images of (C) $\text{ZnCo}_2\text{O}_4/\text{ZnO}$ heterostructured nanorods/ITO,¹¹⁰ (D) porous $\text{NiCo}_2\text{O}_4/\text{ZnCo}_2\text{O}_4/\text{Co}_3\text{O}_4$ hollow nanocages,¹⁰⁵ (E) flower-like $\text{ZnCo}_2\text{O}_4@\text{ZnCo}_2\text{S}_4$ nanostructures/NF,¹¹³ and (F) $\text{ZnCo}_2\text{O}_4@\text{Ni-Co-S}$ nanosheet-based microspheres/NF.¹¹⁸ Panel A: Reproduced with permission.⁹⁹ © 2019 Elsevier Ltd and Techna Group S.r.l. All rights reserved. Panel B: Reproduced with permission.¹⁰² Copyright Marketplace™, Royal Society of Chemistry. Panel C: Reproduced with permission.¹¹⁰ Copyright © 2018 American Chemical Society. Panel D: Reproduced with permission.¹⁰⁵ Copyright © 2018 Elsevier B.V. All rights reserved. Panel E: Reproduced with permission.¹¹³ Copyright © 2020, Springer Science Business Media, LLC, part of Springer Nature. Panel F: Reproduced with permission.¹¹⁸ Copyright © 2020 Elsevier B.V. All rights reserved.

literature presented very high specific surface area, due to radially grown structures such as snowflake-like $\text{ZnCo}_2\text{O}_4/\text{ZnO}$ (826.7 F g^{-1} at 1 A g^{-1})⁹⁹ and marigold-like $\text{ZnO}/\text{ZnCo}_2\text{O}_4$ (705.1 F g^{-1} at 0.3 A g^{-1}),¹⁰¹ or hollow structures, such as nanosheet-based hollow $\text{ZnO}/\text{ZnCo}_2\text{O}_4/\text{NiO}$ microspheres (1136.4 F g^{-1} at 1 A g^{-1}).¹⁰² Snowflake-like $\text{ZnCo}_2\text{O}_4/\text{ZnO}$ microstructures⁹⁹ (Fig. 7A) presented superior performance not only in specific capacitance but also in rate capability. They delivered 69.6% of their initial capacitance after a 15-fold increase in current density, due to the more suitable open space for the ion-diffusion pathway in comparison to tight nanosheets in marigold-like $\text{ZnO}/\text{ZnCo}_2\text{O}_4$ (89.4%, $0.3\text{--}1 \text{ A g}^{-1}$).¹⁰¹

Hollow $\text{ZnO}/\text{ZnCo}_2\text{O}_4/\text{NiO}$ microspheres¹⁰² are covered with numerous ultrathin nanosheets and decorated with tiny pores (Fig. 7B), which provide optimized specific surface area and access to plenty of electrolyte. Such characteristics are beneficial for the exposure of electroactive sites, buffering the effect of volume changes and promoting suitable channels to facilitate rapid ion/electron diffusion during the charge/discharge processes. The result encompasses 86.5% capacitance retention after 5000 cycles and, due to the tiny pore sizes and spaces within the ultrathin nanosheets, rate capabilities of $\sim 31.2\%$ and 54.9% with 30- and 10-fold current density increases, respectively. As for binder-free electrodes, there are $\text{ZnCo}_2\text{O}_4/\text{ZnO}$ heterostructured nanorods on an ITO electrode ($150 \mu\text{F cm}^{-2}$ at $1.2 \mu\text{A cm}^{-2}$ with UV-radiation)¹¹⁰ (Fig. 7C), which feature both the photoelectric effect and direct electron transportation pathway. Photoinduced electrons and holes, under UV radiation, participate directly in the electrolyte ion separation process to boost the overall capacitive response, thus delivering 174% (2.7 times) more

specific capacitance under UV illumination as compared to the absence of UV.

Differently from the mentioned core@shell materials, the mesoporous $\text{Co}_3\text{O}_4@\text{ZnCo}_2\text{O}_4/\text{NF}$ electrode (2255.5 F g^{-1} at 2 mA cm^{-2})¹²⁸ features ZnCo_2O_4 as the shell material, due to its excellent rate capability and cycling stability. In this way it could improve the practical application of the electrode; even so, it has better electrical conductivity than its core. The directly grown needle-like Co_3O_4 nanowire arrays are composed of numerous polycrystalline interconnected nanoparticles, which provides good roughness, increasing the specific surface area and facilitating the uniform coating with the ZnCo_2O_4 thin film composed of multiple nanoparticles. As a result, the electrode delivers high specific capacitance, about 3-times more than that of $\text{Co}_3\text{O}_4/\text{NF}$, with a capacitance retention of 59.0% and 90.9% after a 15-fold current density increase and 3000 cycles, respectively.

Composites based on heterojunctions of ZnCo_2O_4 and other MCo_2O_4 usually present: (i) richer and more abundant redox reaction sites and, thus, higher specific capacitances; (ii) more stability, since both have high contents of $\text{Co}_2\text{O}_4^{2-}$; and (iii) similar lattice parameters, in which the internal resistance of the adjacent interfaces is greatly reduced during the charge/discharge processes and facilitates the electron transport. In this context, $\text{ZnCo}_2\text{O}_4/\text{MnCo}_2\text{O}_4$ heterojunction nanosheets (254 F g^{-1} at 1 A g^{-1})¹⁰³ and $\text{NiCo}_2\text{O}_4/\text{ZnCo}_2\text{O}_4$ heterostructures (1870.9 F g^{-1} at 1 A g^{-1})¹⁰⁴ composed of ZnCo_2O_4 nanosheets and urchin-like NiCo_2O_4 , and porous $\text{NiCo}_2\text{O}_4/\text{ZnCo}_2\text{O}_4/\text{Co}_3\text{O}_4$ hollow nanocages (1892.5 F g^{-1} at 1 A g^{-1})¹⁰⁵ (Fig. 7D) formed by interconnecting ultra-small nanoparticles with many voids that results in porous multiple shells have been reported.

Despite delivering relatively low specific capacitance, slurry-cast $\text{ZnCo}_2\text{O}_4/\text{MnCo}_2\text{O}_4$ heterojunction nanosheet electrodes¹⁰³ presented higher specific capacitance and overall stability than pristine ZnCo_2O_4 and MnCo_2O_4 . In fact, the other two composites also presented much better performance than their counterparts in slurry-cast electrodes $\text{NiCo}_2\text{O}_4/\text{Co}_3\text{O}_4$ and $\text{ZnCo}_2\text{O}_4/\text{Co}_3\text{O}_4$, with $\text{NiCo}_2\text{O}_4/\text{ZnCo}_2\text{O}_4/\text{Co}_3\text{O}_4$ hollow nanocages,¹⁰⁵ and urchin-like NiCo_2O_4 and sheet-like ZnCo_2O_4 for $\text{NiCo}_2\text{O}_4/\text{ZnCo}_2\text{O}_4$ heterostructures. Notwithstanding, these $\text{NiCo}_2\text{O}_4/\text{ZnCo}_2\text{O}_4$ -based composites exhibit the second and third highest specific capacitances among all reported slurry-cast electrodes. They also show superior electrical conductivity, rich and abundant electrochemically active sites, high specific surface area, and good rate capability and cycling stability,^{104,105} with a capacitance retention of 58.4% and 91% after a 20-fold current density increase and 10 000 cycles, respectively.

Transition metal sulfides display higher electrical conductivity than their oxide counterparts because the replacement of oxygen with sulfur allows easier electron transport, lower electronegativity and smaller band-gaps, making them good candidates for supercapacitive applications and thus improving the energy storage properties of ZnCo_2O_4 in composite architectures. From this perspective, there are binder-free electrodes based on core@shell $\text{ZnCo}_2\text{O}_4@\text{Zn}_x\text{Co}_{3-x}\text{S}_4$ materials, such as those based on flower-like $\text{ZnCo}_2\text{O}_4@\text{ZnCo}_2\text{S}_4$ arrays//NF (1057.78 F g⁻¹ at 1 A g⁻¹)¹¹³ and $\text{ZnCo}_2\text{O}_4@\text{Zn-Co-S}$ hybrid arrays//CNTFs (~1.35 F cm⁻² at 0.5 mA cm⁻²)¹¹⁴ and microsphere-structured $\text{ZnCo}_2\text{O}_4@\text{Ni-Co-S}$ nanosheets (1762.6 F g⁻¹ at 1 A g⁻¹).¹¹⁸ The flower-like $\text{ZnCo}_2\text{O}_4@\text{ZnCo}_2\text{S}_4/\text{NF}$ ¹¹³ electrode (Fig. 7E) delivered good specific capacitance and, even so the hierarchical micro-nanostructured features could further improve the electrochemical properties of the electrode by offering larger spacing for the penetration of electrolyte into the structure. Thus, it could increase the availability of electroactive sites at higher current densities and electron transfer. A capacitance retention of 54.6% was achieved by a 10-fold increase in current density, as expected for a flower-like structure-based binder-free electrode.

Among bimetallic sulfides, nickel-cobalt sulfides have attracted a lot of attention due to their excellent conductivity, superior to nickel and cobalt sulfide counterparts and about 100 times higher than those of the corresponding oxides, and better capacitance performance compared with other metallic sulfides, such as NiS, Ni_3S_2 , and CoS. In this context, slurry-cast core@shell $\text{ZnCo}_2\text{O}_4@\text{Ni-Co-S}$ microspheres composed of radially grown ZnCo_2O_4 nanosheets, with a rough surface of electrodeposited Ni-Co-S¹¹⁸ (Fig. 7F), delivered higher specific capacitance, rate capability and cycling stability than their pristine ZnCo_2O_4 and Ni-Co-S counterparts. The increase of capacitance occurs mainly due to their hierarchical micro-nanostructure that has an open network of individual nanosheets. They facilitate ion-diffusion and help in maintaining the structural integrity. The highly conductive Ni-Co-S shell can efficiently decrease the charge transfer resistance, leading to a fast reversible redox reaction, ample redox active site availability and short ion diffusion pathways, thus resulting

in a capacitance retention of 81.3% at a 50-fold increase in current density and 81.4% after 5000 cycles.

Notwithstanding, other materials have also attracted great attention as promising electrodes for energy storage devices, such as molybdenum- and tungsten-based metal oxides, nickel hydroxides and layered double hydroxides (LDHs). Core@shell structures along with ZnCo_2O_4 have been studied as shell materials, to achieve competitive supercapacitive performance. Molybdenum-based metal oxides such as NiMoO_4 ¹¹⁹⁻¹²¹ and CoMoO_4 ¹²² in core@shell architectures with ZnCo_2O_4 were studied, due to their high theoretical specific capacity attributed to Ni and Co ions, and excellent electrical conductivity, attributed to the multiple redox reactions of Mo ions.¹¹⁹⁻¹²² All three reviewed core@shell $\text{ZnCo}_2\text{O}_4@\text{NiMoO}_4$ materials had hierarchical nanowire and nanosheet architectures grown on NF, although with some differences that were relevant to their electrochemical performance, respectively: intercrossed ZnCo_2O_4 nanowires covered with NiMoO_4 nanosheets (2316 F g⁻¹ at 10 mA cm⁻²)¹¹⁹ (Fig. 8A); ZnCo_2O_4 nanowires covered with an ultrathin porous NiMoO_4 nanosheet network (1912 F g⁻¹ at 1 A g⁻¹)¹²⁰ (Fig. 8B); and smooth reduced- ZnCo_2O_4 nanowires covered with NiMoO_4 nanosheets (3.53 F cm⁻² at 1 mA cm⁻²)¹²¹ (Fig. 8C). Comparing all three electrodes, the first one¹¹⁹ not only had the best cycling stability and specific capacitance, but also presented hierarchical heterostructures for the nanowires with the smallest diameter, which facilitated ion-diffusion. The rate-capability was the best one, although it was still relatively low as a nanowire-based binder-free electrode. On the other hand, the core@shell $\text{ZnCo}_2\text{O}_4@\text{CoMoO}_4/\text{NF}$ electrode (2192.2 F g⁻¹ at 10 mA cm⁻²) presented smooth honeycomb-like ZnCo_2O_4 nanosheets covered with interconnected rough CoMoO_4 nanosheets. In this way, it could effectively shorten the ion transport distance and increase the availability of electroactive sites, thus delivering high specific capacitance and excellent cycling stability, along with good rate-capability.

Tungsten-based metal oxides with wolframite structure, such as ZnWO_4 ¹²³ and NiWO_4 ,¹²⁴ are promising materials for sensor, photocatalyst and energy storage systems. They allow supercapacitive applications, with high theoretical specific capacitance, where both Zn/Ni and W elements participate in the faradaic redox reactions and have high electrical conductivity. Core@shell $\text{ZnCo}_2\text{O}_4@\text{ZnWO}_4$ (13.4 F cm⁻² at 4 mA cm⁻²)¹²³ (Fig. 8D) and $\text{ZnCo}_2\text{O}_4@\text{NiWO}_4$ (1782 F g⁻¹ and 2.14 F cm⁻² at 1 mA cm⁻²)¹²⁴ (Fig. 8E) present heterostructured ultrathin and interconnected nanosheet-covered nanowires on NF architecture. They can deliver high specific and areal capacitance, especially in the case of $\text{ZnCo}_2\text{O}_4@\text{ZnWO}_4$ where the highly conductive ZnCo_2O_4 nanowire arrays rationally overcome the poor conductivity of ZnWO_4 nanosheets which could shorten the ion-diffusion and electron transport pathways. Additionally, both electrodes present relatively poor rate-capability as nanowire-based binder-free electrodes, with a capacitance retention of 28.1% at 64 mA cm⁻²¹²³ and 35.5%¹²⁴ at 10 mA cm⁻², respectively.

Considering hydroxide-based shell materials, recent reports can be found in the literature for $\text{Ni}(\text{OH})_2$ ^{125,126} and Co-Al



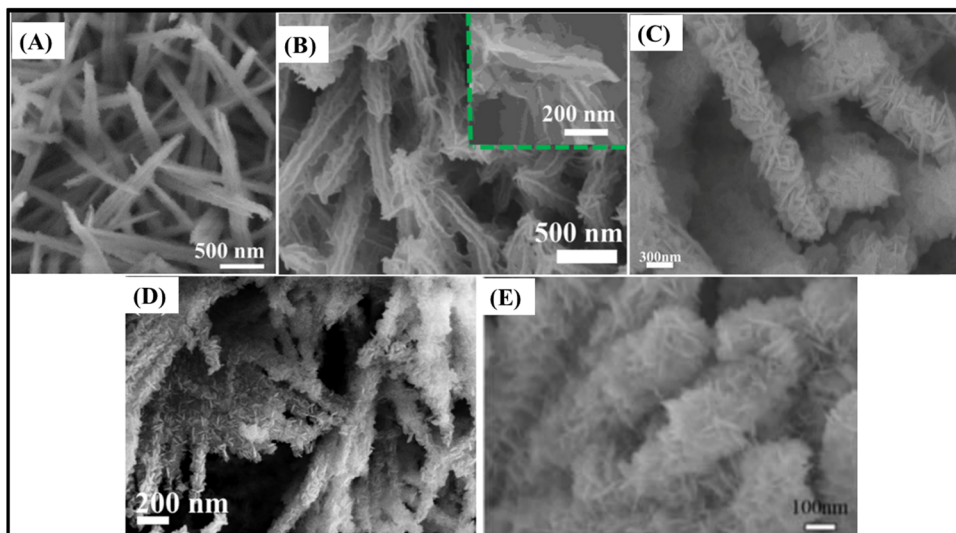


Fig. 8 SEM images of (A) $\text{ZnCo}_2\text{O}_4@\text{NiMoO}_4$ heterostructured nanowires/NF,¹¹⁹ (B) $\text{ZnCo}_2\text{O}_4@\text{NiMoO}_4$ heterostructured nanowires/NF,¹²⁰ (C) $\text{r-ZnCo}_2\text{O}_4@\text{NiMoO}_4\cdot\text{H}_2\text{O}$ heterostructured nanowires/NF,¹²¹ (D) $\text{ZnCo}_2\text{O}_4@\text{ZnWO}_4$ heterostructured nanowires/NF¹²³ and (E) $\text{ZnCo}_2\text{O}_4@\text{NiWO}_4$ heterostructures/NF.¹²⁴ Panel A: Reproduced with permission.¹¹⁹ Copyright © 2020 Elsevier Ltd. All rights reserved. Panel B: Reproduced with permission.¹²⁰ Copyright © 2020 Elsevier Ltd. All rights reserved. Panel C: Reproduced with permission.¹²¹ © 2018 Elsevier B.V. All rights reserved. Panel D: Reproduced with permission.¹²³ Copyright © 2018 Published by Elsevier Inc. Panel E: Reproduced with permission.¹²⁴ Copyright © 2020, Springer-Verlag GmbH Germany, part of Springer Nature.

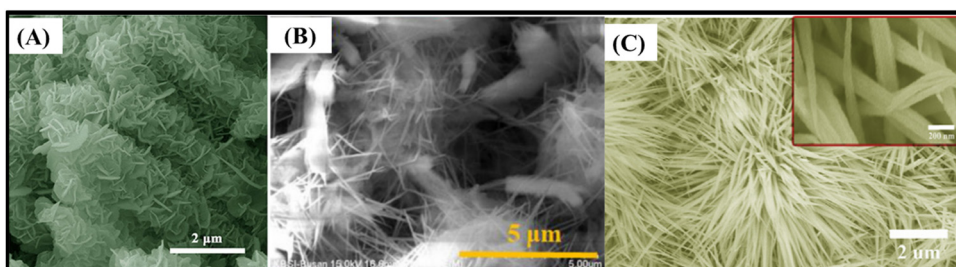


Fig. 9 SEM images of (A) porous $\text{ZnCo}_2\text{O}_4@\text{Ni}(\text{OH})_2$ nanosheets/NF,¹²⁶ (B) $\text{ZnO-ZnCo}_2\text{O}_4@\text{Ni}(\text{OH})_2$ heterostructured nanowires/NF,¹²⁵ and (C) $\text{ZnCo}_2\text{O}_4@\text{Co-Al LDH}$ nanowires on NF.¹²⁷ Panel A: Reproduced with permission.¹²⁶ Copyright © 2018 Wiley-VCH Verlag GmbH & Co. KGaA, Weinheim. Panel B: Reproduced with permission.¹²⁵ Copyright © 2020 Elsevier Ltd. All rights reserved. Panel C: Reproduced with permission.¹²⁷ Copyright © 2019 Elsevier Ltd and Techna Group S.r.l. All rights reserved.

LDH.¹²⁷ The $\text{ZnCo}_2\text{O}_4@\text{Ni}(\text{OH})_2/\text{NF}$ electrode (1021.1 F g^{-1} and 3.06 F cm^{-2} at 1 mA cm^{-2})¹²⁶ (Fig. 9A) based on crosslinked ultrathin nanoflakes, covering porous nanosheets with a thick triangular shape, delivered good specific capacitance but low rate-capability and cycling stability. They have been ascribed to the bulkiness of the ZnCo_2O_4 nanosheets and reduced space between them, which hinders the ion-diffusion and electron transfer. This also reduces the control of the strain effects due to volume changes through cycling. Conversely, $\text{ZnO-ZnCo}_2\text{O}_4@\text{Ni}(\text{OH})_2/\text{NF}$ (1901.6 F g^{-1} at 2 A g^{-1})¹²⁵ (Fig. 9B) delivered not only higher specific capacitance, but also high rate-capability for a heterostructured nanowire-based binder-free electrode, with 85.7% capacitance retention at 20 A g^{-1} , along with high cycling stability, retaining 98.7% of its initial capacitance after 5000 cycles. Additionally, the $\text{ZnO-ZnCo}_2\text{O}_4@\text{ZnO/NF}$, $\text{ZnO-ZnCo}_2\text{O}_4@\text{CoO/NF}$ and $\text{ZnO-ZnCo}_2\text{O}_4/\text{NF}$ electrodes have been studied for comparison purposes, delivering

approximately 54%, 40% and 31%, respectively, of the specific capacitance of $\text{ZnO-ZnCo}_2\text{O}_4@\text{Ni}(\text{OH})_2/\text{NF}$. The superior performance of $\text{ZnO-ZnCo}_2\text{O}_4@\text{Ni}(\text{OH})_2/\text{NF}$ is attributed to the nanoflake-covered interconnected nanowires forming a hierarchical porous 2D network on top of the NF. This provides a high surface area, with plenty of space for electrolyte diffusion, which in conjunction with the available electroactive sites facilitates the electron transport through the $\text{ZnO-ZnCo}_2\text{O}_4$ nanowires.

Layered double hydroxides (LDHs) have high theoretical capacity, low cost and environmental compatibility. However, their inherent low conductivity and aggregation effects hinder charge transportation, leading to low electrochemical performance. However, when an LDH is assembled as a shell material combined with a highly conductive core, such as ZnCo_2O_4 , superior performance is expected. In fact, $\text{ZnCo}_2\text{O}_4@\text{Co-Al LDH}$ nanowires on NF (2041 F g^{-1} at 1 A g^{-1})¹²⁷ (Fig. 9C),

composed of urchin-like porous ZnCo_2O_4 nanowires, which were uniformly covered with Co-Al LDH nanosheets, delivered higher specific capacitance and rate-capability than pristine ZnCo_2O_4 , Ni-Al LDH and Co-Al LDH, and core@shell $\text{ZnCo}_2\text{O}_4@\text{Ni-Al LDH}$ electrodes, retaining 70% of the initial capacitance at 10 A g^{-1} due to the increase in specific surface area, the high electroactivity of the Co-Al LDH shell, and band alignments between ZnCo_2O_4 and Co-Al LDH, thus facilitating the charge transfer.

3.1.3. $\text{ZnCo}_2\text{O}_4/\text{carbon}$ material composite electrodes.

Several carbonaceous materials can be derived from ZnCo_2O_4 as composites encompassing carbon nanotubes (CNTs),^{129,134} carbon nanoparticles,^{97,100} N-doped carbon,¹³² reduced graphene oxide (rGO),^{106,130,133} polyaniline (PANI)^{131,136} and graphitic-carbon nitride ($\text{g-C}_3\text{N}_4$)¹³⁵ in slurry-cast electrodes, and carbon,¹⁴³ N-doped carbon,^{138,140} rGO,^{109,137,139,141,142} polyvinylpyrrolidone (PVP)⁶⁶ and polypyrrole (PPy)^{57,144} in binder-free electrodes. Accordingly, it should be possible to explore the combined effects of electric double-layer capacitance (EDLC) from carbonaceous materials, and pseudocapacitance from transition metal oxide materials. In this way, one could overcome the inherent limitations of these carbon materials, *e.g.*, low specific capacitance, and of ZnCo_2O_4 , *e.g.*, low electronic conductivity. They can hinder charge transfer, resulting in low capacitance and poor rate capability, including cyclability, in accordance with theoretical expectations.¹⁰⁰

Polymers, *e.g.*, PANI,^{131,136} $\text{g-C}_3\text{N}_4$ ¹³⁵ and PVP,⁶⁶ can act as support materials for ZnCo_2O_4 , while PPy^{57,144} has been explored as a shell material in core@shell architectures. Embedding ZnCo_2O_4 in $\text{g-C}_3\text{N}_4$, a mesoporous sheet-like soft polymer, can produce $\text{g-C}_3\text{N}_4@\text{ZnCo}_2\text{O}_4$ (1386 F g^{-1} at 4 A g^{-1})¹³⁵ (Fig. 10A) with the benefit of the highly active nitrogen sites, large

specific surface area and good overall stability, in addition to low-cost. However, in comparison to pristine ZnCo_2O_4 , only 66% of the initial specific capacity was maintained for a 2-fold density current increase. PVP is a bulky, non-toxic, non-ionic polymer containing carbonyl, amine, and alkyl functional groups that can be used as a surfactant, reducing agent, shape controlling agent, and dispersant in nanoparticle synthesis. The self-assembly of PVP was used to produce binder-free hierarchical microflowers of $\text{ZnCo}_2\text{O}_4/\text{PVP}$ composites (761 F g^{-1} at 0.35 A g^{-1})⁶⁶ (Fig. 10B) *via* an assisted hydrothermal method. These materials presented relatively poor rate capability, as expected for a flower-like structured material-based binder-free electrode. Notwithstanding, PANI, a semi-flexible rod-like polymer, exhibits a good electrical conductivity with multi-redox activity involving protonation, and can modify ZnCo_2O_4 particles' sizes and shapes thanks to its strong interactions, shortening electron/ion pathways and increasing surface area due to interconnective rod-like structures. As a result, nanosheet-like $\text{ZnCo}_2\text{O}_4/\text{N-GO}/\text{PANI}$ (720 F g^{-1} at 1.5 A g^{-1})¹³¹ (Fig. 10C), based on $\text{ZnCo}_2\text{O}_4/\text{N-GO}$ coverage with multifaceted PANI, and PANI/ ZnCo_2O_4 nanoparticle (867 F g^{-1} at 0.5 A g^{-1})¹³⁶ (Fig. 10D) slurry-cast electrodes exhibited significant changes in size, shape, specific surface area, bond length, electron density, and other parameters. Both delivered excellent cyclability and specific capacitance in comparison to the $\text{ZnCo}_2\text{O}_4/\text{N-GO}$ nanocomposite¹³¹ and pristine ZnCo_2O_4 NPs.¹³⁶

PPy is considered to be a promising electrode material owing to its high electrical conductivity, greatly improving the specific capacitance and cycle performance as well as decreasing the overpotential attributed to the promotion of electron transport and reduction of internal resistance.^{57,144} $\text{ZnCo}_2\text{O}_4@\text{PPy/NF}$ (1210 F g^{-1} at 1 A g^{-1})⁵⁷ (Fig. 10E), architectured as

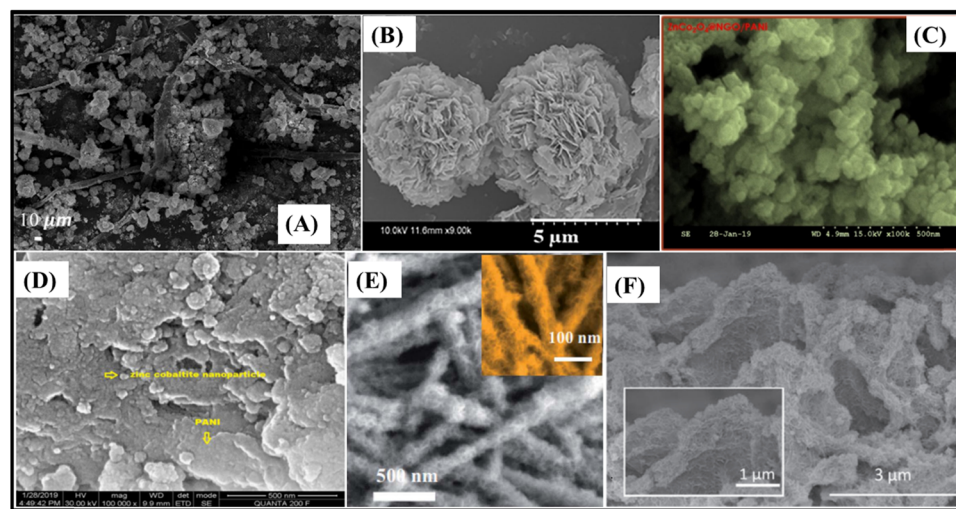


Fig. 10 SEM images of (A) nanosheet-like $\text{g-C}_3\text{N}_4/\text{ZnCo}_2\text{O}_4$,¹³⁵ (B) 3D flower-like $\text{ZnCo}_2\text{O}_4/\text{PVP}$,⁶⁶ (C) nanosheet-like $\text{ZnCo}_2\text{O}_4/\text{N-GO}/\text{PANI}$,¹³¹ (D) $\text{PANI}/\text{ZnCo}_2\text{O}_4$ nanoparticles,¹³⁶ (E) $\text{ZnCo}_2\text{O}_4@\text{PPy}$ nanostructures/NF⁵⁷ and (F) core@shell $\text{ZnCo}_2\text{O}_4@\text{NiCo}_2\text{S}_4@\text{PPy}$.¹⁴⁴ Panel A: Reproduced with permission.¹³⁵ Copyright © 2020, The Author(s). Panel B: Reproduced with permission.⁶⁶ Copyright © 2020 John Wiley & Sons Ltd. Panel C: Reproduced with permission.¹³¹ © 2020 Elsevier B.V. All rights reserved. Panel D: Reproduced with permission.¹³⁶ Copyright © 2019, Springer-Verlag GmbH Germany, part of Springer Nature. Panel E: Reproduced with permission.⁵⁷ CC BY 3.0. Royal Society of Chemistry. Panel F: Reproduced with permission.¹⁴⁴ Copyright Marketplace™. IOP Publishing.



ultrathin PPy film-coated ZnCo_2O_4 nanowires, delivered about 9 times more specific capacitance than pristine spinel species. On the other hand, the core@shell $\text{ZnCo}_2\text{O}_4@\text{NiCo}_2\text{S}_4@\text{PPy}/\text{NF}$ electrode (2507.0 F g^{-1} and 3.75 F cm^{-2} at 0.5 A g^{-1})¹⁴⁴ (Fig. 10F) presented much better rate-capability, with 69% capacitance retention after a 40-fold increase in current density. This result is associated with its composition, since NiCo_2S_4 exhibits abundant valence states and high theoretical specific capacitance in addition to the more suitable architecture. It resembles porous leaf-like ZnCo_2O_4 nanosheets covered hierarchically with thin and abundant NiCo_2S_4 nanosheets and a thin PPy film. This core@shell structure formed by three materials created a bi-interface that can promote the contact with the electrolyte and facilitate ion-diffusion, accelerate the electron transfer, and increase the availability of electroactive sites. However, PPy can contribute to the pseudocapacitance through doping and de-doping redox reactions, increasing the volume changes along the cycling and thus reducing the mechanical stability of the material. Slightly poorer cycling stability than that of $\text{ZnCo}_2\text{O}_4@\text{NiCo}_2\text{S}_4/\text{NF}$ was observed, without PPy coating, but, in contrast, the specific capacitance almost doubled after the coating.

Carbon (C) is also considered to be a promising candidate to form a composite material for ZnCo_2O_4 -based electrodes in supercapacitive applications, due to its good volume expansion tolerance and excellent electron transport. The use of C can effectively improve the overall electrical conductivity of the material, decrease the volume expansion, and inhibit the agglomeration of ZnCo_2O_4 in the redox reaction process, thus improving the specific capacitance and cycling stability. This is the case of the core@shell $\text{ZnCo}_2\text{O}_4@\text{C}/\text{NF}$ electrode (2340 F g^{-1}

and 7.02 F cm^{-2} at 1 mA cm^{-2})¹⁴³ composed of agglomerated ZnCo_2O_4 nanoparticles as porous nanowire arrays, covered with a thin amorphous carbon layer, leading to high specific capacitance and good cycling stability (capacitance retention of 92.6% after 10 000 cycles).

Notwithstanding, N-doped carbon (NC) supported P- ZnCo_2O_4 nanosheets (1581.5 F g^{-1} at 1 A g^{-1})¹³² (Fig. 11A), in which the NC acted as a 3D continuous network, provided a highly electrically conductive support with large surface area for the growth of P-doped ZnCo_2O_4 nanosheets. They showed much better results, with 90.6% rate capability after a 10-fold current density increase. The triangular-shaped P-doped ZnCo_2O_4 nanosheets are rich in oxygen vacancies, due to their substitution for phosphorus ions. In this way, ion-diffusion and the absorption of OH^- are facilitated. There are a large interface contact area and shortened electron/ion diffusion paths, which is an interesting strategy to improve ZnCo_2O_4 electrochemical performances in slurry-cast electrodes.

As for binder-free electrodes, in recent years the relevant systems studied were $\text{ZnCo}_2\text{O}_4/\text{NC}$ hollow nanowall arrays/flexible carbon textiles (CT) ($\sim 2003.8 \text{ F g}^{-1}$ at $\sim 1.79 \text{ A g}^{-1}$)¹³⁸ and NC/ ZnCo_2O_4 honeycomb-like nanostructures (1289 F g^{-1} at 3.5 A g^{-1})¹⁴⁰ (Fig. 11B) is based on NC hollow nanowall arrays that serve as the backbone and conductive connection for porous ultrathin ZnCo_2O_4 nanoflakes. They increase the contact area with the electrolyte and enable fast redox reaction, featuring high specific surface area and short ion diffusion paths. This leads to high rate-capability and cycling stability, with 74.7% and $\sim 99.4\%$ capacitance retention, when increasing the current density to 57.14 A g^{-1} and after 10 000 cycles, respectively. The second one¹⁴⁰ (Fig. 11C)

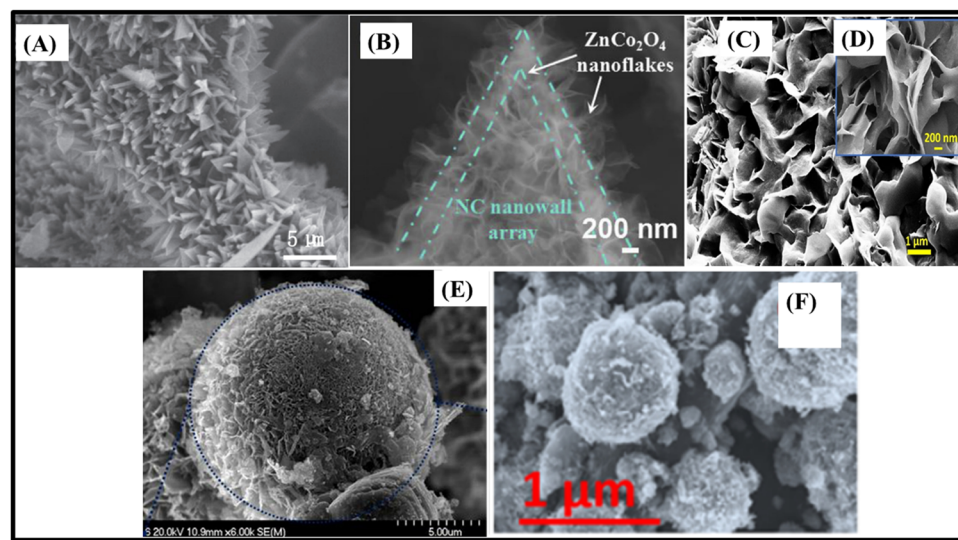


Fig. 11 (A) SEM image of N-doped C supported P- ZnCo_2O_4 nanosheets.¹³² (B) TEM image of $\text{ZnCo}_2\text{O}_4/\text{N-doped carbon hollow nanowall arrays/CT}$.¹³⁸ SEM images of (C and D) N-doped carbon/ ZnCo_2O_4 honey nest nanostructures.¹⁴⁰ (E) cauliflower-like AuNP/rGO- ZnCo_2O_4 ¹³³ and (F) NiCo_2O_4 - $\text{ZnCo}_2\text{O}_4/\text{rGO}$ nanosheets.¹⁰⁶ Panel A: Reproduced with permission.¹³² © 2020 Elsevier B.V. All rights reserved. Panel B: Reproduced with permission.¹³⁸ © 2019 Published by Elsevier B.V. Panels C and D: Reproduced with permission.¹⁴⁰ Copyright © 2020, Springer Science Business Media, LLC, part of Springer Nature. Panel E: Reproduced with permission.¹³³ Copyright © 2019 Elsevier B.V. All rights reserved. Panel F: Reproduced with permission.¹⁰⁶ Copyright © 2020 American Chemical Society.



shows less competitive performance, but it involves an interesting strategy for the production of NC using high fructose corn syrup as a green, abundant, and inexpensive carbon source for producing 3D porous ultrathin nanoflakes in a honeycomb-like morphology. The arrangement facilitates the penetration of the electrolyte, providing small contact impedance, and improved ion and electron transportation, yielding relatively good rate capability and cycling stability, with 70% and 86% capacitance retention at 20 A g^{-1} and after 2000 cycles.

As for carbon nanoparticles (CNPs), there are examples in which they were dispersed onto $\text{ZnO}/\text{ZnCo}_2\text{O}_4$ nanosheets to produce $\text{CNP}/\text{ZnO}/\text{ZnCo}_2\text{O}_4$ derivatives (593.6 F g^{-1} at 0.25 A g^{-1}).¹⁰⁰ Electrospun 1D $\text{ZnCo}_2\text{O}_4/\text{C}$ nanofibers, consisting of a ZnCo_2O_4 and carbon nanoparticle mixture (327.5 F g^{-1} at 0.5 A g^{-1}), have also been reported.⁹⁷ Both materials don't use carbon as a conductive support, but in the form of dispersed nanoparticles. Therefore, the ions should diffuse through them to reach the electroactive material. As a result, they present low specific capacitances and very poor rate capabilities, despite the high cycling stability due to their optimized morphologies and CNP incorporation.^{97,100}

Other highly conductive carbon materials, such as CNTs¹²⁹ and rGO,^{106,133} have also been studied as supports for ZnCo_2O_4 in slurry cast electrodes, and both presented remarkable results. It should be noted that rGO has a large specific surface area, high electrical conductivity, good thermal stability, and excellent mechanical flexibility, displaying all benefits of 2D morphologies and superb possibilities as a support material. Nonetheless, $\pi-\pi$ interactions and van der Waals forces between graphene sheets cause a restacking effect of rGO at higher current densities. This can limit its electrochemical performance, due to reduction in the specific surface area and creation of difficult channels for electrolyte ion transportation.

The cauliflower-like $\text{AuNP}/\text{rGO}-\text{ZnCo}_2\text{O}_4$ (54.1 mA h g^{-1} at 25 mA cm^{-2})¹³³ (Fig. 11D) was based on the incorporation of AuNPs within rGO nanosheets to prevent the restacking effect. However, rGO nanosheets were coated with flower-like ZnCo_2O_4 in order to increase their specific surface area. Therefore, this material did not work as a support material. The electrode delivered low specific capacity although it presented high cycling stability. In contrast, heterostructured $\text{NiCo}_2\text{O}_4-\text{ZnCo}_2\text{O}_4/\text{rGO}$ nanosheets (2176.4 F g^{-1} at 1 A g^{-1})¹⁰⁶ (Fig. 11E), composed of spherical $\text{NiCo}_2\text{O}_4@/\text{ZnCo}_2\text{O}_4$ heterostructures (urchin-like NiCo_2O_4 and sheetlike ZnCo_2O_4) that were supported on rGO nanosheets, delivered the highest specific capacitance among all reviewed slurry-cast electrodes. This material afforded 58.2% rate capability after a 20-fold current density increase and 93.8% capacitance retention after 5000 charge/discharge cycles. Not coincidentally, the three best slurry-cast electrodes were those based on $\text{NiCo}_2\text{O}_4-\text{ZnCo}_2\text{O}_4$ composites supported onto rGO.

Binder-free electrode materials based on ZnCo_2O_4 and rGO composites have also been studied in recent years.^{109,137,139,141,142} $\text{ZnCo}_2\text{O}_4/\text{rGO}$ intertwined sheets on NF (3222 F g^{-1} at 1 A g^{-1})¹³⁷ (Fig. 12A) presented specific capacitance superior to other ZiCo -based composite materials containing rGO such as ZnCo -layered double hydroxide@rGO/NF (2142.0 F g^{-1}),¹⁴⁵ ZnCo -sulfide-rGO 3D hollow microsphere flowers (1225.1 F g^{-1}),¹⁴⁶ and $\text{CoO-ZnO}/\text{rGO/NF}$ (1951.8 F g^{-1}),¹⁴⁷ but with poor rate capability and cycling stability, retaining only 26.7% and 65% after a 20-fold current density increase and 5000 cycles. This is due to the slow ion-diffusion rates induced by the fused porous ultrathin ZnCo_2O_4 curl nanosheets coated onto the vertically interconnected rGO nanosheets, limiting the penetration of electrolyte. Porous ZnCo_2O_4 nanosheets directly grown on rGO-coated NF (680 F g^{-1} at 1 A g^{-1})¹⁴² presented the poorest specific capacitance among all reviewed electrodes, but it is inferred that the

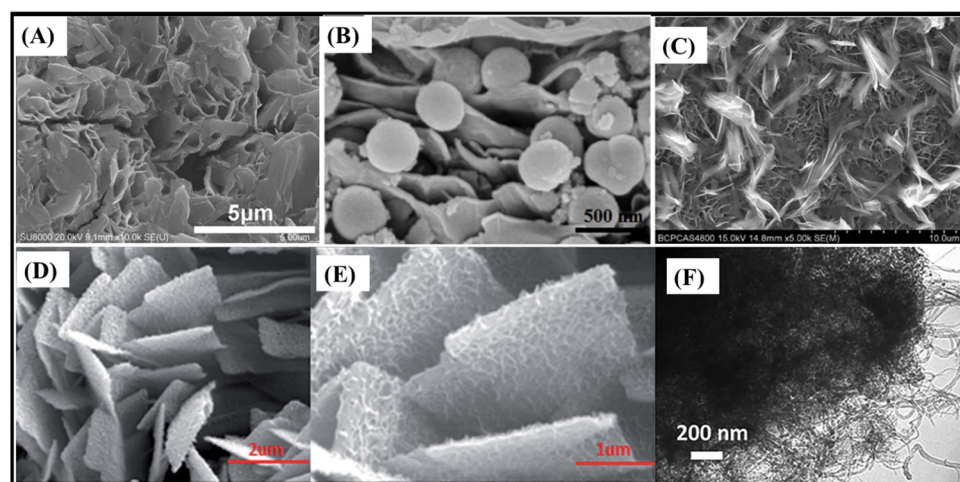


Fig. 12 SEM images of (A) $\text{ZnCo}_2\text{O}_4/\text{rGO}$ intertwined sheets/NF,¹³⁷ (B) sandwich-like ZnCo_2O_4 hollow spheres/rGO lamellar film,¹³⁹ (C) heterostructured $\text{ZnCo}_2\text{O}_4/\text{N-rGO}/\text{NF}$,¹⁴¹ and (D and E) MnO_2 -decorated ZnCo_2O_4 nanosheets on rGO-doped NF.¹⁰⁹ (F) TEM image of $\text{ZnCo}_2\text{O}_4/\text{CNT}$ nanoflowers.¹²⁹ Panel A: Reproduced with permission.¹³⁷ Copyright © 2018 Elsevier B.V. All rights reserved. Panel B: Reproduced with permission.¹³⁹ Copyright © 2020 Published by Elsevier B.V. Panel C: Reproduced with permission.¹⁴¹ CC BY-NC 3.0. Royal Society of Chemistry. Panels D and E: Reproduced with permission.¹⁰⁹ CC BY-NC 3.0. Royal Society of Chemistry. Panel F: Reproduced with permission.¹²⁹ Copyright © 2019 Elsevier B.V. All rights reserved.



rGO can effectively buffer ZnCo_2O_4 nanosheets' volume changes through cycling and enhance the electrical conductivity. It can act as bridges for electron transfer, but the rGO-coated NF seems to not actively promote the ion-diffusion rates, exhibiting 88% capacitance retention after just a 5-fold current density increase. Lamellar films of $\text{ZnCo}_2\text{O}_4/\text{rGO}$ hollow spheres (1075.4 F g^{-1} at 1 A g^{-1})¹³⁹ (Fig. 12B) present a sandwich-like structure. The sandwiched hollow nanospheres can expand the inner-space and minimize the aggregation of rGO, facilitating and accelerating the electrolyte diffusion and increasing the cycling stability. On the other hand, heterostructured $\text{ZnCo}_2\text{O}_4/\text{N-rGO}$ on NF (1600 F g^{-1} at 1 A g^{-1})¹⁴¹ (Fig. 12C) features ultrathin and porous honeycomb-like nanosheets and nanofeathers, with a hierarchical double-morphology. These characteristics, respectively, increase the active surface area and hinder the volume change through cycling. The N-doped rGO seems to parallelly orient the growth of ZnCo_2O_4 nanosheets, thus delivering 78.1% of the initial capacitance even after a 30-fold current density increase. Finally, MnO_2 -decorated ZnCo_2O_4 nanosheets on rGO-doped NF (3405.2 F g^{-1} at 2 A g^{-1})¹⁰⁹ (Fig. 12D and E) feature the combined benefits of composites based on MnO_2 and rGO. They were electrodeposited onto porous ZnCo_2O_4 nanosheets and on rGO-coated NF, thus delivering very high specific capacitance and good cycling stability (91.2%, 5000 cycles) but relatively poor rate capability (64.9%, 10-fold increase). In this way, they behave as porous ZnCo_2O_4 nanosheets on rGO-doped NF,¹⁴² because the rGO coating limits the ion-diffusion at higher current densities.

CNTs present all advantages of 1D materials along with the increased conductivity of a carbon material. Therefore, when used as a support and connective material, they provide improved charge and electron transfer pathways.^{129,134} A MWCNT/ ZnCo_2O_4 slurry-cast electrode (64 mA h g^{-1} at 1 A g^{-1})¹³⁴ presented nearly double the specific capacity of pristine ZnCo_2O_4 due to its hexagonal nanoplates connected by multiwalled carbon nanotubes, even though it delivered very low specific capacity and rate

capability. On the other hand, $\text{ZnCo}_2\text{O}_4/\text{CNT}$ nanoflowers¹²⁹ (Fig. 12F) delivered a high specific capacitance of 1203.8 F g^{-1} at 1 A g^{-1} , in which CNTs interpenetrate the ZnCo_2O_4 flowers acting as both a conductive additive and a buffer material. This facilitates ion diffusion rates and rapid electron transfer and reduces interior stress and volume expansion during electrochemical reactions, increasing the cycling stability and electrochemical performances of the electrode.

3.1.4. The top 10 highest specific capacitances for electrode materials based on ZnCo_2O_4 . The highest specific capacitances among pristine ZnCo_2O_4 and ZnCo_2O_4 -based composites as slurry-cast or binder-free electrodes are illustrated in Fig. 13A. The best pristine ZnCo_2O_4 -based slurry-cast electrode delivered much lower specific capacitance in comparison to the other electrodes. It is interesting to note that the highest specific capacitances of pristine binder-free and composite slurry-cast electrodes are quite similar, even though each one of these strategies is uniquely effective. Thus, the best way to improve ZnCo_2O_4 -based electrodes is to combine the rational design of composites and the production of binder-free electrodes. In fact, among the top 10 electrode materials, 9 of them are composite binder-free electrodes (Fig. 13B). In fact, the highest specific capacitance was achieved by MnO_2 -decorated ZnCo_2O_4 nanosheets on rGO-doped NF. The improved specific capacitance was provided by the additional MnO_2 -decorated electroactive material and the electrical conduction associated with the rGO-doped NF substrate used for the growth of ZnCo_2O_4 nanosheets.

Notwithstanding, there is still a possible limitation to be taken into consideration: in such architectures, the space between the nanostructures plays an important role in the ion-diffusion rates and in the availability of electroactive sites at higher current densities. This is pretty evident in binder-free electrodes based on ZnCo_2O_4 nanowires that can present very high specific capacitance, but low rate-capability. As a result, the best rate-capabilities are achieved by these binder-free

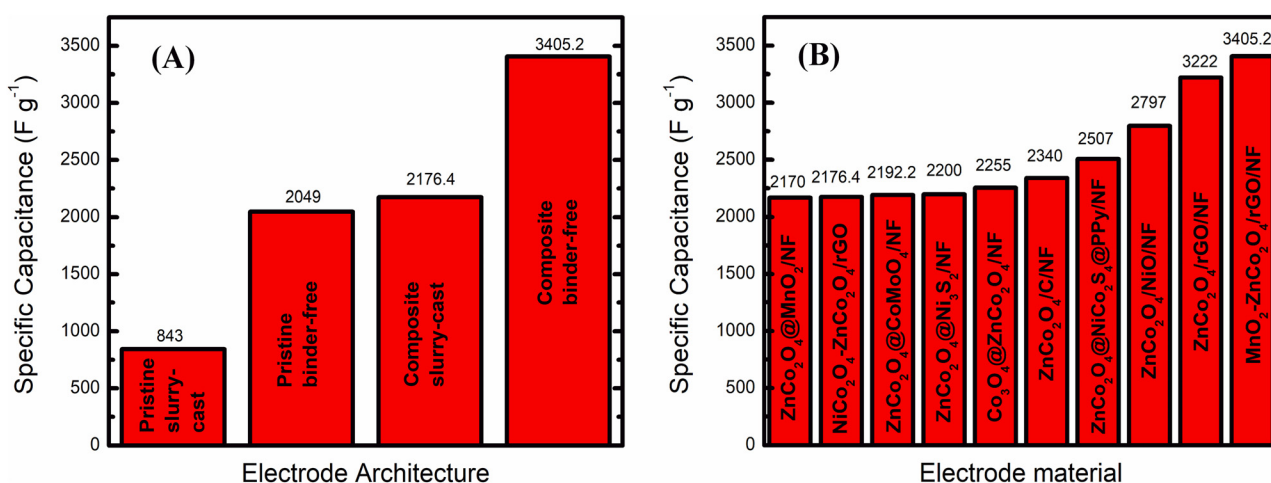


Fig. 13 (A) Best specific capacitance for each ZnCo_2O_4 -based electrode type: pristine slurry-cast; pristine binder-free; composite slurry-cast and composite binder-free (ref. 11, 26, 58 and 62, respectively). (B) Top 10 specific capacitances delivered by ZnCo_2O_4 -based electrodes (ref. 62, 43, 38, 90, 84, 67, 75, 79, 58 and 89, respectively).



electrodes with suitably spaced nanostructures and high availability of ion-diffusion channels.

3.2. Batteries

3.2.1. Lithium-ion batteries. Rechargeable Li-ion batteries (LIBs) received extensive investments because of their excellent cyclability, good safety performance, and high-energy density. Since the early 1990s, LIBs have been widely used in portable electronic and electric vehicles.¹¹ A LiCoO₂ cathode and a graphite anode are some of the most well-known commercial LIB material pairings.^{148–150} Unfortunately, so far, the traditional intercalation-type material, graphite, generally has suffered from its low theoretical specific capacity (372 mA h g⁻¹) and poor rate performance, which hinders the large-scale application of LIBs.¹⁵¹ Other potential anode materials, such as spinel-structure mixed transition metal oxides, have emerged as ideal candidates due to their higher lithium storage capacity (500–1500 mA h g⁻¹).^{11,152} Among various spinel oxides, ZnCo₂O₄ has captured great attention due to its special lithiation properties, environmental benignity, affordable price, good conductivity, and high theoretical specific capacity (900 mA h g⁻¹).^{153,154} Up to now, many types of ZnCo₂O₄ materials with different morphologies, such as nanoribbons,⁸¹ nanoboxes,¹⁵⁵ nanosheets,^{152,156,157} microcubes,¹⁵⁸ nanocubes,¹⁵⁹ nanospheres,^{160–164} nanotubes,¹⁶⁵ and nanocages,¹⁶⁶ have been applied in LIBs.

To increase mass transfer and contact between electrodes and electrolyte, Zhang *et al.*¹⁵² reported nickel foam supported hierarchical ZnCo₂O₄ nanosheets prepared by the solution-based method. A reversible specific capacity of 773 mA h g⁻¹ at 0.25 A g⁻¹ over 500 cycles was found for the porous ZnCo₂O₄ nanosheets. Song *et al.*¹⁵⁷ also reported the synthesis of ZnCo₂O₄ nanosheets; when evaluated as an anode material for LIBs, the electrode showed an initial specific capacity of 1979 mA h g⁻¹ and a stable discharge capacity of 688 mA g⁻¹ at 0.5 A g⁻¹ after 1000 cycles. Another ZnCo₂O₄ nanosheet material reported in the literature delivered a reversible capacity of 1640.8 mA h g⁻¹ at a current density of 100 mA g⁻¹ after 50 cycles.¹⁵⁶

The morphology of the material plays a crucial role in the overall electrochemical performance, and thus, various morphologies have been intensively pursued and well designed. For example, Chen *et al.*¹⁶⁰ synthesized ZnCo₂O₄ nanospheres with the desired shape *via* a one-step solution method. The ZnCo₂O₄ nanospheres showed an initial discharge capacity of 1320 mA h g⁻¹ at a current density of 100 mA g⁻¹ and a capacity retention rate of 76.22% after 50 charge and discharge cycles. Cheng *et al.*¹⁶⁷ synthesized 1D porous ZnCo₂O₄ tailored cuboids with green natural soybean oil by a micro-emulsion strategy. This material exhibited an initial coulombic efficiency of 80.6% and a specific capacity of 1029.3 mA h g⁻¹ at 1000 mA g⁻¹ over 400 cycles. Lately, Li *et al.*¹⁵³ synthesized 3D mesoporous ZnCo₂O₄ architectures by the ethylene glycol combustion strategy. The average specific capacity of the ZnCo₂O₄ electrode can return to about 778.7 mA h g⁻¹ at a current density of 200 mA g⁻¹ over 50 cycles. 3D hierarchical

ZnCo₂O₄ nanocubes prepared by a hydrothermal method delivered a reversible specific capacity of 775 mA h g⁻¹ after 100 cycles at 500 mA g⁻¹.¹⁵⁹

Hollow nanostructures have attracted considerable attention; their unique structure enables a high specific surface area, tunable chemical composition, and short charge transport pathway. Xue *et al.*¹⁶⁴ developed a universal self-template approach to synthesize multishelled hollow ZnCo₂O₄ spheres (Fig. 14A and B), which displayed a specific capacity of 1020 mA h g⁻¹ at 100 mA g⁻¹ (Fig. 14C), a cycling durability of 1200 mA h g⁻¹ after 200 cycles at 0.1 A g⁻¹ and a rate capability of 730 mA h g⁻¹ at 5.0 A g⁻¹. Similarly, Deng *et al.*¹⁶⁸ proposed a citrate-assisted hydrothermal synthesis to generate hollow ZnCo₂O₄ octahedral particles (Fig. 14D and E). Battery tests demonstrated a specific capacity of 1110 mA h g⁻¹ at 0.2 A g⁻¹ (Fig. 14F) and a capacity retention of 60% at 5 A g⁻¹ over 60 cycles.

The main electrochemical performances for ZnCo₂O₄ with different morphologies are summarized and listed in Table 6. Hollow porous structures composed of 2D structures of ZnCo₂O₄, such as nanosheets, showed superior electrochemical performance to other nanostructures or microstructures in LIBs, due to the interior hollow structure which can accommodate the huge volume expansion and provide more active lithiation sites; thus, ZnCo₂O₄ structures exhibit higher capacity and cycling stability than the other materials, and second, the porous structures ensure sufficient contact between active materials and electrolyte. Therefore, it can be concluded that 2D nanostructures of ZnCo₂O₄ would be considered as an optimum architecture for high-performance ZnCo₂O₄.

Although the theoretical capacity of ZnCo₂O₄ as an anode material is high (900 mA h g⁻¹),¹⁵⁴ tremendous efforts have been paid, in recent years, to increasing the conductivity and overcoming the volume expansion of ZnCo₂O₄ caused by lithium-ion insertion/extraction, which results in its fast fading of capacity. One strategy is the combination with transition metal oxides such as ZnO/ZnCo₂O₄/Co₃O₄,¹⁸⁰ ZnCo₂O₄/Co₃O₄,^{177–179} N-ZnCo₂O₄/CoO,¹⁸³ ZnCo₂O₄@NiO,¹⁸⁵ Ni-NiCo₂O₄@ZnCo₂O₄,¹⁸¹ and ZnCo₂O₄@Fe₂O₃–C,¹⁸² which can alleviate the problem through the synergy effect of bimetallic oxides.

The construction of hollow and 3D porous structures is another effective strategy, promoting the generation of voids, which can alleviate the structural stress and buffer the volume variation. For example, a novel route to prepare hollow Co₃O₄ nanospheres doped with ZnCo₂O₄ was demonstrated by Song *et al.*¹⁷⁹ (Fig. 15A). This nanocomposite shows a specific capacity of 890 mA h g⁻¹ at a current density of 0.1 A g⁻¹ and displays a similar specific capacity at 1 A g⁻¹ after 120 cycles (Fig. 15B). Guo *et al.*¹⁷⁷ reported the synthesis of a 3D porous ZnCo₂O₄/Co₃O₄ composite on carbon cloth (Fig. 15C). The as-prepared composite exhibits an enhanced lithium storage property of 1350.0 mA h g⁻¹ at 0.3 A g⁻¹ and a cycling performance of 64% over 105 cycles at 0.3 A g⁻¹ (Fig. 15D). Li *et al.*¹⁷⁸ also prepared ZnCo₂O₄/Co₃O₄ hierarchical hollow ZnCo₂O₄/Co₃O₄ microspheres *via* solvothermal synthesis followed by thermal annealing. When used as an anode material



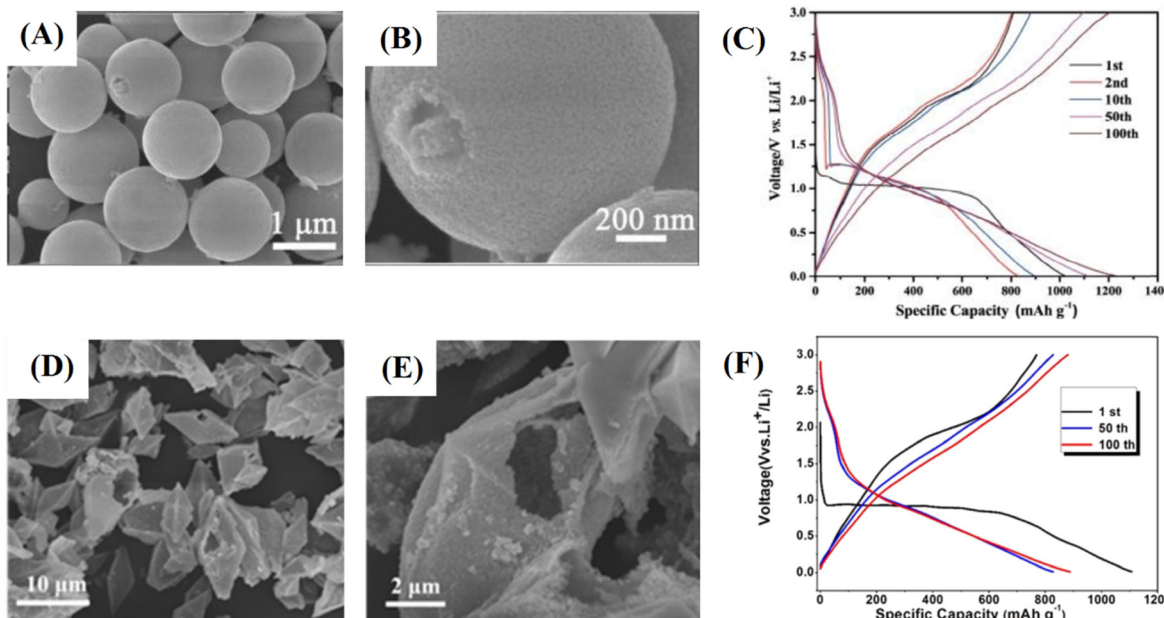


Fig. 14 (A and B) SEM images of ZnCo_2O_4 multishelled hollow spheres at different magnifications. (C) Galvanostatic charge/discharge curves of a ZnCo_2O_4 multi-shelled hollow sphere anode at a current density of 100 mA g^{-1} . Reproduced with permission.¹⁶⁴ Copyright Marketplace™. Royal Society of Chemistry. (D and E) SEM images of ZnCo_2O_4 hollow structures at different magnifications. (F) Galvanostatic charge/discharge curves of a ZnCo_2O_4 hollow anode at a current density of 0.2 A g^{-1} . Reproduced with permission.¹⁶⁸ Copyright © 2017 Published by Elsevier B.V.

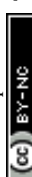
for LIBs, this material exhibits a rate capability of 842 mA h g^{-1} at a current density of 4 A g^{-1} and a cycle life of 754 mA h g^{-1} after 800 cycles at a current density of 2 A g^{-1} . The development of hollow structures based on $\text{ZnCo}_2\text{O}_4/\text{Co}_3\text{O}_4$ composites demonstrated that the hierarchical hollow structure with high porosity relieves the volume expansion and increases the contact area between the electrode and electrolyte, increasing discharge capacity and cycling performance.

Another strategy to solve concerns in terms of lithium diffusion kinetics, electronic transport, volume change, and particle agglomeration is to anchor ZnCo_2O_4 structures onto electrically conductive nanostructured carbon materials. Hence, some carbonaceous materials including carbon nanotubes (CNTs),^{129,198,199} reduced graphene oxide (rGO),^{187–192} polyaniline (PAN),²¹⁰ n-doped carbon layers,^{208,222} carbon cloth (CC),^{194,195,223} and carbon porous structures^{202–204} were used as inert and conductive matrices in ZnCo_2O_4 based anode materials. For instance, binder-free and self-supporting anode materials were prepared based on carbon-coated ZnCo_2O_4 composites. The lithium storage properties were as follows: a high initial discharge ($1951.4 \text{ mA h g}^{-1}$) and good capacity after cycling ($88.6.4 \text{ mA h g}^{-1}$ over 100 cycles at 200 mA g^{-1}).²⁰⁹ In addition, Huang *et al.*²²³ prepared a $\text{ZnCo}_2\text{O}_4@\text{CC}$ nanocomposite with a reversible capacity of 1376 mA h g^{-1} even after 200 cycles at a current density of 1 A g^{-1} .

Graphene has attracted widespread attention due to its unique properties such as mechanical flexibility, excellent conductivity (1600 S m^{-1}), large specific surface area ($2630 \text{ m}^2 \text{ g}^{-1}$), and chemical stability.^{224–227} The introduction of graphene into ZnCo_2O_4 structures can accommodate serious

volume expansion, prevent agglomeration of ZnCo_2O_4 material over continuous lithiation/delithiation cycles, and, meanwhile, improve the electrical conductivity of the hybrids.^{187,228,229} For example, Wang *et al.*¹⁹¹ prepared interconnected mesoporous ZnCo_2O_4 nanosheets on 3D graphene foam (Fig. 16A), which had a discharge capacity of 1233 mA h g^{-1} at 500 mA g^{-1} after 240 cycles (Fig. 16B). Ren *et al.*¹⁸⁸ fabricated a $\text{ZnCo}_2\text{O}_4@\text{rGO}$ nanocomposite to be used as a LIB anode. The $\text{ZnCo}_2\text{O}_4@\text{rGO}$ electrode exhibited cycling stability (1589 mA h g^{-1} at 100 mA g^{-1} after 140 cycles) (Fig. 16C). Xie *et al.* developed a rapid laser-irradiation methodology for the synthesis of oxygen-vacancy abundant nano- ZnCo_2O_4 /porous rGO hybrids as anodes for LIBs (Fig. 16E). The results showed that the nano- ZnCo_2O_4 /porous rGO has a reversible capacity of $\sim 1053 \text{ mA h g}^{-1}$ at 0.05 A g^{-1} and a cycling stability of $\sim 746 \text{ mA h g}^{-1}$ at 1.0 A g^{-1} after 250 cycles (Fig. 16D).¹⁹² In these cases, the rGO acts as a conductive substrate for anchoring the ZnCo_2O_4 structure, which increases the electrical conductivity and avoid the structure collapse upon cycling (Fig. 16F).

The combination in the composites, taking full use of the good conductivity and high surface area of carbon materials, efficaciously heightens the undesirable conductivity of ZnCo_2O_4 , thereby affording enhanced electrochemical behaviors in LIBs. The carbon coated ZnCo_2O_4 nanocomposites have large surface areas, resulting in better electrolyte wettability and high conductivity, which contribute to cycling stability. This effective approach to fabricating material composites not only has the advantages of all the constituents, but also overcomes the disadvantages of the individual components.

Table 6 Performances reported for ZnCo_2O_4 -based materials for metal ion batteries

Type	Strategy	Material	Initial discharge (mA h g ⁻¹)	Potential window (V vs.)	Reversible capacity (Nth) mA h g ⁻¹	Stability	Ref.
Li-ion	Pristine	Hollow polyhedral ZnCo_2O_4	1097.3	0.01–3 Li/Li ⁺	891.7 (200)/100 mA g ⁻¹	—	169
		ZnCo_2O_4 nanoribbons	2161	0.01–3 Li/Li ⁺	1422 (80)/200 mA g ⁻¹	71%/80 cycles	81
		Hierarchical micro-sized ZnCo_2O_4 assembled with nanosheets			1005.8 (180)/500 mA g ⁻¹	—	170
		$\text{Zn}_{1-x}\text{Co}_{3-x}\text{O}_4$ hollow nanoboxes	1141.7	0.01–3 Li/Li ⁺	625 (800)/500 mA g ⁻¹	85%/800 cycles	155
		ZnCo_2O_4 nanosheets	1197	0.01–3 Li/Li ⁺	688 (1000)/5 A g ⁻¹	—	157
		ZnCo_2O_4 nanosheets/NF	1297	0.01–3 Li/Li ⁺	773 (500)/0.25 A g ⁻¹	87%/500 cycles	152
		ZnCo_2O_4 nanosheets	1710.2	0.01–3 Li/Li ⁺	1640.8 (50)/100 mA g ⁻¹	—	156
		1D porous ZnCo_2O_4 cuboids	1376	0.01–2.5 Li/Li ⁺	1029.3 (400)/1000 mA g ⁻¹	—	167
		3D ZnCo_2O_4 nanocubes	1049	0.01–3 Li/Li ⁺	775 (100)/500 mA g ⁻¹	—	159
		ZnCo_2O_4 micro-cubes	1087	0.01–3 Li/Li ⁺	588 (1000)/1 A g ⁻¹	76%/1000 cycles	158
		Microcube-like ZnCo_2O_4			412 (600)/1200 mA g ⁻¹	—	171
		ZnCo_2O_4 nanocages	1328	0.01–3 Li/Li ⁺	1025 (200)/500 mA g ⁻¹	—	166
		Micro-ranoporous ZnCo_2O_4 spheres	1307.8	0.02–3 Li/Li ⁺	950 (90)/0.1C	99.7%/90 cycles	163
		Yolk-shell ZnCo_2O_4 microspheres	1466	0.01–3 Li/Li ⁺	1063 (50)/200 mA g ⁻¹	—	162
		Yolk-shell ZnCo_2O_4 spheres	1586	0.01–3 Li/Li ⁺	910 (300)/1 A g ⁻¹	92.3%/300 cycles	161
		Multi-shelled hollow ZnCo_2O_4 spheres	1020	0.01–3 Li/Li ⁺	1200 (200)/0.1 mA g ⁻¹	—	164
		3D ZnCo_2O_4 microspheres	2094	0.01–3 Li/Li ⁺	1296.91 (200)/100 mA g ⁻¹	—	172
		3D $\text{Zn}_{0.2}\text{Ni}_{0.8}\text{Co}_2\text{O}_4$ microspheres	1482	0.01–3 Li/Li ⁺	681 (40)/C/20	—	173
		ZnCo_2O_4 nanospheres	1320	0.01–3 Li/Li ⁺	625 (50)/100 mA g ⁻¹	76.22%/50 cycles	160
		Nanosheathed ZnCo_2O_4 spheroids	1477	0.01–3 Li/Li ⁺	815 (500)/0.1 A g ⁻¹	—	174
		Needle-like ZnCo_2O_4 octahedrons	1413	0.005–3 Li/Li ⁺	516 (50)/60 mA g ⁻¹	—	175
		3D mesoporous ZnCo_2O_4 nanoparticles	1128.0	0.01–3 Li/Li ⁺	779.6 (50)/200 mA g ⁻¹	94%/50 cycles	153
		Hollow ZnCo_2O_4 octahedrons	1110	0.01–3 Li/Li ⁺	880 (160)/0.2 A g ⁻¹	60%/60 cycles	161
		Zn defective ZnCo_2O_4 nanorods	1398.8	0.01–3 Li/Li ⁺	1140 (200)/0.4 A g ⁻¹	—	176
		ZnCo_2O_4 nanotubes	1353	0.01–3 Li/Li ⁺	1180 (275)/200 mA g ⁻¹	—	165
		3D porous $\text{ZnCo}_2\text{O}_4/\text{Co}_3\text{O}_4$	1350.0	0.01–3 Li/Li ⁺	481.9 (105)/0.3 A g ⁻¹	64.2%/105 cycles	177
		$\text{Co}_3\text{O}_4/\text{ZnCo}_2\text{O}_4$ microspheres	1567	0.01–3 Li/Li ⁺	754 (800)/2 A g ⁻¹	—	178
		$\text{Co}_3\text{O}_4/\text{ZnCo}_2\text{O}_4$	1051	0.01–3 Li/Li ⁺	890 (120)/0.1 A g ⁻¹	—	179
		3D $\text{ZnO}/\text{ZnCo}_2\text{O}_4/\text{Co}_3\text{O}_4/\text{Cu}$	1480	0.01–3 Li/Li ⁺	1428 (100)/200 mA g ⁻¹	—	180
		Ni– NiCo_2O_4 @ ZnCo_2O_4	1541	0.01–3 Li/Li ⁺	1097.5 (600)/1 A g ⁻¹	—	181
		yolk-shell nanotetrahedrons					
		ZnCo_2O_4 @ Fe_2O_3 –C	1501	0.01–3 Li/Li ⁺	952 (100)/100 mA g ⁻¹	—	182
		N-doped $\text{ZnCo}_2\text{O}_4/\text{CoO}$	1303.9	0.01–3 Li/Li ⁺	978 (500)/1 A g ⁻¹	—	183
		$\text{ZnCo}_2\text{O}_4/\text{Co}$ –B	1385	0.01–3 Li/Li ⁺	946 (1000)/1 A g ⁻¹	—	184
		3D porous ZnCo_2O_4 @ NiO/NF	1595.8	0.01–3 Li/Li ⁺	730.5 (200)/800 mA g ⁻¹	—	185
		$\text{Zn}_{1-x}\text{Co}_{x}\text{O}/\text{ZnCo}_2\text{O}_4$	1265	0.01–3 Li/Li ⁺	741 (800)/1000 mA g ⁻¹	—	186
		yolk-shell ZnCo_2O_4 spheres/rGO	1587	0.01–3 Li/Li ⁺	997 (500)/1.0 A g ⁻¹	—	187
		$\text{ZnCo}_2\text{O}_4/\text{rGO}$	1093	0.01–3 Li/Li ⁺	1613 (400)/500 mA g ⁻¹	—	188
		rGO@ ZnCo_2O_4 nanosheets	801.5	0.01–3 Li/Li ⁺	1107.2 (100)/100 mA g ⁻¹	—	189
		ZnCo_2O_4 microspheres/rGO	963.9	0.01–3 Li/Li ⁺	908.7 (500)/500 mA g ⁻¹	—	190
		ZnCo_2O_4 @3D graphene film@Ni foams	2024	0.01–3 Li/Li ⁺	1223 (240)/500 mA g ⁻¹	—	191
		Nano- ZnCo_2O_4 @rGO	~1230	0.01–3 Li/Li ⁺	~746 (250)/1 A g ⁻¹	—	192
		Graphene/porous ZnCo_2O_4	1146	0.01–3 Li/Li ⁺	791 (1000)/1 A g ⁻¹	97.3%/1000 cycles	193
		ZnCo_2O_4 –graphene	1937	0.01–3 Li/Li ⁺	1100 (2000)/4000 mA g ⁻¹	66%/2000 cycles	194
		$\text{ZnCo}_2\text{O}_4/\text{CC}$	1087	0.01–3 Li/Li ⁺	701 (60)/0.25 A g ⁻¹	—	195
		ZnCo_2O_4 @CC	1886.2	0.01–3 Li/Li ⁺	1.375 (200)/1 A g ⁻¹	—	196
		ZnCo_2O_4 nanoplates on CC	2.78 mA h cm ⁻²	0.01–3 Li/Li ⁺	3.01 mA h cm ⁻²	—	197
		$\text{ZnCo}_2\text{O}_4/\text{ZnO}/\text{carbon nanotubes}$	1893	0.005–3 Li/Li ⁺	1.440 (200)/100 mA g ⁻¹	—	198
		C/ $\text{ZnCo}_2\text{O}_4/\text{CNTs}$	1947.1	0.01–3 Li/Li ⁺	4.30.4 (1000)/2 A g ⁻¹	—	199



Table 6 (continued)

Type	Strategy	Material	Initial discharge (mA h g ⁻¹)	Potential window (V vs.)	Reversible capacity (Nth) mA h g ⁻¹	Stability	Ref.
ZnCo ₂ O ₄ @CNTs		2553	0.005–3 Li/Li ⁺	1507 (200)/100 mA g ⁻¹	—	200	
ZnCo ₂ O ₄ /CNT microflowers		1300	0.01–3 Li/Li ⁺	1200 (120)/200 mA g ⁻¹	—	129	
ZnCo ₂ O ₄ /ZnO/C		1589	0.005–3 Li/Li ⁺	800 (400)/1 A g ⁻¹	—	201	
ZnCo ₂ O ₄ -C		1521.9	0.01–3 Li/Li ⁺	622.5 (1000)/4 A g ⁻¹	—	202	
ZnCo ₂ O ₄ /C		1703.7	0.01–3 Li/Li ⁺	~760.3 (100)/0.1C	—	203	
ZnCo ₂ O ₄ /C microhydrangea		1418.1	0.01–3 Li/Li ⁺	704.4 (1000)/4 A g ⁻¹	—	204	
ZnCo ₂ O ₄ /C@carbon fibers		733	0.01–3 Li/Li ⁺	463 (100)/50 mA g ⁻¹	—	205	
Porous ZnCo ₂ O ₄ /C nanofibers		1707	0.01–3 Li/Li ⁺	1145 (100)/0.1 A g ⁻¹	—	206	
ZnCo ₂ O ₄ @INC polyhedrons		1495	0.01–3 Li/Li ⁺	1082 (300)/0.1 A g ⁻¹	—	207	
ZnCo ₂ O ₄ @INC		1592.1	0.01–3 Li/Li ⁺	1146.6 (100)/0.5 A g ⁻¹	—	208	
Carbon-coated ZnCo ₂ O ₄ nanowires		1951.4	0.01–3 Li/Li ⁺	886.4 (100)/200 mA g ⁻¹	—	209	
PAN-CE/ZnCo ₂ O ₄		927.2	0.01–3 Li/Li ⁺	787.2 (150)/100 mA g ⁻¹	—	210	
ZnCo ₂ O ₄ @C ₃ N ₄ B		1636.34	0.01–3 Li/Li ⁺	919.76 (500)/0.2 A g ⁻¹	97.8%/1000 cycles	211	
ZnCo ₂ O ₄ /CSF		3164	0.01–3 Li/Li ⁺	778 (100)/100 mA g ⁻¹	—	212	
Hybrid carbon/ZnCo ₂ O ₄ nanotubes		2247	0.01–3 Li/Li ⁺	494 (600)/5 A g ⁻¹	75%/600 cycles	213	
ZnCo ₂ O ₄ /NiCl ₂ -xF _x hydrate		1312	0.01–3 Li/Li ⁺	700 (1000)/1 A g ⁻¹	—	214	
Ni-substituted ZnCo ₂ O ₄ nanograins		1067	0.01–3 Li/Li ⁺	386 (100)/1 A g ⁻¹	68%/100 cycles	215	
N-doped ZnCo ₂ O ₄ nanoparticles		1025	0.01–3 Li/Li ⁺	650 (100)/1C	63%/100 cycles	216	
ZnCo ₂ O ₄ @Ag hollow spheres		830	0.01–3 Li/Li ⁺	616 (900)/1 A g ⁻¹	—	217	
ZnCo ₂ O ₄ nanowires		~1180	0.01–2.5 Na/Na ⁺	70.8 (100)/100 mA g ⁻¹	—	218	
ZnCo ₂ O ₄ nanosheets		~1150	0.01–2.5 Na/Na ⁺	191.9 (100)/100 mA g ⁻¹	—	218	
Zn _x Co _{3-x} O ₄ hollow nanoboxes		350	0.01–3 Na/Na ⁺	310 (100)/200 mA g ⁻¹	90.4%/100 cycles	155	
ZnCo ₂ O ₄ nanosheets		415.1	0.01–3 Na/Na ⁺	330 (100)/100 mA g ⁻¹	—	219	
ZnCo ₂ O ₄ nanosheets		800	0.01–3 Na/Na ⁺	463 (60)/0.1 A g ⁻¹	—	219	
Yolk-shell ZnCo ₂ O ₄ spheres/rGO		827.7	0.01–3 Na/Na ⁺	280 (1000)/1.0 A g ⁻¹	—	187	
ZnCo ₂ O ₄ @rGO		407	0.01–3 Na/Na ⁺	1.34 (300)/100 mA g ⁻¹	—	220	
ZnCo ₂ O ₄ /rGO		569.3	0.01–3 Na/Na ⁺	101.7 (500)/1000 mA g ⁻¹	—	221	

CC: carbon cloth, CF: carbon fiber, CNTs: carbon nanotubes, CSF: carbonized silk fabric, NC: N-doped carbon, NF: nickel foam, PAN: polyaniiline, rGO: reduced graphene oxide.

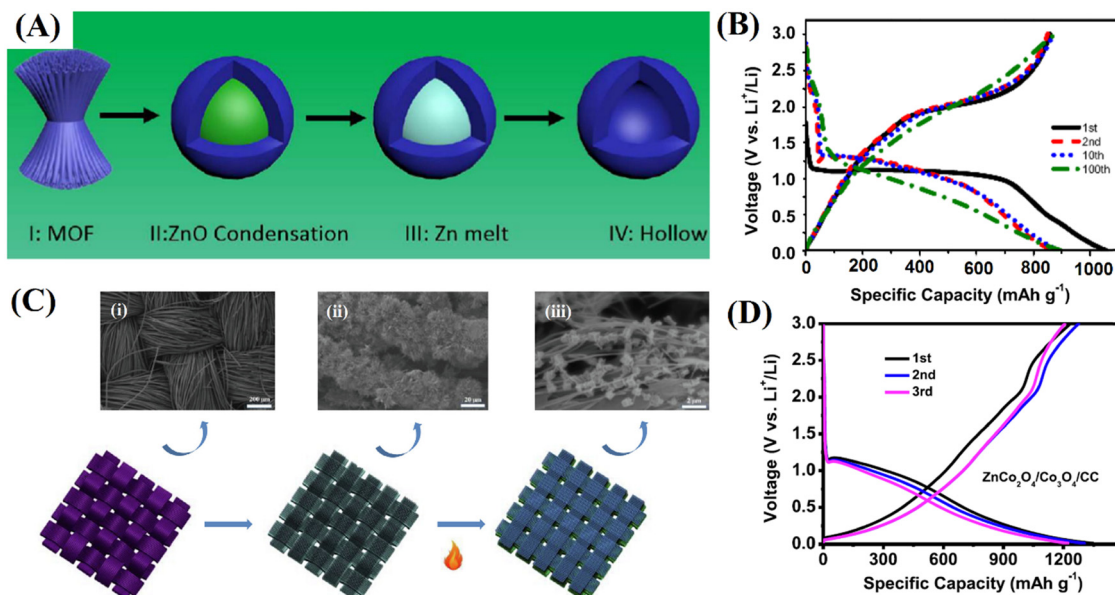


Fig. 15 (A) Schematic representation of the formation process of the hollow structure. (I) ZnCo MOF growth; (II) ZnO condensation to the middle of the pyrolyzed particle; (III) Zn reduction and melt from the middle; and (IV) hollow Co₃O₄ doped with ZnCo₂O₄ after losing Zn. (B) Charge/discharge curves of hollow Co₃O₄/ZnCo₂O₄ spheres at 0.1 A g⁻¹. Reproduced with permission.¹⁷⁹ Copyright © 2018 Published by Elsevier B.V. (C) Schematic illustration of a ZnCo₂O₄/Co₃O₄ composite grown on carbon cloth; SEM images of (i) carbon cloth; (ii) Zn/Co precursor/CC; and (iii) ZnCo₂O₄/Co₃O₄/CC. (D) Charge–discharge curves at a current density of 0.1 A g⁻¹ Reproduced with permission.¹⁷⁷ Copyright © 2020 Elsevier B.V. All rights reserved.

From the perspective of material application, an energy storage device balances the power supply and demand of large-grid energy storage. Several factors can be addressed to evaluate the performance of an electrode material in a battery cell, such as first discharge, stability, reversible capacity and the potential window. Among the many types of ZnCo₂O₄ materials previously shown, we summarize in Fig. 17 the electrodes with the 10 biggest first discharge. The best one is the ZnCo₂O₄/carbonized silk fabric (CSF) (3164 mA h g⁻¹); the high initial discharge of this material is endowed by the hydrothermal method that improves the bonding between active materials and the flexible substrate, and avoids capacity reduction from the active substance detaching from the substrate during the charge and discharge cycle; the unique weave structure of the CSF gives it good mechanical flexibility and the 3D network structure of the CSF provides a fast electron transport path to enhance the composite material's energy storage performance.²¹²

Nine out of the top ten anode materials demonstrate the benefits of a nanocomposite based on ZnCo₂O₄/carbon nanomaterials. Use of these nanocomposites was shown to be a remarkable strategy to improve the electrochemical performance of anode electrodes, as the carbon nanomaterials have many great electrochemical abilities, including enhancing the electrical conductivity of the electrode and preventing the volume change and aggregation found with ZnCo₂O₄ electrodes. The second (ZnCo₂O₄@CNTs, 2553 mA h g⁻¹),²⁰⁰ seventh (C/ZnCo₂O₄/CNT, 1947.1 mA h g⁻¹)¹⁹⁹ and ninth (ZnCo₂O₄/ZnO/CNT, 1893 mA h g⁻¹)¹⁹⁸ materials with the best performances demonstrate the advantages due to the presence of carbon nanotubes; this can be attributed to the efficient

electron transport and CNT network, which could shorten the diffusion pathway of lithium-ions and buffer the volume expansion/constriction, as well as enlarge the surface area for more electrochemically active species.²⁰⁹ Likewise, the tenth (ZnCo₂O₄@CC, 1886.2 mA h g⁻¹),¹⁹⁶ eighth (ZnCo₂O₄–graphene, 1937 mA h g⁻¹),¹⁹⁴ sixth (carbon-coated ZnCo₂O₄ nanowires, 1951.4 mA h g⁻¹),²⁰⁹ fifth (ZnCo₂O₄@3D graphene film@Ni foam, 2024 mA h g⁻¹)¹⁹¹ and third (hybrid carbon/ZnCo₂O₄ nanotubes, 2247 mA h g⁻¹)²¹³ best materials demonstrate improved electrochemical performance, which may be assigned to the carbon nanomaterial structure, which can enlarge the electrode–electrolyte contact area, greatly strengthen the electroconductivity and structural stability and improve the energy density.

It's worth highlighting that the second, seventh and tenth best materials mentioned above are based on MOF-derived materials. This strategy of preparation of materials has many advantages; for example, it endows the materials with large specific area, regular porosity, shearing capability and topological diversity, which can demonstrate that the best electrochemical performance is associated with the effects of the preparation method and the electrode architecture.²³⁰ The fourth (ZnCo₂O₄ nanoribbons, 2161 mA h g⁻¹)⁸¹ best material had its highlighted role due to its unique morphology, as well as the tenth best materials. In fact, the size of nanostructures of ZnCo₂O₄ provided more active sites, large surface area and shorter diffusion paths for ions and electrons, bringing remarkable enhancement in their electrochemical performance.^{81,196}

In summary, ZnCo₂O₄ with excellent electrochemical performance should have nanostructures or a unique morphology or be associated with a carbon nanomaterial as a nanocomposite.



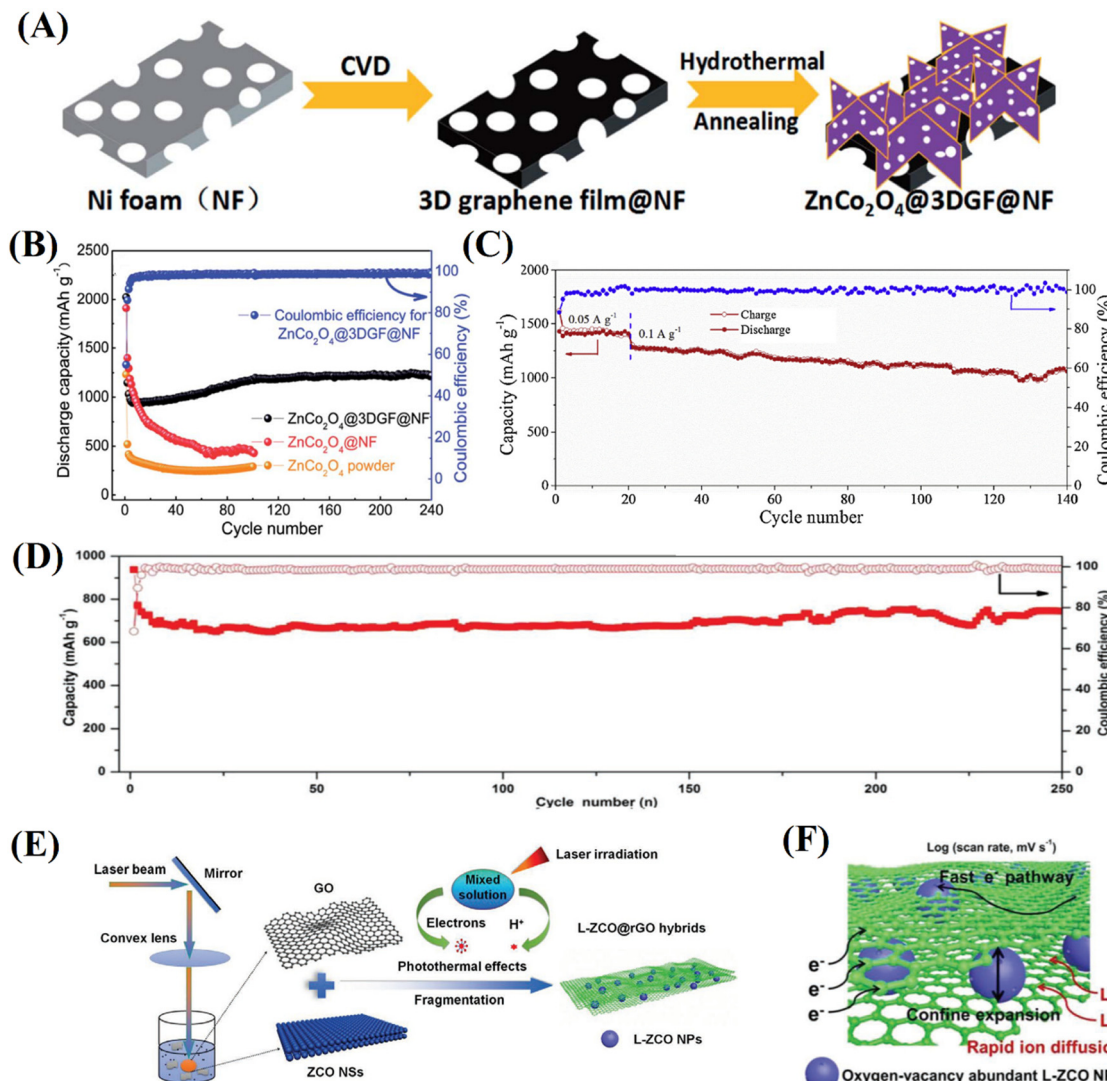


Fig. 16 (A) Schematic illustration of the synthesis of ZnCo_2O_4 @3D graphene foam@nickel foam composites. (B) Comparison of cycle performance of the ZnCo_2O_4 @3DGF@NF, ZnCo_2O_4 @NF, and ZnCo_2O_4 powder electrodes at a current density of 500 mA g^{-1} . Reproduced with permission.¹⁹¹ CC BY-NC 3.0. Royal Society of Chemistry. (C) Cycling capacity of the ZCO@rGO/LiCoO₂ full cell at a current density of 100 mA g^{-1} . Reproduced with permission.¹⁸⁸ Copyright © 2018 Elsevier Ltd. All rights reserved. (D) Cycling performance and coulombic efficiency data at 1.0 A g^{-1} of L-ZCO@rGO-30. (E) The schematic diagram for the formation of L-ZCO@rGO hybrids. (F) Schematic illustration of the fast electron/ion transfer and rapid electrochemical kinetics of the L-ZCO@rGO-30 electrode. Reproduced with permission.¹⁹² Copyright © 2020 Wiley-VCH Verlag GmbH & Co. KGaA, Weinheim.

These improved electrochemical performance can be attributed to the greater number of electrochemically active sites, the high surface area, a good diffusion length of ions and electrons, and a satisfactory volume expansion from the insertion/extraction of Li ions.

3.2.2. Other metal ion batteries. Sodium-ion batteries (SIBs), as appropriate energy storage systems for large-scale applications, have gained a lot of attention as alternative energy storage technologies to LIBs, due to abundant sodium resources and their low cost.^{49,231} As previously reported for LIBs, ZnCo_2O_4 -based materials are attractive candidates as SIB anode materials due to their low cost, high theoretical specific capacity, high specific surface area, and fast ion-diffusion.^{219,220,232} ZnCo_2O_4 nanowires and nanosheets as SIB electrode materials were studied by Zhao and collaborators.²⁰⁹ They prepared ZnCo_2O_4 nanosheets and nanowires aiming for electrochemical applications. Results

indicated that ZnCo_2O_4 nanosheet and nanowire anodes achieved 191.9 mA h g^{-1} and 70.8 mA h g^{-1} after 100 cycles at 100 mA g^{-1} , respectively. Recently, materials obtained by other strategies have been considered for application as anode materials; for example, Yang *et al.*²²⁰ prepared a polyhedron ZnCo_2O_4 anchored onto rGO nanosheets via the hydrothermal method. This composite electrode displays good cycling performance, with a discharge capacity of 134 mA h g^{-1} after 300 cycles. To improve capacity over cycles, Zhang *et al.*¹⁸⁷ designed novel yolk-shell structured ZnCo_2O_4 spheres anchored onto rGO sheets. This unique structure provides superior properties with an initial discharge capacity of 827.7 mA h g^{-1} and a reversible capacity of 280 mA h g^{-1} at 1.0 A g^{-1} after 1000 cycles. Table 6 summarizes the electrochemical performance of electrodes with different materials, coupled with distinct types of anodes based on ZnCo_2O_4 .



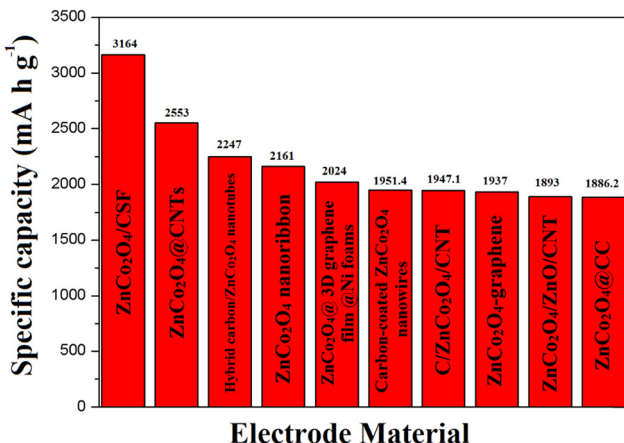


Fig. 17 The ZnCo₂O₄ electrode materials with the top 10 highest first specific capacity in LIBs.

In addition to SIBs, Zn-ion and Mg-ion batteries afford some attributes required of an alternative energy storage technology, such as nondendritic formations, Zn and Mg metal anode material delivers a high capacity of 820 mA h g⁻¹ and 2205 mA h g⁻¹, respectively, and abundant and non-toxic raw materials.^{233,234} Recently, ZnCo₂O₄ structures have been developed as potential cathode materials for these types of batteries. Baby *et al.*²³⁵ reported the synthesis of a ZnMnCoO₄ cathode material with the first discharge of 109.4 mA h g⁻¹ in Zn-ion batteries, whereas Shimokawa *et al.*²³⁶ reported the synthesis of ZnCo₂O₄ used as a cathode material for rechargeable magnesium batteries with a discharge capacity in the first cycle of ~100 mA h g⁻¹.

3.2.3. Lithium-sulfur batteries. To replace current LIBs, lithium-sulfur (Li-S) batteries are considered to be the most potential energy storage systems due to the high theoretical specific capacity (1675 mA h g⁻¹) and high specific energy (2600 W h kg⁻¹) of the sulfur cathode.²³⁷⁻²⁴¹ Owing to their well-defined crystallinity and high porosity, mixed transition metal oxides are regarded as perfect selections for cathode materials, and the interstitial spaces surrounded by the octahedra interconnect into three dimensions, accommodating guest ions, *i.e.*, lithium ions.²⁴²⁻²⁴⁴ To explore the potentiality of ZnCo₂O₄ as a Li-S electrode material, Sun *et al.*²⁴² synthesized ZnCo₂O₄ porous particles anchored on N-doped rGO *via* the combined procedures of refluxing and hydrothermal treatment. ZnCo₂O₄@N-rGO when used as a cathode material for Li-S achieved 1332 mA h g⁻¹, which was maintained at 720 mA h g⁻¹ after 200 cycles. Meanwhile, Zhang and colleagues²⁴⁵ also constructed a ZnCo₂O₄-based material and researched its Li-S storage behavior. This material showed a specific capacity of 466 mA h g⁻¹ at 0.3C and 413 mA h g⁻¹ at 0.5C after 200 cycles. Yeon *et al.*²⁴³ synthesized a 2D spinel ZnCo₂O₄. When performing the electrochemical measurement, this material presented a high initial discharge of 1292.2 mA h g⁻¹ at 0.1C and a capacity retention of 84% (1C) and 86% (2C) even after 800 cycles.

3.2.4. Metal-air batteries. Metal-air batteries (MABs) such as lithium-air, iron-air, zinc-air, aluminum-air, and magnesium-air

batteries are considered to be the next-generation technology because they use oxygen from the air as the cathode, freeing up more space devoted to energy storage.²⁴⁶⁻²⁴⁹ The exceptional theoretical energy density of MABs (3505 W h kg⁻¹ for Li-O₂ batteries and 1086 W h kg⁻¹ for Zn-air batteries)²³⁷ is based on the oxygen evolution reaction (OER) and oxygen reduction reaction (ORR); in this way, these devices have been studied by several researchers, including oxygen electrode catalysts with special structures for use in rechargeable metal-air batteries.²⁵⁰ Among the oxygen electrode catalysts, spinel transition metal oxides such as MCo₂O₄ are potential cathode materials due to the abundance of the necessary raw material and the high electrocatalytic activity for the OER and ORR. ZnCo₂O₄ has been widely studied as a catalytic oxygen electrode material for MABs such as lithium-air batteries^{55,251} and zinc-air batteries.²⁵²⁻²⁵⁵ Kin *et al.*²⁵¹ fabricated highly mesoporous ZnCo₂O₄ nanofibers by simple electrospinning and used them as a cathode material in the lithium-oxygen battery. The ZnCo₂O₄ nanofiber electrode displayed excellent electrocatalytic activity and cycling stability (226 cycles with a capacity limit of 1000 mA h g⁻¹ at 500 mA g⁻¹). Mai *et al.*²⁵³ reported a catalyst with ZnCo₂O₄ submicron/nanospheres with Co_xSe_y nanosheets, which exhibited promising catalytic properties towards OER activity with an overpotential of 324 mV at 10 mA cm⁻² in 1 M KOH. In the homemade Zn-air battery test, the cathode showed a small voltage gap (0.98 V at 50 mA cm⁻²), high power density (212.9 mW cm⁻²) (Fig. 18A) and high specific capacity (570.1 mA h g⁻¹). Costa and co-workers²⁵² documented the fabrication of a novel W-Co oxide bifunctional catalyst for the air electrode in Zn-air batteries. The conformal layer of W-Co oxide was transformed into cubic spinel ZnCo₂O₄ nanoparticles which provided excellent bifunctional catalytic activity and a good performance in the Zn-air battery test with a maximum power density of 216.4 mW cm⁻² (Fig. 18B).

To improve catalyst performance, composite materials have been synthesized and used as catalysts in both the ORR and OER. Generally, metal oxides combined with carbon materials such as graphene and carbon nanotubes (CNTs) can not only improve the conductivity of the catalyst but also increase the specific surface area and improve electrochemical stability.²⁵⁴⁻²⁵⁷ Combining Co/ZnCo₂O₄ with N-doped carbon microplates interwoven with CNTs, Yan *et al.*²⁵⁵ developed a Co/ZnCo₂O₄@NC-CNT-based flexible solid-state Zn-air battery with a competitive power density of 151 mW cm⁻² at 50 mA cm⁻² (Fig. 18C), robust flexibility and integrality. Xu *et al.*²⁵⁴ prepared ZnCo₂O₄/CNTs by inserting zinc ions. When used as a cathode material in a rechargeable Zn-air battery, this material exhibits a power density of 249.4 mW cm⁻², and a charge-discharge durability of 240 cycles.

4. ZnCo₂O₄-based electrocatalysts for energy conversion and storage applications

4.1. ORR electrocatalysts in energy storage

As mentioned in the previous topic, both the oxygen reduction and oxygen evolution reactions (ORR/OER) play an important



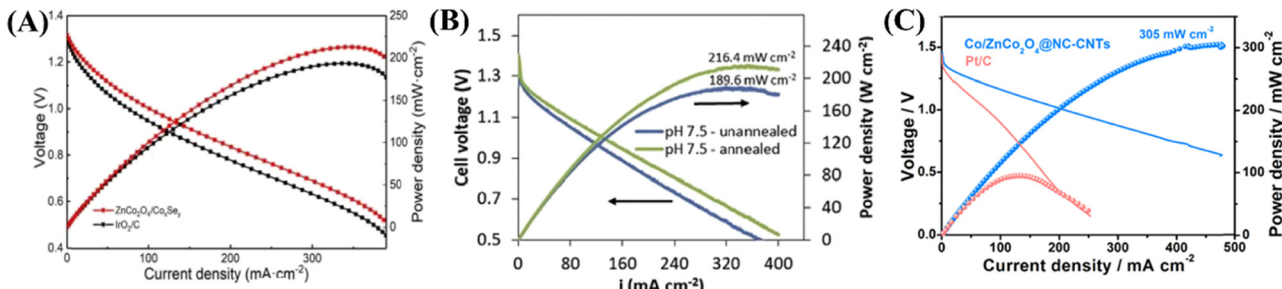


Fig. 18 Discharge polarization curves and the corresponding power density plots of a battery based on (A) $\text{ZnCo}_2\text{O}_4/\text{Co}_3\text{Se}_2$ and IrO_2/C (Reproduced with permission.²⁵³ Copyright Marketplace™. Royal Society of Chemistry), (B) annealed and unannealed W–Co oxide electrodes (Reproduced with permission.²⁵² Copyright © 2020 Hydrogen Energy Publications LLC. Published by Elsevier Ltd. All rights reserved) and (C) Pt/C and $\text{Co/ZnCo}_2\text{O}_4@\text{NC-CNTs}$ (Reproduced with permission.²⁵⁵ Copyright © 2020 Elsevier Ltd. All rights reserved).

role in the electrochemical energy conversion process, not only in metal–air rechargeable batteries but also in fuel cells.²⁵⁸ In fact, because of their high associated activation energies, such reactions are usually sluggish and require catalysts to enhance the kinetics.²³⁵ In this sense, great efforts have been directed towards the development of inexpensive, efficient, noble metal-free and stable electrocatalysts for next-generation sustainable energy technologies.²⁵⁸ Thus, ZnCo_2O_4 and its composites show great potential as electrocatalysts due to their high intrinsic activity,²⁵⁹ and in many cases exhibit both ORR and OER activity simultaneously.

As shown in Table 7, despite being considered as very promising electrocatalysts, less than two dozen ZnCo_2O_4 -based materials have been reported in the past 5 years for application in the ORR, indicating that these materials are still to be explored, especially in the design of bifunctional electrocatalysts. However, some improvement strategies for these materials can be highlighted, as a guide for future research. For instance, many catalysts with different morphologies such as nanosheets,^{130,260} flower like structures¹³⁰ and near-spherical particles²³⁵ have been recently reported.

In one of these studies, Chakrabarty *et al.*²⁶¹ synthesized a flower-like porous ZnCo_2O_4 microstructure by the one-step solvothermal method, as confirmed by SEM and HRTEM images (Fig. 19A and B). The ZnCo_2O_4 microstructure achieves a nearly 4-electron assisted oxygen reduction ($n \approx 3.4$) with onset and half wave potentials observed at 0.81 V and 0.75 V vs. RHE (Table 7). It is important to highlight that despite the interesting results obtained by designing the morphology of ZnCo_2O_4 nanostructures, better results are clearly improved by the formation of composites, especially by combining them with conductive carbonaceous materials. For example, Chakrabarty *et al.*²⁶¹ also showed the activity of electrocatalysts predicated by the simultaneous growth of ZnCo_2O_4 and reduction of GO (Fig. 19D), achieving a more positive ORR onset potential (0.95 V vs. RHE) with higher cathodic peak current density compared to ZnCo_2O_4 and $n \approx 3.95$, demonstrating that the presence of a conductive matrix is essential in the design of high-performance electrocatalysts. Furthermore, the bifunctional electroactivity of the rGO– ZnCo_2O_4 and ZnCo_2O_4 was determined from the potential difference (ΔE) between the

OER (E_{OER} , at 10 mA cm⁻²) and ORR (E_{ORR} , at -3 mA cm⁻²). The ΔE for rGO– ZnCo_2O_4 was 0.679 V vs. RHE (Fig. 19C), which is less than that obtained using ZnCo_2O_4 (0.944 V vs. RHE), demonstrating the synergistic effect achieved by increasing the catalytic surface area and efficient electron transfer through the RGO sheet in the composite catalyst.²⁶¹

Employing a similar strategy, Yan and coworkers²⁵⁵ reported the preparation of a 3D bifunctional oxygen electrocatalyst based on $\text{Co/ZnCo}_2\text{O}_4$ nanoparticles derived from CoZn-ZIF-L sandwiched in leaf-like nitrogen-doped carbon microplates interwoven with carbon nanotubes ($\text{Co/ZnCo}_2\text{O}_4@\text{NC-CNTs}$, Fig. 20A), as confirmed by the SEM images in Fig. 20B and C and TEM images in Fig. 20D and E. As shown in Table 7, the $\text{Co/ZnCo}_2\text{O}_4@\text{NC-CNT}$ material is among the best bifunctional electrocatalysts as revealed by its excellent onset potential of 1.01 V, $E_{1/2}$ of 0.90 V, Tafel slope of 91 mV dec⁻¹, limiting current density of 4.6 mA cm⁻² for the ORR and small ΔE of 0.70 V for ORR/OER activities. The excellent activity of this composite is due to the large amount of metal–N_x and Co³⁺ active sites as well as the interwoven CNTs on the surfaces of the carbon microplates which are beneficial to the charge transfer in the ORR/OER processes.²⁵⁵

4.2. Water-splitting electrocatalysts for energy conversion (OER and HER)

Electrochemical water-splitting has been considered as a promising method to obtain H₂ and O₂ through the hydrogen evolution reaction (HER) and the oxygen evolution reaction (OER), respectively. However, the production of H₂ is limited by the sluggish OER kinetics at the anode due to the multi-electron transfer coupled with protons, which leads to high overpotentials.²⁶⁴ Benchmark catalysts such as RuO₂ and IrO₂ have been used in the water-splitting process to overcome this issue. Nevertheless, due to the scarcity and high cost of these noble metals, their commercial implementation has been unfeasible.²⁶⁵ In this sense, it is necessary to search for new electrode materials with low cost, which are not scarce, besides they have a superior electrochemical behavior.

In recent years, cobaltite spinel oxides $\text{M}_x\text{Co}_{3-x}\text{O}_4$ (where M = Ni, Mn, Zn, and Fe) have been used as electrode materials for efficient water oxidation.^{61,266,267} Among these electrode

Table 7 Catalytic activity parameters of recently reported ORR ZnCo_2O_4 -based electrocatalysts

ORR catalysts	Incorporated material or atom	Substrate	E_{ORR} onset potential (V vs. RHE)	Half wave potential (V vs. RHE)	Overpotential E_{ORR} at -3 mA cm ⁻² (V vs. RHE)	Overpotential E_{ORR} at -3 mA cm ⁻¹ (V vs. RHE)	E_{ORR} at 10 mA cm ⁻² (V vs. RHE)	E_{ORR} at 10 mA cm ⁻¹ (V vs. RHE)	Current density (mA cm^{-2})	$\Delta E, E_{\text{ORR}}$ (V vs. RHE)	Tafel slope (mV dec ⁻¹)	Average electron transfer number (n)	Retention% stability (h)	pH conditions for the ORR	Ref.
ZnCo_2O_4 ultrathin nanosheets	—	GCE	—	—	0.34	—	—	—	—	4.1	12	0.1 M KOH	130		
Flower like ZnCo_2O_4	—	GCE	0.81	0.75	0.696	0.41	0.944	—	—	3.05-3.4	—	1 M KOH	261		
Near-spherical particles of ZnCo_2O_4	—	GCE	0.83 ^b	0.62 ^b	—	—	—	2.97	—	3.99	—	0.1 M KOH	235		
ZnCo_2O_4 nanosheets	—	GCE	0.8	—	—	—	—	—	5.6	—	3.77-3.95	95%	0.1 M KOH	260	
ZnCo_2O_4 LFs	—	GCE	0.77	0.68	—	—	—	—	—	—	~3.5	~96%	0.1 M KOH	262	
Near-spherical particles of ZnMnCo_4	Mn	GCE	0.94 ^b	0.74 ^b	—	—	—	—	5.22	—	3.99	—	0.1 M KOH	235	
ZnMnCo_4	—	GCE	0.97	0.76	—	0.49	—	—	5.72	—	3.89	2000 cycles	0.1 M KOH	254	
ZnCo_2O_4 -CNTs	CNTs	GCE	1.01	0.90	—	0.37	0.70 ^c	4.6	91	4.0	CVS	87%	0.1 M KOH	255	
$\text{Co/ZnCo}_2\text{O}_4$ @NC-CNTs	NC-CNTs	GCE	—	—	—	—	—	—	—	—	>10	—	—	—	
ZnCo_2O_4 -MC	MC	GCE	—	—	—	—	—	4.24	—	—	—	—	—	—	
ZnCo_2O_4 -graphene	Graphene	GCE	0.95	0.87	0.851	0.30	0.679	4.49	—	—	—	—	—	—	
rGO-ZnCo ₂ O ₄	RGO	GCE	-0.14 ^a	-0.25 ^a	—	—	—	6.11	—	—	3.7-3.95	12	0.1 M KOH	254	
ZnO/ZnCo ₂ O ₄ /C	ZnO + C	GCE	—	—	—	—	—	—	87.39	3.41	95.6%	3.33	0.1 M KOH	261	
ZnO/ZnCo ₂ O ₄ /C@rGO	ZnO + C + rGO	GCE	-0.05 ^a	-0.15 ^a	—	—	—	—	—	46.70	3.95	99.7%	0.1 M KOH	263	

N-doped MWCNTs = nitrogen-doped multi-walled carbon nanotubes, CNTs = carbon nanotubes, 3D-G = three-dimensional graphene, LFs = lilac flowers, N-C = N-doped carbon, pNGr = N-doped porous graphene, dAC = AC-based defective carbon, and MC = graphene and porous carbon. ^a V vs. Ag/AgCl. ^b V vs. SHE. ^c $\Delta E = |E_{\text{p}}| - |E_{1/2}|$.

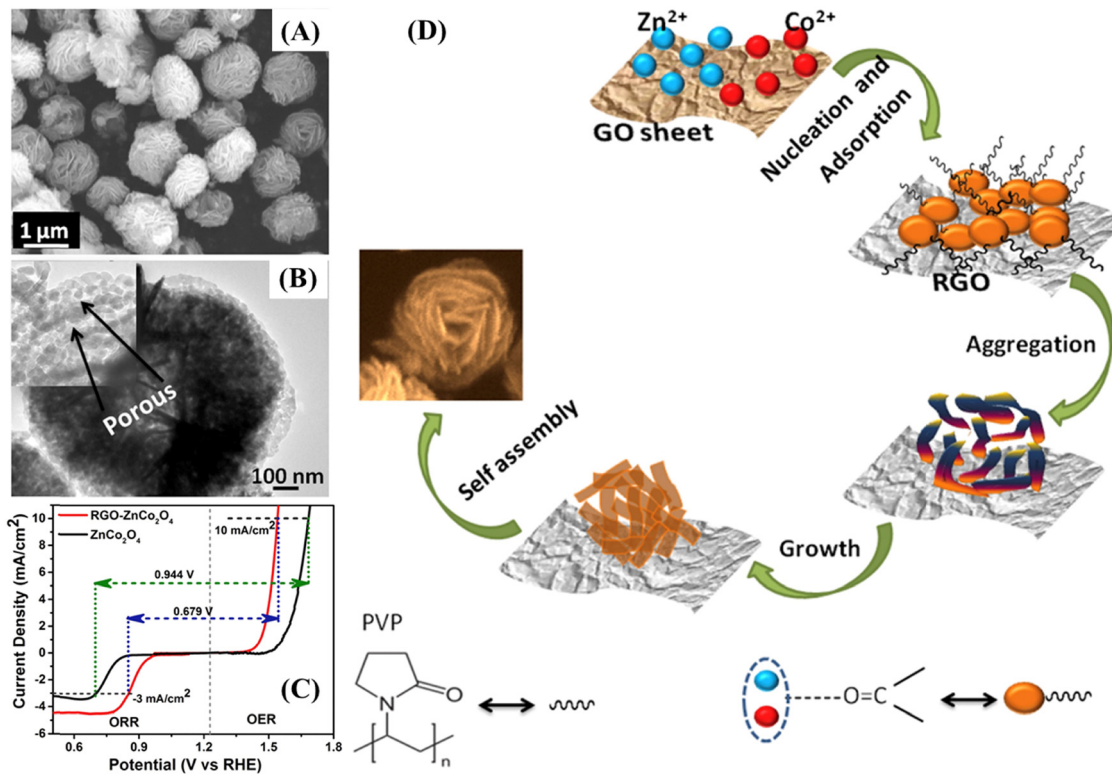


Fig. 19 (A) SEM image of ZnCo₂O₄ microspheres and (B) TEM images of a ZnCo₂O₄ microsphere. The inset of (B) shows the magnified portion of the image that shows the porous structure. (C) Oxygen electrode activities of both the catalysts within the range of potential for the ORR and OER in O₂-saturated 1 M KOH electrolyte at 1200 rpm. (D) Growth mechanism of rGO-ZnCo₂O₄ flower-like microstructures. Reproduced with permission.²⁶¹ Copyright © 2018 Hydrogen Energy Publications LLC. Published by Elsevier Ltd. All rights reserved.

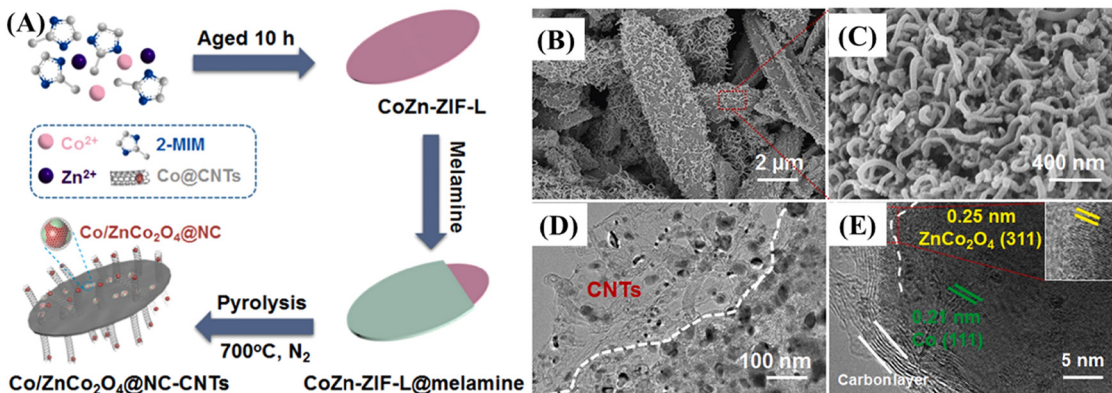


Fig. 20 (A) Schematic synthesis process of the Co/ZnCo₂O₄@NC-CNT electrocatalyst. (B and C) SEM images, (D) TEM image, and (E) HRTEM image of the as-prepared Co/ZnCo₂O₄@NC-CNTs. Reproduced with permission.²⁵⁵ Copyright © 2020 Elsevier Ltd. All rights reserved.

materials, ZnCo₂O₄ has drawn attention due to its rich redox chemistry, which has led to enhanced electrochemical performance. Indeed, ZnCo₂O₄ presents a better catalytic activity for the OER when compared to other cobaltite spinel oxides,²⁶⁸ and the reason for this lies in how Zn²⁺ ions replace Co ions in the Co₃O₄ spinel structure.

In the Co₃O₄ spinel structure, Co²⁺ and Co³⁺ ions are found, respectively, in the tetrahedral and octahedral sites. Kim and colleagues²⁶⁹ demonstrated that Zn²⁺, when inserted into the

Co₃O₄ spinel structure to form ZnCo₂O₄, only replaces Co²⁺ found in the tetrahedral interstices, leaving Co³⁺ (highly active species for the OER) unchanged in the octahedral sites. Nevertheless, other metal ions like Ni and Mn, when inserted into Co₃O₄ to form NiCo₂O₄ and MnCo₂O₄, respectively, can suppress the catalytic activity for the OER,²⁶¹ due to occupation of tetrahedral and octahedral sites in the Co₃O₄ spinel structure. In addition, M. Harada, F. Kotegawa, & M. Kuwa¹⁶ demonstrated that the active sites are controlled by the balance of



M^{3+}/M^{2+} cation distribution in O_h and T_d sites and by the bond strength between M and oxygen atoms at the electrocatalyst surface before and after the exposure to OER conditions, where the catalytic activity of the OER decreases in the order of $ZnCo_2O_4 > NiCo_2O_4 > FeCo_2O_4 > Co_3O_4 > MnCo_2O_4$.

In this sense, $ZnCo_2O_4$ has been used as an electrode material for the OER and has shown good results. For instance, Bao *et al.*¹³⁰ prepared $ZnCo_2O_4$ ultrathin nanosheets by thermal treatment of $ZnCo$ -LDH (where LDH = layered double hydroxide). The electrode material was deposited on a GCE (glassy carbon electrode) and tested for OER performance in KOH 1.0 mol L⁻¹. The as-prepared $ZnCo_2O_4$ ultrathin nanosheet presented an overpotential of 340 mV at 10 mA cm⁻², and a Tafel slope of 38 mV dec⁻¹, compared to RuO_2 (33 mV dec⁻¹). The authors attributed these results to the large surface area of $ZnCo_2O_4$ ultrathin nanosheets that provides more exposed active sites on the surface, easing the catalytic reaction. Moreover, Xiang and colleagues²⁷⁰ synthesized $ZnCo_2O_4$ nanosheets with abundant oxygen vacancies (OV), named OV- $ZnCo_2O_4$, through the hydrothermal method and $NaBH_4$ reduction process. The results showed that the presence of oxygen vacancies in $ZnCo_2O_4$ was beneficial for the OER. In fact, OV- $ZnCo_2O_4$ achieved an overpotential of 324 mV at 10 mA cm⁻², while pristine $ZnCo_2O_4$ showed an overpotential of 427 mV at the same current density. The catalytic kinetics for the OER also was evaluated and OV- $ZnCo_2O_4$ presented a Tafel slope of 56.9 mV dec⁻¹, which is lower than that of pristine $ZnCo_2O_4$ (74.4 mV dec⁻¹).

Although the studies aforementioned seem to be encouraging, the electrochemical performance of $ZnCo_2O_4$ is still

restricted by its poor electronic conductivity, which leads to suppression of electrocatalytic activity towards the OER. Thus, most works reported in the literature presented $ZnCo_2O_4$ combined with other compounds, especially with conductive polymers and conductive carbon-based materials to enhance its electronic conductivity, resulting in a better catalytic activity for the OER, as can be seen in Table 8.

For instance, Tomboc *et al.*²⁷⁴ prepared $ZnCo_2O_4$ nanoparticles with a nanocactus morphology in the presence of polyvinylpyrrolidone (PVP) (here denoted as PVP- $ZnCo_2O_4$) using a one-step hydrothermal method followed by calcination treatment. The authors demonstrated that in the presence of PVP the electrocatalytic activity of $ZnCo_2O_4$ was enhanced when compared to $ZnCo_2O_4$ without PVP. Indeed, PVP- $ZnCo_2O_4$ exhibited an overpotential of 282 mV at 10 mA cm⁻², while $ZnCo_2O_4$ without PVP showed an overpotential of 343 mV. PVP- $ZnCo_2O_4$ also presented an overpotential lower than PVP- $NiCo_2O_4$ (298 mV), synthesized under the same conditions.

Recently, Zhao and colleagues²⁷⁵ electropolymerized poly-pyrrole (PPy) on $ZnCo_2O_4$ nanowires under a constant potential of 0.9 V for 60, 100, 200 and 300 s, and the electrodes were denoted as $ZnCo_2O_4@PPy-60$, $ZnCo_2O_4@PPy-100$, $ZnCo_2O_4@PPy-200$, and $ZnCo_2O_4@PPy-300$, respectively. The SEM image of $ZnCo_2O_4@PPy-200$ in Fig. 21B reveals that nanowires were coated by a thin layer of PPy, in comparison to $ZnCo_2O_4$ (Fig. 21A), and from the TEM images in Fig. 21C and D it is possible to observe that nanowires are composed of many nanoparticles. In addition, $ZnCo_2O_4@PPy-200$ presented a surface area of 56 m² g⁻¹ higher than pristine $ZnCo_2O_4$ (39 m² g⁻¹).

Table 8 $ZnCo_2O_4$ -based OER and HER catalysts and their main electrocatalytic parameters

Catalyst	Preparation method	Overpotential at 10 mA cm ⁻² ($E_{\eta_{10}}$) (mV vs. RHE)	Tafel slope (mV dec ⁻¹)	Stability (h)	pH conditions (mol L ⁻¹)	Ref.
OER	$ZnCo_2O_4$	Sol-gel method	650	51	—	KOH 0.1
	$ZnCo_2O_4$ nanosheets	Thermal treatment of Zn-Co LDH	340	38	—	KOH 1.0
	MOF-derived $ZnCo_2O_4$	Calcination process	389	61.8	2	KOH 1.0
	OV- $ZnCo_2O_4$	Hydrothermal method	324	56.9	30	KOH 0.1
	$m\text{-}ZnCo_2O_4$	Calcination process	300	54	—	KOH 1.0
	PVP- $ZnCo_2O_4$ NPs	Hydrothermal method	282	79.9	24	KOH 1.0
	$ZnCo_2O_4@PPy-200$	Hydrothermal and electrochemical deposition	254	60.77	42	KOH 1.0
	$ZnCo_2O_4$ -CNTs	Hydrothermal method	490	—	—	KOH 0.1
	$ZnCo_2O_4@C\text{-}MWCNTs$	Calcination process	327	65	25	KOH 1.0
	$ZnCo_2O_4@NC/CT$	Carbonization–oxidation process	196.4	61.3	45	KOH 1.0
	rGO- $ZnCo_2O_4$	Solvothermal method	300	59.2	12	KOH 1.0
	$Co/ZnCo_2O_4@NC\text{-}CNTs$	Pyrolysis treatment	370	64	30	KOH 1.0
	$ZnCo_2O_4@Ni(OH)_2\text{-}2.0$	Hydrothermal method	280.2 ^a	64.62	17	KOH 1.0
	$ZnCo_2O_4@ZnCo$ -LDHs	Hydrolysis	375	73	—	KOH 1.0
	$ZnCo_2O_4@NiFe$ -LDH	Hydrothermal method	249	96.7	20	KOH 1.0
	$ZnCo_2O_4/FeOOH$ HPs	Thermal treatment of ZnCo/ZIFs	299	69	15	KOH 1.0
	$ZnCo_2O_4/Au/CNTs$	Hydrothermal method	440	46.2	—	KOH 1.0
HER	$ZnCo_2O_4/Co_3Se_2$	Solvothermal method	324	79.3	50	KOH 1.0
	$C/ZnCo_2O_4/ZnO$	Annealing	279	72	24	KOH 1.0
	$Co_2P/CoO/ZnCo_2O_4$	Hydrothermal followed by phosphorization process	112	62	24	KOH 1.0
	$ZnCo_2O_4@PPy-50$	Hydrothermal and electrochemical deposition	133	62.4	—	KOH 1.0
	$ZnCo_2O_4@PPy-200$	Hydrothermal and electrochemical deposition	183.52	60.77	22	KOH 1.0

HPs = hollow polyhedrons; ZIFs = zeolitic imidazolate frameworks. ^a At 50 mA cm⁻².



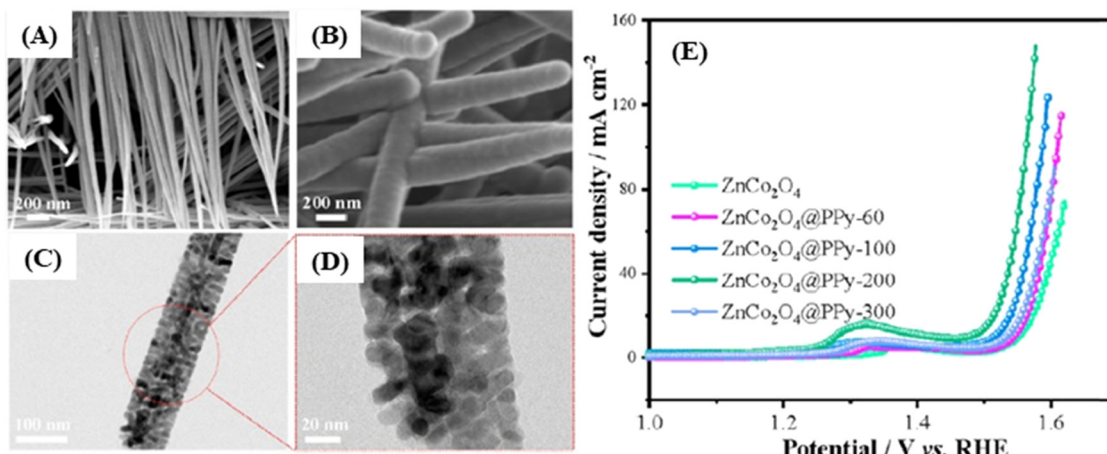


Fig. 21 SEM images of ZnCo_2O_4 (A) and ZnCo_2O_4 @PPy-200 (B). TEM images of ZnCo_2O_4 @PPy-200 (C and D). Linear sweep voltammetry at 2 mV s^{-1} for ZnCo_2O_4 and ZnCo_2O_4 @PPy samples (E). Reproduced with permission.²⁷⁵ Copyright © 2021 Elsevier Ltd. All rights reserved.

Among these samples, ZnCo_2O_4 @PPy-200 exhibited a lower overpotential (250 mV) at 10 mA cm^{-2} (Fig. 21E) and a lower Tafel slope ($60.77 \text{ mV dec}^{-1}$). Chronoamperometric studies were performed to evaluate the durability and stability of the ZnCo_2O_4 @PPy-200 electrode, and even after 42 hours the catalyst remained steady, revealing its excellent stability.

In addition to conductive polymers, carbon-based materials (carbon nanotubes and graphene) have been widely used with cobaltite spinel oxides to improve their electronic conductivity,^{284,285} thus providing a conducting platform. Furthermore, these materials, when combined, present a synergistic effect in the OER owing to their high surface area, providing more electrocatalytically active sites for charge transport between the electrode/electrolyte interface. For instance, Yan and co-authors²⁵⁵ reported the synthesis of $\text{Co}/\text{ZnCo}_2\text{O}_4$ from a MOF (CoZn-ZIF-L) sandwiched in N-doped carbon interconnected with carbon nanotubes (denoted $\text{Co}/\text{ZnCo}_2\text{O}_4$ @NC-CNTs) as an electrode material for OER activity. The composite presented an overpotential of 370 mV at a current density of 10 mA cm^{-2} and a low Tafel slope of 64 mV dec^{-1} . Similarly, Liu *et al.*²⁷⁶ embedded two different MOFs (metal-organic frameworks) ZIF-8 and ZIF-67 into MWCNTs (multi-walled carbon nanotubes) and obtained ZnCo_2O_4 @C-MWCNTs by the calcination process. The electrode material exhibited a low overpotential of 327 mV at 10 mA cm^{-2} and a Tafel slope of 65 mV dec^{-1} . In addition, the electrocatalytic activity of ZnCo_2O_4 @C-MWCNTs remained unchanged, even after 25 hours of tests, demonstrating the reliability of the material.

In the same way, Kong *et al.*,¹³⁸ using a ZnCo MOF, prepared an electrode material based on zinc-cobalt oxide nanoflakes@N-doped carbon hollow nanowall arrays anchored onto carbon textile (ZnCo_2O_4 @NC/CT). The SEM images of ZnCo_2O_4 @NC/CT show that the compound grown vertically on a carbon textile electrode (Fig. 22A) and holes can be observed in its structure (Fig. 22B), caused by cation exchange between Co^{2+} and Zn^{2+} . Furthermore, the hollow structure is confirmed through the contrast between the shell and core (hollow), as can be seen in

Fig. 22C. The electrode exhibited an outstanding low overpotential of 196.4 mV at 10 mA cm^{-2} , a low Tafel slope of 61.3 mV dec^{-1} , and a long-term durability of 45 hours (Fig. 22D). The authors attributed the excellent results to (i) the decreased resistance at the interface between the substrate and the electrode material due to the direct growth of N-doped carbon nanowalls on the substrate surface, leading to improvement of the ion/electron transfer rates and (ii) the easy penetration of electrolyte, leading to faster faradaic reactions and ion diffusion rates, thanks to the high surface area of the porous structure of the ZnCo_2O_4 nanoflake shell, as shown in Fig. 22E and F.

Graphene has also been combined with spinel oxides to improve the electrocatalytic activity for the OER.^{284,286,287} To enhance the catalytic activity of ZnCo_2O_4 towards the OER, Chakabarty *et al.*²⁶¹ prepared a ZnCo_2O_4 grafted onto reduced graphene oxide (rGO) sheet through the solvothermal method. The SEM and TEM images in Fig. 19A and B revealed that the structure of the ZnCo_2O_4 microsphere is highly porous, as well as composed of several nanoparticles with an average size of 10 nm. The highly porous structure of ZnCo_2O_4 was maintained in the rGO-ZnCo₂O₄, as shown in Fig. 19B. The rGO-ZnCo₂O₄ composite presented the lowest overpotential at 10 mA cm^{-2} for the OER (300 mV) when compared to rGO (510 mV), ZnCo_2O_4 (410 mV), and benchmark IrO_2 (340 mV), or a rGO/ZnCo-layered double hydroxide composite (onset overpotential $\sim 330 \text{ mV}$).²⁸⁸ Moreover, rGO-ZnCo₂O₄ presented high stability and the current density remained stable from the beginning to the end of the measurement (12 h), differently from ZnCo_2O_4 that presented a decrease of current density, caused by gas bubble formation. In addition, the electrocatalytic activity of rGO-ZnCo₂O₄ towards the OER was evaluated by SECM measurement. It is possible to observe that a small current density is detected from 1.4 V, indicating the beginning of the OER process. As the potential increases to 1.45 V and 1.5 V the current density also increases.

In addition to carbon-based materials, other compounds such as LDH and oxides have been associated with ZnCo_2O_4 , as

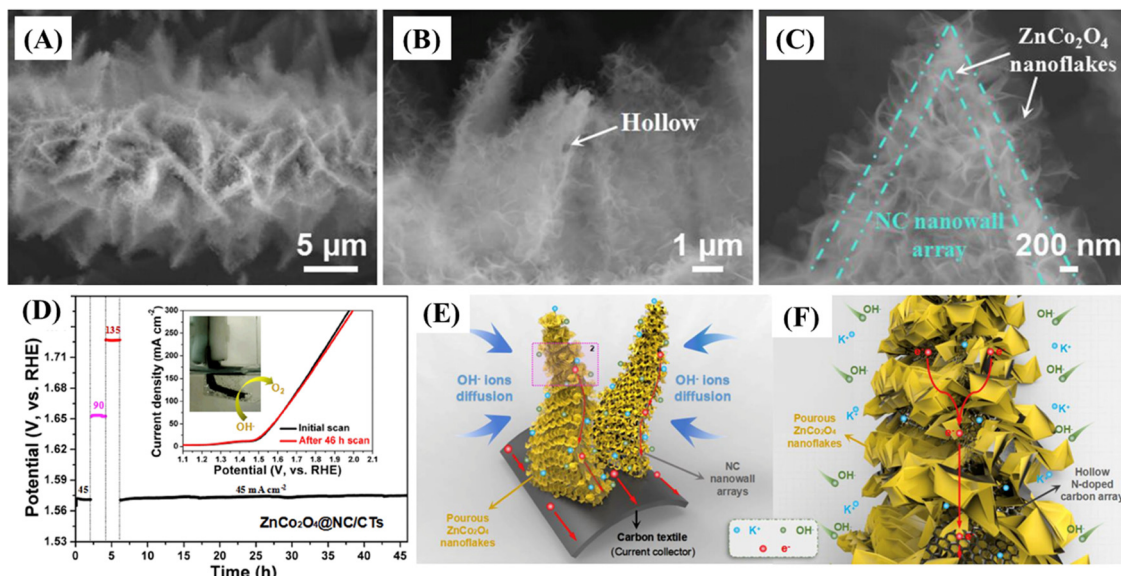


Fig. 22 (A–C) SEM images of ZnCo_2O_4 @NC/CT. (D) Stability measurements of ZnCo_2O_4 @NC/CT at different current densities and (E and F) schematic illustration of the ZnCo_2O_4 @NC/CT electrode. Reproduced with permission.¹³⁸ Copyright © 2019 Published by Elsevier B.V.

can be seen in Table 8. For instance, Pan *et al.*²⁷⁸ reported the synthesis of ZnCo_2O_4 @ZnCo-LDH yolk-shell nanospheres. The electrode material exhibited an overpotential of 375 mV at 10 mA cm^{-2} and a Tafel slope of 73 mV dec⁻¹. Its electrochemical performance was attributed to the large surface area, the synergistic effect between ZnCo_2O_4 and ZnCo-LDH, and the interconnection among the nanosheets which consisted of the nanospheres, causing the reduction of the transportation path of electrolyte ions. Que *et al.*²⁷⁹ obtained a core-shell structure of ZnCo_2O_4 @NiFe-LHD that presented an overpotential of 249 mV at 10 mA cm^{-2} . The authors explained that the low overpotential achieved by the electrode material was due to the synergistic effect between core@shell structure components. Xiong *et al.*²⁸² prepared a C/ ZnCo_2O_4 /ZnO material, combining two strategies (preparation of MOF-derived ZnCo_2O_4 and the formation of a hierarchical core@shell structure). As a consequence, the electrode material required 279 mV overpotential to reach 10 mA cm^{-2} current density. Besides, the electrocatalyst did not present significant degradation after a 24 h stability test.

Possible strategies and tendencies in the preparation of electrode materials based on ZnCo_2O_4 for OER catalysis can be seen in Fig. 23, where the electrocatalysts are summarized according to their low overpotential ($\eta_{10} \leq 300 \text{ mV}$). Analyzing the electrode materials displayed in Fig. 23 we figured out that three of the nine electrocatalysts based on ZnCo_2O_4 are MOF derivatives, and one of them presented the best electrochemical performance for OER catalysis among the electrocatalysts reported. In fact, ZnCo_2O_4 @NC/CT, C/ ZnCo_2O_4 /ZnO and ZnCo_2O_4 /FeOOH HPs exhibited an overpotential of 196.4, 279 and 299 mV, respectively. The best electrocatalyst ZnCo_2O_4 @NC/CT presented an overpotential of $\sim 102 \text{ mV}$ lower than the seventh electrocatalyst also based on MOF-derivative ZnCo_2O_4 /FeOOH HPs (299 mV). Although both of them were designed

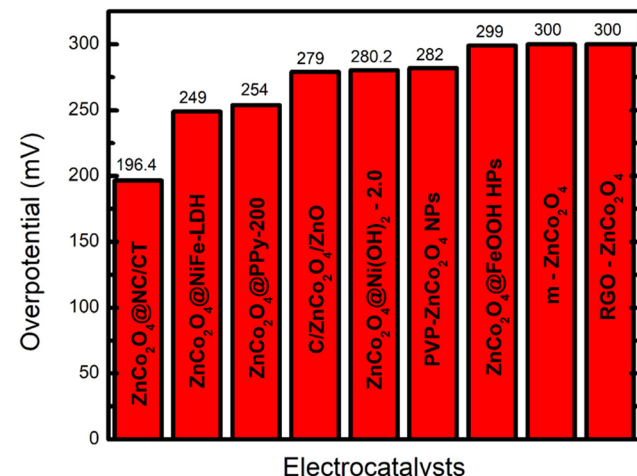


Fig. 23 The top 9 electrocatalysts based on ZnCo_2O_4 for the OER that presented an overpotential $\leq 300 \text{ mV}$ ($\eta_{10} \leq 300 \text{ mV}$).

from the MOF, the former was combined with a carbon material that enhanced the electronic conductivity of the electrode. However, the rGO- ZnCo_2O_4 electrocatalyst occupied the eighth position along with m- ZnCo_2O_4 and both of them presented an overpotential of 300 mV.

Among the electrode materials displayed in Fig. 23, it can be noticed that the combination of ZnCo_2O_4 with conductivity polymers can also be a good strategy to improve the electrochemical performance of the electrocatalyst. Indeed, intermediate overpotential values were reached for ZnCo_2O_4 @PPy-200 (254 mV) and PVP- ZnCo_2O_4 NPs (282 mV) electrodes, occupying, respectively, the third and sixth positions.

The design of hierarchical structures as core@shell providing a shortened ion/electron transport pathways and a large surface area with a large number of electrocatalytic sites exposed, favoring

faradaic reactions, seems to be another interesting strategy to improve the electrochemical performance for OER catalysis. Thus, it can be highlighted that the electrocatalyst based on ZnCo_2O_4 @NiFe-LDH presented the second-best electrochemical performance with an overpotential of 249 mV, and the synergistic effect between the core and shell materials in the structure contributed to the excellent result. It is noteworthy that the chosen shell material also was fundamental to achieving the results. In fact, recent studies have shown that NiFe-LDH and ternary NiFe-LDH derivatives are promising electrode materials for the OER catalysis.²⁸⁹ The fifth position was occupied by the electrocatalyst ZnCo_2O_4 @ $\text{Ni}(\text{OH})_2$ - 2.0, presenting an overpotential of 280.2 mV, where the presence of $\text{Ni}(\text{OH})_2$ as a shell material improved the electrochemical performance of the electrode materials, since the $\text{Ni}(\text{OH})_2$ nanosheets made transporting electrons/ions easier. In fact, the overpotential value for the ZnCo_2O_4 @ $\text{Ni}(\text{OH})_2$ is much smaller than those of many other pristine materials such as NiO (310 mV),²⁹⁰ ZnO (340 mV)²⁹¹ and $\text{Ni}(\text{OH})_2$ (340 mV).²⁹²

Although many works using ZnCo_2O_4 as an electrode material for the catalysis of OER processes have been reported, few articles using the same material were found in the literature for HER electrocatalysis, as can be seen in Table 8. The main reason for this is that the production of high-purity hydrogen from the water-splitting method²⁹³ still is restricted by the sluggish kinetics of the OER.²⁶⁴

Among these works, we can highlight that reported by Zhang and colleagues²⁸³ where zinc cobalt oxide/phosphide ($\text{Co}_2\text{P}/\text{CoO}/\text{ZnCo}_2\text{O}_4$) hollow submicron boxes were obtained and used as an electrode material for the HER. The electrocatalyst showed an overpotential of 112 mV at -10 mA cm^{-2} current density; for comparison purposes the commercial Pt/C electrode also was tested and presented an overpotential of 19 mV at the same current density. Furthermore, the electrode materials exhibited a Tafel slope of 62 mV dec^{-1} , indicating that the reaction pathway obeys the Volmer–Heyrovsky mechanism with a fast Volmer step for the HER.

5. Conclusion and outlook

The morphology of ZnCo_2O_4 has a huge impact on its electrochemical performance, and can be improved by means of a rational design. The specific capacitance, electrocatalytic activity, rate-capability and cycling stability of ZnCo_2O_4 -based electrodes heavily depend on ZnCo_2O_4 mechanical properties. Bulkier micro- and nanoparticles usually have low specific surface area (even lower if they are not porous or having at least rough surfaces), heavily suffering from the strain effects throughout the charge–discharge cycling, and high internal electrical resistance due to low surface area-to-volume ratios.

The design of 1D and 2D morphologies, along with hollow and/or porous structures, can partially overcome these limitations, specially aligned with suitable spaces between these 1D and 2D structures. 1D and 2D structures present increased specific surface areas, promoting electrolyte diffusion and electroactive site availability; greatly reduced one or more

dimensions, providing shortened electron transfer pathways and alleviating the strain effects caused by volume changes; and in the case of electrocatalysts the high porosity and pore sizes, enhancing specific surface area and facilitating electrolyte adsorption and product release (e.g., O_2 in the OER and H_2 in the HER).

In fact, for supercapacitive applications, 1D structures can deliver high specific capacitances at lower current densities, owing to their unidimensional electron pathways and high specific surface area, which enhances the electroactive site availability. However, usually at higher current densities the electrolyte diffusion is hindered due to the entanglement of such 1D structures, which reduces the area for electrolyte penetration within the structure, limiting the electroactive site availability and cyclability. This effect can also be observed in 2D structures, which, even being the most commonly synthesized and being known for their high specific capacitance, can present strain effects caused by volume changes if the space between the structures is not suitable for fast electrolyte diffusion at higher current densities. Thus, it is extremely beneficial to engineering electrodes based on ZnCo_2O_4 with wide-open 1D or 2D nanostructures, which, along with all the benefits of such structures, facilitates the electrolyte diffusion even at higher current densities and further alleviates the strain effects of continuous charge–discharge cycling processes.

As for electrocatalytic applications, similarly to supercapacitive applications, it is interesting to synthesize wide-open and porous nanostructures. 1D nanostructures usually present unsuitable specific surface area, pore sizes and porosity for efficient electrolyte adsorption and product desorption, hindering the electrocatalyst performance of such structures, especially in comparison to 2D structured nanoparticles. 2D nanostructures commonly present the most optimal mesoporous and microporous sizes and volumes for the promotion of electrocatalytic activity, which can be even further enhanced according to the spaces between such structures by the facilitation of electrolyte penetration and enhancement of electroactive site availability.

Additionally, the electrochemical performance of ZnCo_2O_4 -based electrodes can be even more improved by the incorporation of composites and/or binder-free electrode production, along with the morphology control. The use of slurry-cast electrodes with binders that can significantly reduce the electronic conductivity, limiting the availability of active materials, and hindering the ion-diffusion. It can also increase the mass density as “dead-mass” and reduce the material integrity through cycling. So, binder-free electrodes should be preferred to circumvent all the above-mentioned downsides. ZnCo_2O_4 composites can be produced with highly electrically conductive and/or electrochemically active carbonaceous and other transition metal materials, such as oxides, hydroxides and sulfides, as both support and coating components. They can provide bigger specific surface area, faster electron transfer, and short and more efficient ion-diffusion paths. In addition to the more active sites and richer redox reactions, the overall stability is greatly improved. One can also morphologically orient the growth of ZnCo_2O_4 when it is used as a support material.



The strategies for synthesis and application of pristine ZnCo_2O_4 and its composites in LIBs, SIBs, Li-S batteries and metal-air batteries are summed up. Although ZnCo_2O_4 has been applied in energy storage and has proved to be a promising electrode material, there are a few challenges to mention, *e.g.*, its poor electrical conductivity, slow lithium diffusion and short cycling life. This is associated with the volume expansion during the lithium insertion and extraction process. Many prospective strategies should be developed for the application of ZnCo_2O_4 electrode materials, and we hope that this review article will facilitate further studies and advancements in this area.

Improving the conductivity is always a key issue in the development of electrode materials based on ZnCo_2O_4 . Generally synthesis of electrode materials with nanoscale dimension ZnCo_2O_4 has already been proven to be effective for obtaining high-power density, high-energy density, better stability and other admirable electrochemical performances. Nanostructured ZnCo_2O_4 composites with conductive materials such as polymers and carbon were also demonstrated to improve their electrochemical performance. These strategies can effectively enhance the conductivity and alleviate the volume change of ZnCo_2O_4 electrode materials. Therefore, ZnCo_2O_4 has been gaining more and more attention in the field of energy storage in recent years.

For application as electrocatalysts in energy technologies, ZnCo_2O_4 and its composites show great potential due to their high intrinsic activity. In many cases they can exhibit bifunctionalities, encompassing both ORR and OER activity. In fact, it is important to highlight that the main strategies employed in electrode materials for the ORR consisted of the design of new catalysts with different morphologies, and the formation of composites with conducting nanocarbons, such as carbon nanotubes and graphene.

Similarly, although ZnCo_2O_4 exhibits an overpotential close to 300 mV as an electrode material for OER catalysis, it is limited by its poor conductivity. For this reason, ZnCo_2O_4 -based OER electrocatalysts have been combined with conducting carbon materials and polymers, as well as with compounds such as metal oxides/hydroxides. Curiously, among the top 9 ($\eta_{10} \leq 300$ mV) electrode materials for OER catalysis, three electrocatalysts are based on MOF-derivatives. Deriving ZnCo_2O_4 electrodes using the MOF strategies can be interesting, since the main features will be preserved, such as a high porous structure and large surface area.²⁹⁴ They will improve the electrochemical performance of the electrocatalyst. The design of the electrode material is fundamental for obtaining a good electrochemical performance. For instance, hierarchical core@shell structures can yield excellent results because of their large surface area, while the exposed electrocatalytic sites can improve the faradaic reaction, and shorten the ion/electron transport pathway. In fact, the regulation strategies for improving the electrocatalytic performance of ZnCo_2O_4 -based electrodes follow trends also reported in other works^{6,289,295} and can be summarized mainly as: (a) reducing electrical resistance using conductive supports and (b) increasing active sites by

nanostructuration, morphology engineering and porous structure construction.²⁷

Despite the important advances in the design of new materials based on ZnCo_2O_4 aforementioned, many challenges still need to be overcome regarding a full exploration and implementation in practical/real application in electrochemical energy storage and conversion. For instance, currently it is mandatory the development of devices that are able to withstand high current density with long-term cycling stability, aiming to reduce the charge time, *e.g.*, devices that can provide high energy density at a high-power density during the long-term charge/discharge cycling process. However, the excellent performances generally reported in the literature, especially in studies using three-electrode systems, and even in two-electrode devices, may not fully represent a real application, since on a laboratory scale it usually takes 2–3 mg cm^{−2} of the electrode material, but commercially always demands high mass loading (>10 mg cm^{−2}). In this sense, the design and manufacture of more robust devices with greater thickness and mass loading should be further studied.

In fact, we are convinced that much research needs to be done to further improve electrochemical and electrocatalytic materials based on ZnCo_2O_4 , where site engineering and a conductivity optimization approach should be used in the quest for ideal electrode materials.²⁷ For instance, the incorporation (or metal-ion doping) of third and fourth metal ions³ or the development of high entropy materials²⁹⁶ can be decisive for improving energy storage and for electrocatalytic activity.²⁸⁹ In fact, these strategies can also help in the challenge of minimizing the use of Co, which are pushing a new trend of emerging low-Co (and Co-free) materials as next-generation electrode materials for energy applications.²⁹⁷ In addition, the research should seek to increase the conductivity and porosity of ZnCo_2O_4 /carbon composites as strategies for manufacturing electrodes with high mass loading for real application. From this perspective, the preparation of ZnCo_2O_4 /carbon derived from MOFs should be studied more deeply, especially those derived from the zeolitic imidazolate framework (ZIF-67, ZIF-8, ZIF-67 + ZIF-8, *etc.*). In fact, MOF-derived composites have been regarded as excellent new functional electrode materials for many applications, exhibiting exceptional conductivity, stability, porous/hollow structures with tunable shapes, and tailored compositions and electrochemical activity, overcoming the relatively low conductivity and missing chemical and/or structural robustness of precursor MOFs.^{13,294,298} Therefore, these are some future directions for the development of ZnCo_2O_4 based materials for their commercial/real applications towards a more sustainable society.

Conflicts of interest

There are no conflicts to declare.

Acknowledgements

This work was supported by the São Paulo Research Foundation (FAPESP 2018/21489-1, 2017/13137-5, 2014/50867-3 and



2013/24725-4) and the National Council for Scientific and Technological Development (CNPq 401581/2016-0, 408222/2016-6, 442599/2019-6, 311847/2018-8), in addition to the fellowships granted to J. M. G. (FAPESP 2018/16896-7), M. I. S. (CAPES 141853/2015-8) and M. N. T. S. (CAPES 88882.429165/2019.01). The Grupo de Materiais Inorgânicos do Triângulo (GMT) research group was supported by FAPEMIG (APQ-00330-14), Brazilian Institute of Science and Technology (INCT) in Carbon Nanomaterials.

References

- 1 S. Liu, L. Hu, X. Xu, A. A. Al-Ghamdi and X. Fang, Nickel Cobaltite Nanostructures for Photoelectric and Catalytic Applications, *Small*, 2015, **11**, 4267–4283.
- 2 J. M. Gonçalves, A. Kumar, M. I. da Silva, H. E. Toma, P. R. Martins, K. Araki, M. Bertotti and L. Angnes, Nanoporous Gold-Based Materials for Electrochemical Energy Storage and Conversion, *Energy Technol.*, 2021, **9**, 2000927.
- 3 J. M. Gonçalves, M. I. da Silva, H. E. Toma, L. Angnes, P. R. Martins and K. Araki, Trimetallic oxides/hydroxides as hybrid supercapacitor electrode materials: a review, *J. Mater. Chem. A*, 2020, **8**, 10534–10570.
- 4 S. J. Uke, V. P. Akhare, D. R. Bambole, A. B. Bodade and G. N. Chaudhari, Recent Advancements in the Cobalt Oxides, Manganese Oxides, and Their Composite As an Electrode Material for Supercapacitor: A Review, *Front. Mater.*, 2017, **4**, 21.
- 5 J. G. Ruiz-Montoya, V. L. Quispe-Garrido, J. C. Calderón Gómez, A. M. Baena Moncada and J. M. Gonçalves, Recent Progress and Prospects on Supercapacitor Materials based on Metal Oxide or Hydroxide/Biomass-Derived Carbon Composites, *Sustainable Energy Fuels*, 2021, **5**, 5332–5365.
- 6 J. M. Gonçalves, D. P. Rocha, M. N. T. Silva, P. Roberto Martins, E. Nossol, L. Angnes, C. S. Rout and R. A. Abarza Munoz, Feasible strategies to promote the sensing performances of spinel MCo_2O_4 ($M = Ni, Fe, Mn, Cu$ and Zn) based electrochemical sensors: A review, *J. Mater. Chem. C*, 2021, **9**, 7852–7887.
- 7 Y. Li, X. Han, T. Yi, Y. He and X. Li, Review and prospect of $NiCo_2O_4$ -based composite materials for supercapacitor electrodes, *J. Energy Chem.*, 2019, **31**, 54–78.
- 8 J. M. Gonçalves, M. N. T. Silva, K. K. Naik, P. R. Martins, D. P. Rocha, E. Nossol, R. A. A. Munoz, L. Angnes and C. S. Rout, Multifunctional spinel $MnCo_2O_4$ based materials for energy storage and conversion: a review on emerging trends, recent developments and future perspectives, *J. Mater. Chem. A*, 2021, **9**, 3095–3124.
- 9 X. Zhao, L. Mao, Q. Cheng, J. Li, F. Liao, G. Yang, L. Xie, C. Zhao and L. Chen, Two-dimensional Spinel Structured Co-based Materials for High Performance Supercapacitors: A Critical Review, *Chem. Eng. J.*, 2020, **387**, 124081.
- 10 J. P. Cheng, W. D. Wang, X. C. Wang and F. Liu, Recent research of core-shell structured composites with $NiCo_2O_4$ as scaffolds for electrochemical capacitors, *Chem. Eng. J.*, 2020, **393**, 124747.
- 11 X. Han, X. Gui, T.-F. Yi, Y. Li and C. Yue, Recent progress of $NiCo_2O_4$ -based anodes for high-performance lithium-ion batteries, *Curr. Opin. Solid State Mater. Sci.*, 2018, **22**, 109–126.
- 12 R. Kumar, $NiCo_2O_4$ Nano-/Microstructures as High-Performance Biosensors: A Review, *Nano-Micro Lett.*, 2020, **12**, 122.
- 13 R. Wu, J. Sun, C. Xu and H. Chen, $MgCo_2O_4$ -based electrode materials for electrochemical energy storage and conversion: a comprehensive review, *Sustainable Energy Fuels*, 2021, **5**, 4807–4829.
- 14 J. Sun, C. Xu and H. Chen, A review on the synthesis of $CuCo_2O_4$ -based electrode materials and their applications in supercapacitors, *J. Materomics*, 2021, **7**, 98–126.
- 15 H. Gao, S. Liu, Y. Li, E. Conte and Y. Cao, A Critical Review of Spinel Structured Iron Cobalt Oxides Based Materials for Electrochemical Energy Storage and Conversion, *Energies*, 2017, **10**(11), 1787, DOI: [10.3390/en10111787](https://doi.org/10.3390/en10111787).
- 16 M. Harada, F. Kotegawa and M. Kuwa, Structural Changes of Spinel MCo_2O_4 ($M = Mn, Fe, Co, Ni$, and Zn) Electrocatalysts during the Oxygen Evolution Reaction Investigated by In Situ X-ray Absorption Spectroscopy, *ACS Appl. Energy Mater.*, 2022, **5**, 278–294.
- 17 S. Gedi, R. Manne, G. Manjula, L. V. Reddy, C. P. Reddy, N. Marraiki, W. K. Kim, K. Mallikarjuna and M. S. Pratap, Reddy, Tunability of the self-assemblies of porous polygon-like zinc cobaltite architectures using mixed solvents for high-performance supercapacitors, *J. Phys. Chem. Solids*, 2022, **163**, 110587.
- 18 J. A. Rajesh and K.-S. Ahn, Facile Hydrothermal Synthesis and Supercapacitor Performance of Mesoporous Necklace-Type $ZnCo_2O_4$ Nanowires, *Catalysts*, 2021, **11**(12), 1516, DOI: [10.3390/catal11121516](https://doi.org/10.3390/catal11121516).
- 19 S.-H. Lee, J. H. Kim and J.-R. Yoon, Laser Scribed Graphene Cathode for Next Generation of High Performance Hybrid Supercapacitors, *Sci. Rep.*, 2018, **8**, 8179.
- 20 N.-T. Suen, S.-F. Hung, Q. Quan, N. Zhang, Y.-J. Xu and H. M. Chen, Electrocatalysis for the oxygen evolution reaction: recent development and future perspectives, *Chem. Soc. Rev.*, 2017, **46**, 337–365.
- 21 M. Bohra, V. Alman and R. Arras, Nanostructured $ZnFe_2O_4$: An Exotic Energy Material, *Nanomaterials*, 2021, **11**(5), 1286, DOI: [10.3390/nano11051286](https://doi.org/10.3390/nano11051286).
- 22 L. Sun, Q. Luo, Z. Dai and F. Ma, Material libraries for electrocatalytic overall water splitting, *Coord. Chem. Rev.*, 2021, **444**, 214049.
- 23 J. M. Gonçalves, P. R. Martins, K. Araki and L. Angnes, Recent progress in water splitting and hybrid supercapacitors based on nickel-vanadium layered double hydroxides, *J. Energy Chem.*, 2021, **57**, 496–515.
- 24 Y. Wang, X. Huang and Z. Wei, Recent developments in the use of single-atom catalysts for water splitting, *Chin. J. Catal.*, 2021, **42**, 1269–1286.
- 25 P. Chen, J. Ye, H. Wang, L. Ouyang and M. Zhu, Recent progress of transition metal carbides/nitrides for electrocatalytic water splitting, *J. Alloys Compd.*, 2021, **883**, 160833.



26 Y. Yan, T. He, B. Zhao, K. Qi, H. Liu and B. Y. Xia, Metal-covalent-organic frameworks-based electrocatalysts for water splitting, *J. Mater. Chem. A*, 2018, **6**, 15905–15926.

27 J. M. Gonçalves, T. A. Matias, K. C. F. Toledo and K. Araki, in *Advances in Inorganic Chemistry*, ed. R. V. Eldik and C. Hubbard, Elsevier, 2019, vol. 74, p. 63.

28 M. Tahir, L. Pan, F. Idrees, X. Zhang, L. Wang, J.-J. Zou and Z. L. Wang, Electrocatalytic oxygen evolution reaction for energy conversion and storage: A comprehensive review, *Nano Energy*, 2017, **37**, 136–157.

29 A. Chakraborty, S. Kunnikuruvan, S. Kumar, B. Markovsky, D. Aurbach, M. Dixit and D. T. Major, Layered Cathode Materials for Lithium-Ion Batteries: Review of Computational Studies on $\text{LiNi}_{1-x-y}\text{Co}_x\text{Mn}_y\text{O}_2$ and $\text{LiNi}_{1-x-y}\text{Co}_x\text{Al}_y\text{O}_2$, *Chem. Mater.*, 2020, **32**, 915–952.

30 M. Winter and R. J. Brodd, What Are Batteries, Fuel Cells, and Supercapacitors?, *Chem. Rev.*, 2004, **104**, 4245–4270.

31 C. Zou, L. Zhang, X. Hu, Z. Wang, T. Wik and M. Pecht, A review of fractional-order techniques applied to lithium-ion batteries, lead-acid batteries, and supercapacitors, *J. Power Sources*, 2018, **390**, 286–296.

32 Y. Gogotsi and R. M. Penner, Energy Storage in Nanomaterials – Capacitive, Pseudocapacitive, or Battery-like?, *ACS Nano*, 2018, **12**, 2081–2083.

33 J. Cherusseri, D. Pandey and J. Thomas, Symmetric, Asymmetric, and Battery-Type Supercapacitors Using Two-Dimensional Nanomaterials and Composites, *Batteries Supercaps*, 2020, **3**, 860–875.

34 N. R. Chodankar, H. D. Pham, A. K. Nanjundan, J. F. S. Fernando, K. Jayaramulu, D. Golberg, Y.-K. Han and D. P. Dubal, True Meaning of Pseudocapacitors and Their Performance Metrics: Asymmetric versus Hybrid Supercapacitors, *Small*, 2020, **16**, 2002806.

35 J. M. Gonçalves, M. I. da Silva, M. Hasheminejad, H. E. Toma, K. Araki, P. R. Martins and L. Angnes, Recent Progress in Core@Shell Sulfide Electrode Materials for Advanced Supercapacitor Devices, *Batteries Supercaps*, 2021, **4**, 1397.

36 R. Wang, M. Yao and Z. Niu, Smart supercapacitors from materials to devices, *InfoMat*, 2020, **2**, 113–125.

37 M. D. Stoller, S. A. Stoller, N. Quarles, J. W. Suk, S. Murali, Y. Zhu, X. Zhu and R. S. Ruoff, Using coin cells for ultracapacitor electrode material testing, *J. Appl. Electrochem.*, 2011, **41**, 681.

38 M. Yu and X. Feng, Thin-Film Electrode-Based Supercapacitors, *Joule*, 2019, **3**, 338–360.

39 D. Chen, K. Jiang, T. Huang and G. Shen, Recent Advances in Fiber Supercapacitors: Materials, Device Configurations, and Applications, *Adv. Mater.*, 2020, **32**, 1901806.

40 F. Bu, W. Zhou, Y. Xu, Y. Du, C. Guan and W. Huang, Recent developments of advanced micro-supercapacitors: design, fabrication and applications, *npj Flexible Electron.*, 2020, **4**, 31.

41 V. Augustyn, P. Simon and B. Dunn, Pseudocapacitive oxide materials for high-rate electrochemical energy storage, *Energy Environ. Sci.*, 2014, **7**, 1597–1614.

42 D. P. Chatterjee and A. K. Nandi, A review on the recent advances in hybrid supercapacitors, *J. Mater. Chem. A*, 2021, **9**, 15880–15918.

43 D. P. Dubal, O. Ayyad, V. Ruiz and P. Gómez-Romero, Hybrid energy storage: the merging of battery and supercapacitor chemistries, *Chem. Soc. Rev.*, 2015, **44**, 1777–1790.

44 D. Qian, C. Ma, K. L. More, Y. S. Meng and M. Chi, Advanced analytical electron microscopy for lithium-ion batteries, *NPG Asia Mater.*, 2015, **7**, e193.

45 H. Cheng, J. G. Shapter, Y. Li and G. Gao, Recent progress of advanced anode materials of lithium-ion batteries, *J. Energy Chem.*, 2021, **57**, 451–468.

46 Y. Han, Y. Lei, J. Ni, Y. Zhang, Z. Geng, P. Ming, C. Zhang, X. Tian, J.-L. Shi, Y.-G. Guo and Q. Xiao, Single-Crystalline Cathodes for Advanced Li-Ion Batteries: Progress and Challenges, *Small*, 2022, 2107048.

47 Y. Lu, Q. Zhang and J. Chen, Recent progress on lithium-ion batteries with high electrochemical performance, *Sci. China: Chem.*, 2019, **62**, 533–548.

48 J. M. Tarascon and M. Armand, Issues and challenges facing rechargeable lithium batteries, *Nature*, 2001, **414**, 359–367.

49 S.-W. Kim, D.-H. Seo, X. Ma, G. Ceder and K. Kang, Electrode Materials for Rechargeable Sodium-Ion Batteries: Potential Alternatives to Current Lithium-Ion Batteries, *Adv. Energy Mater.*, 2012, **2**, 710–721.

50 Y. Li and J. Lu, Metal–Air Batteries: Will They Be the Future Electrochemical Energy Storage Device of Choice?, *ACS Energy Lett.*, 2017, **2**, 1370–1377.

51 H.-F. Wang and Q. Xu, Materials Design for Rechargeable Metal–Air Batteries, *Matter*, 2019, **1**, 565–595.

52 K. Yoo, S. Banerjee, J. Kim and P. Dutta, A Review of Lithium–Air Battery Modeling Studies, *Energies*, 2017, **10**, 1748.

53 Y. Huang, Y. Wang, C. Tang, J. Wang, Q. Zhang, Y. Wang and J. Zhang, Atomic Modulation and Structure Design of Carbons for Bifunctional Electrocatalysis in Metal–Air Batteries, *Adv. Mater.*, 2019, **31**, 1803800.

54 Z. Ma, X. Yuan, L. Li, Z.-F. Ma, D. P. Wilkinson, L. Zhang and J. Zhang, A review of cathode materials and structures for rechargeable lithium–air batteries, *Energy Environ. Sci.*, 2015, **8**, 2144–2198.

55 K. Song, B. Yang, Z. Li, Y. Lv, Y. Yu, L. Yuan, X. Shen and X. Hu, Direct synthesis of ACo_2O_4 ($\text{A} = \text{Ni, Cu, Fe, Zn}$) nanowires on carbon cloth as an oxygen electrode catalyst for rechargeable lithium–oxygen batteries, *Appl. Surf. Sci.*, 2020, **529**, 147064.

56 T. Ramachandran and F. Hamed, Electrochemical performance of plate-like zinc cobaltite electrode material for supercapacitor applications, *J. Phys. Chem. Solids*, 2018, **121**, 93–101.

57 X. Liu, Q. Li, Y. Qin and Y. Jiang, Constructing high-performance electrode materials using core–shell $\text{ZnCo}_2\text{O}_4@\text{PPy}$ nanowires for hybrid batteries and water splitting, *RSC Adv.*, 2020, **10**, 28324–28331.

58 D. Yu, Z. Zhang, Y. n Meng, Y. Teng, Y. Wu, X. Zhang, Q. Sun, W. Tong, X. Zhao and X. Liu, The synthesis of hierarchical $\text{ZnCo}_2\text{O}_4@\text{MnO}_2$ core–shell nanosheet arrays



on Ni foam for high-performance all-solid-state asymmetric supercapacitors, *Inorg. Chem. Front.*, 2018, **5**, 597–604.

59 L. Merabet, K. Rida and N. Boukmouche, Sol-gel synthesis, characterization, and supercapacitor applications of MCo_2O_4 ($\text{M} = \text{Ni, Mn, Cu, Zn}$) cobaltite spinels, *Ceram. Int.*, 2018, **44**, 11265–11273.

60 K. Prasad, G. Rajasekhar Reddy, M. Rajesh, P. R. Babu, G. Shanmugam, N. J. Sushma, M. S. Pratap Reddy and B. Deva, Electrochemical Performance of 2D-Hierarchical Sheet-Like ZnCo_2O_4 Microstructures for Supercapacitor Applications, *Crystals*, 2020, **10**, 566, DOI: [10.3390/crust10070566](https://doi.org/10.3390/crust10070566).

61 D. M. Alqahtani, C. Zequine, C. K. Ranaweera, K. Siam, P. K. Kahol, T. P. Poudel, S. R. Mishra and R. K. Gupta, Effect of metal ion substitution on electrochemical properties of cobalt oxide, *J. Alloys Compd.*, 2019, **771**, 951–959.

62 Y. Shang, T. Xie, C. Ma, L. Su, Y. Gai, J. Liu and L. Gong, Synthesis of hollow ZnCo_2O_4 microspheres with enhanced electrochemical performance for asymmetric supercapacitor, *Electrochim. Acta*, 2018, **286**, 103–113.

63 B. Saravanakumar, G. Ravi, R. Yuvakkumar, V. Ganesh, S. Ravichandran, M. Thambidurai and A. Sakunthala, Hydrothermal synthesis and electrochemical properties of ZnCo_2O_4 microspheres, *Ionics*, 2019, **25**, 353–360.

64 H. Chen, J. Wang, X. Han, F. Liao, Y. Zhang, X. Han and C. Xu, Simple growth of mesoporous zinc cobaltite urchin-like microstructures towards high-performance electrochemical capacitors, *Ceram. Int.*, 2019, **45**, 4059–4066.

65 H. Chen, J. Wang, X. Han, F. Liao, Y. Zhang, L. Gao and C. Xu, Facile synthesis of mesoporous ZnCo_2O_4 hierarchical microspheres and their excellent supercapacitor performance, *Ceram. Int.*, 2019, **45**, 8577–8584.

66 R. R. Gutturu, T. V. M. Sreekanth, R. Rajavaram, D. P. R. Borelli, G. R. Dillip, P. C. Nagajyothi and J. Shim, Effect of reaction time and PVP contents on morphologies of hierarchical 3D flower-like ZnCo_2O_4 microstructures for energy storage devices, *Int. J. Energy Res.*, 2020, **44**, 11233–11247.

67 J. Bhagwan, Sk. Khaja Hussain and J. S. Yu, Aqueous asymmetric supercapacitors based on ZnCo_2O_4 nanoparticles *via* facile combustion method, *J. Alloys Compd.*, 2020, **815**, 152456.

68 Y. Shang, T. Xie, Y. Gai, L. Su, L. Gong, H. Lv and F. Dong, Self-assembled hierarchical peony-like ZnCo_2O_4 for high-performance asymmetric supercapacitors, *Electrochim. Acta*, 2017, **253**, 281–290.

69 M. Priya, V. K. Premkumar, P. Vasanharani and G. Sivakumar, Structural and electrochemical properties of ZnCo_2O_4 nanoparticles synthesized by hydrothermal method, *Vacuum*, 2019, **167**, 307–312.

70 D. Song, J. Zhu, J. Li, T. Pu, B. Huang, C. Zhao, L. Xie and L. Chen, Free-standing Two-dimensional Mesoporous ZnCo_2O_4 Thin Sheets Consisting of 3D Ultrathin Nanoflake Array Frameworks for High Performance Asymmetric Supercapacitor, *Electrochim. Acta*, 2017, **257**, 455–464.

71 A. J. C. Mary and A. C. Bose, Surfactant assisted ZnCo_2O_4 nanomaterial for supercapacitor application, *Appl. Surf. Sci.*, 2018, **449**, 105–112.

72 J. Zhu, D. Song, T. Pu, J. Li, B. Huang, W. Wang, C. Zhao, L. Xie and L. Chen, Two-dimensional porous ZnCo_2O_4 thin sheets assembled by 3D nanoflake array with enhanced performance for aqueous asymmetric supercapacitor, *Chem. Eng. J.*, 2018, **336**, 679–689.

73 X. Xiao, G. Wang, M. Zhang, Z. Wang, R. Zhao and Y. Wang, Electrochemical performance of mesoporous ZnCo_2O_4 nanosheets as an electrode material for supercapacitor, *Ionics*, 2018, **24**, 2435–2443.

74 P. Sivakumar, P. Nakhanivej, C. J. Raj and H. S. Park, 3D flower-like oxygen-deficient non-stoichiometry zinc cobaltite for high performance hybrid supercapacitors, *Int. J. Energy Res.*, 2021, **45**, 10832–10842.

75 A. J. C. Mary, S. Thilagavathi and A. C. Bose, Influence of different synthesis approach on ZnCo_2O_4 nanomaterial and its supercapacitor behavior, *AIP Conf. Proc.*, 2018, **1942**, 140042.

76 D. He, Y. Gao, Y. Yao, L. Wu, J. Zhang, Z.-H. Huang and M.-X. Wang, Asymmetric Supercapacitors Based on Hierarchically Nanoporous Carbon and ZnCo_2O_4 From a Single Biometallic Metal-Organic Frameworks (Zn/Co-MOF), *Front. Chem.*, 2020, **8**, 719.

77 S. Zhao, X. Yu, H. Chen, K. Tao, Y. Hu and L. Han, Zeolitic imidazolate framework derived ZnCo_2O_4 hollow tubular nanofibers for long-life supercapacitors, *RSC Adv.*, 2020, **10**, 13922–13928.

78 X. Wu, L. Meng, Q. Wang, W. Zhang and Y. Wang, Highly flexible and large areal/volumetric capacitances for asymmetric supercapacitor based on ZnCo_2O_4 nanorods arrays and polypyrrole on carbon cloth as binder-free electrodes, *Mater. Lett.*, 2019, **234**, 1–4.

79 G. P. Kamble, A. A. Kashale, S. S. Kolekar, I. W. P. Chen, B. R. Sathe and A. V. Ghule, Reflux temperature-dependent zinc cobaltite nanostructures for asymmetric supercapacitors, *J. Mater. Sci.: Mater. Electron.*, 2021, **32**, 5859–5869.

80 M. S. Javed, A. J. Khan, S. Asim, S. S. A. Shah, T. Najam, S. H. Siyal, M. F. Tahir, Z. Zhao and W. Mai, Insights to pseudocapacitive charge storage of binary metal-oxide nanobelts decorated activated carbon cloth for highly-flexible hybrid-supercapacitors, *J. Energy Storage*, 2020, **31**, 101602.

81 Z. Zhang, X. Zhang, Y. Feng, X. Wang, Q. Sun, D. Yu, W. Tong, X. Zhao and X. Liu, Fabrication of porous ZnCo_2O_4 nanoribbon arrays on nickel foam for high-performance supercapacitors and lithium-ion batteries, *Electrochim. Acta*, 2018, **260**, 823–829.

82 G. Rajeshkhan and G. Ranga, Rao, High energy density symmetric capacitor using zinc cobaltate flowers grown *in situ* on Ni foam, *Electrochim. Acta*, 2018, **261**, 265–274.

83 G. J. H. Lim, X. Liu, C. Guan and J. Wang, Co/Zn bimetallic oxides derived from metal organic frameworks for high performance electrochemical energy storage, *Electrochim. Acta*, 2018, **291**, 177–187.

84 B. Saravanakumar, T. H. Ko and B.-S. Kim, Rational design of binder-free ZnCo_2O_4 and Fe_2O_3 decorated porous 3D Ni as high-performance electrodes for asymmetric supercapacitor, *Ceram. Int.*, 2018, **44**, 10635–10645.



85 Y. Zhou, L. Chen, Y. Jiao, Z. Li and Y. Gao, Controllable fabrication of ZnCo_2O_4 ultra-thin curved sheets on Ni foam for high-performance asymmetric supercapacitors, *Electrochim. Acta*, 2019, **299**, 388–394.

86 X. Li, M. Zhang, L. Wu, Q. Fu and H. Gao, Annealing temperature dependent ZnCo_2O_4 nanosheet arrays supported on Ni foam for high-performance asymmetric supercapacitor, *J. Alloys Compd.*, 2019, **773**, 367–375.

87 M. S. Javed, N. Shaheen, S. Hussain, J. Li, S. S. A. Shah, Y. Abbas, M. A. Ahmad, R. Raza and W. Mai, An ultra-high energy density flexible asymmetric supercapacitor based on hierarchical fabric decorated with 2D bimetallic oxide nanosheets and MOF-derived porous carbon polyhedra, *J. Mater. Chem. A*, 2019, **7**, 946–957.

88 W. Wang, L. Chen, J. Qi, Y. Sui, Y. He, Q. Meng, F. Wei and Z. Sun, All-solid-state asymmetric supercapacitor based on N-doped activated carbon derived from polyvinylidene fluoride and ZnCo_2O_4 nanosheet arrays, *J. Mater. Sci.: Mater. Electron.*, 2018, **29**, 2120–2130.

89 M. Saghafi, S. A. Hosseini, S. Zangeneh, A. H. Moghanian and S. Mohajerzadeh, Ternary nanostructured MZnCo oxides ($\text{M} = \text{Al, Mg, Cu, Fe, Ni}$) prepared by hydrothermal method as excellent charge storage devices, *Ionics*, 2020, **26**, 1491–1505.

90 Y. A. Kumar, K. D. Kumar and H.-J. Kim, Reagents assisted ZnCo_2O_4 nanomaterial for supercapacitor application, *Electrochim. Acta*, 2020, **330**, 135261.

91 C. Du, E. Han, L. Sun, S. Qiao and L. Li, Template agent for assisting in the synthesis of ZnCo_2O_4 on Ni foam for high-performance supercapacitors, *Ionics*, 2020, **26**, 383–391.

92 L. Cheng, M. Xu, Q. Zhang, G. Li, J. Chen and Y. Lou, NH_4F assisted and morphology-controlled fabrication of ZnCo_2O_4 nanostructures on Ni-foam for enhanced energy storage devices, *J. Alloys Compd.*, 2019, **781**, 245–254.

93 M. Saghafi and S. Zangeneh, Zn-Co oxide electrodes with excellent capacitive behavior for using supercapacitor application, *Curr. Appl. Phys.*, 2019, **19**, 745–755.

94 G. P. Kamble, A. A. Kashale, S. S. Dhanayat, S. S. Kolekar and A. V. Ghule, Binder-free synthesis of high-quality nanocrystalline ZnCo_2O_4 thin film electrodes for supercapacitor application, *Bull. Mater. Sci.*, 2019, **42**, 272.

95 D. Xie, R.-j. Zhong, D. Ren, L.-y. Tuo, G.-h. Song and F. Hu, Self-assembled ZnCo_2O_4 micro-urchins as high-performance electrode materials for energy storage device, *J. Mater. Sci.: Mater. Electron.*, 2019, **30**, 6439–6447.

96 S. Wang, Y. Teng, X. Liu, D. Yu, Y. n Meng, Y. Wu, S. Sun, X. Zhao and X. Liu, Facile synthesis of mesoporous ZnCo_2O_4 nanowire arrays and nanosheet arrays directly grown on nickel foam for high-performance supercapacitors, *Inorg. Chem. Commun.*, 2019, **101**, 16–22.

97 H. Yu, H. Zhao, Y. Wu, B. Chen and J. Sun, Electrospun $\text{ZnCo}_2\text{O}_4/\text{C}$ composite nanofibers with superior electrochemical performance for supercapacitor, *J. Phys. Chem. Solids*, 2020, **140**, 109385.

98 H. Li, L. Wang, Y. Guan, Y. Su, J. Mu, H. Che, A. Liu and Z. Guo, Facile solvothermal synthesis of $\text{ZnCo}_2\text{O}_4/\text{MnO}_2$ nanosheets composite with enhanced electrochemical properties as supercapacitor electrodes, *Appl. Phys. A: Mater. Sci. Process.*, 2018, **124**, 485.

99 J. Sun, S. Li, X. Han, F. Liao, Y. Zhang, L. Gao, H. Chen and C. Xu, Rapid hydrothermal synthesis of snowflake-like $\text{ZnCo}_2\text{O}_4/\text{ZnO}$ mesoporous microstructures with excellent electrochemical performances, *Ceram. Int.*, 2019, **45**, 12243–12250.

100 H. M. Shaikh, N. Siva Kumar and A. Mahmood, Synthesis of carbon nanoparticles/zinc oxide/zinc cobalt oxide composite and its electrochemical properties, *Ceram. Int.*, 2020, **46**, 18096–18100.

101 N. S. Kumar, V. R. Minnam Reddy, M. Asif, M. Boumaza and K. Mallikarjuna, Reaction time dependent in situ synthesized and morphology altered chrysanthemum to marigold -flower like zinc cobaltite and zinc oxide composite for energy storage devices, *J. Taiwan Inst. Chem. Eng.*, 2020, **116**, 92–100.

102 C. Huang, C. Hao, Z. Ye, S. Zhou, X. Wang, L. Zhu and J. Wu, In situ growth of ZIF-8-derived ternary $\text{ZnO}/\text{ZnCo}_2\text{O}_4/\text{NiO}$ for high performance asymmetric supercapacitors, *Nanoscale*, 2019, **11**, 10114–10128.

103 L. Wang, Y. Guan, X. Zhao, J. Mu, H. Che, H. Li and Z. Guo, $\text{ZnCo}_2\text{O}_4@\text{MnCo}_2\text{O}_4$ heterojunction structured nanosheets for high-performance supercapacitor, *J. Mater. Sci.: Mater. Electron.*, 2018, **29**, 5782–5790.

104 A. J. Christina Mary, C. I. Sathish, P. S. Murphin Kumar, A. Vinu and A. C. Bose, Fabrication of hybrid supercapacitor device based on $\text{NiCo}_2\text{O}_4@\text{ZnCo}_2\text{O}_4$ and the biomass-derived N-doped activated carbon with a honeycomb structure, *Electrochim. Acta*, 2020, **342**, 136062.

105 S. Zhou, C. Hao, J. Wang, X. Wang and H. Gao, Metal-organic framework templated synthesis of porous $\text{NiCo}_2\text{O}_4/\text{ZnCo}_2\text{O}_4/\text{Co}_3\text{O}_4$ hollow polyhedral nanocages and their enhanced pseudocapacitive properties, *Chem. Eng. J.*, 2018, **351**, 74–84.

106 A. J. C. Mary, C. I. Sathish, A. Vinu and A. C. Bose, Electrochemical Performance of rGO/ $\text{NiCo}_2\text{O}_4@\text{ZnCo}_2\text{O}_4$ Ternary Composite Material and the Fabrication of an all-Solid-State Supercapacitor Device, *Energy Fuels*, 2020, **34**, 10131–10141.

107 Y. Huang, X. Feng, C. Li, Y. Li, X. Chen, X. Gao, C. Chen, Z. Guang and P. Liu, Construction of hydrangea-like $\text{ZnCo}_2\text{O}_4/\text{Ni}_3\text{V}_2\text{O}_8$ hierarchical nanostructures for asymmetric all-solid-state supercapacitors, *Ceram. Int.*, 2019, **45**, 15451–15457.

108 V. S. Kumbhar and D.-H. Kim, Hierarchical coating of MnO_2 nanosheets on ZnCo_2O_4 nanoflakes for enhanced electrochemical performance of asymmetric supercapacitors, *Electrochim. Acta*, 2018, **271**, 284–296.

109 W. Cong, R. Miao, B. Tao and F. Miao, $\text{MnO}_2/\text{ZnCo}_2\text{O}_4$ with binder-free arrays on nickel foam loaded with graphene as a high performance electrode for advanced asymmetric supercapacitors, *RSC Adv.*, 2019, **9**, 32889–32897.

110 B. D. Boruah and A. Misra, Voltage Generation in Optically Sensitive Supercapacitor for Enhanced Performance, *ACS Appl. Energy Mater.*, 2019, **2**, 278–286.



111 T.-F. Yi, Y.-M. Li, J.-Z. Wu, Y. Xie and S. Luo, Hierarchical mesoporous flower-like ZnCo_2O_4 @NiO nanoflakes grown on nickel foam as high-performance electrodes for supercapacitors, *Electrochim. Acta*, 2018, **284**, 128–141.

112 Y. Tong, X. Cheng, D. Qi, B. Chi and W. Zhang, Hybrid ZnCo_2O_4 @ Co_3S_4 Nanowires for High-Performance Asymmetric Supercapacitors, *J. Nanoelectron. Optoelectron.*, 2020, **15**, 1552–1558.

113 X. Wang, P. Wu, Z. Zhao, L. Sun, Q. Deng, Z. Yin and X. Chen, Construction of flower-like ZnCo_2S_4 / ZnCo_2O_4 arrays on Ni foam for high-performance asymmetric supercapacitors, *J. Mater. Sci.: Mater. Electron.*, 2020, **31**, 4895–4904.

114 J. Zhao, H. Li, C. Li, Q. Zhang, J. Sun, X. Wang, J. Guo, L. Xie, J. Xie, B. He, Z. Zhou, C. Lu, W. Lu, G. Zhu and Y. Yao, MOF for template-directed growth of well-oriented nanowire hybrid arrays on carbon nanotube fibers for wearable electronics integrated with triboelectric nanogenerators, *Nano Energy*, 2018, **45**, 420–431.

115 X. Jia, X. Wu and B. Liu, Formation of ZnCo_2O_4 @ MnO_2 core–shell electrode materials for hybrid supercapacitor, *Dalton Trans.*, 2018, **47**, 15506–15511.

116 D. S. Patil, A. M. Teli, W. J. Choi, S. A. Pawar, J. C. Shin and H. J. Kim, An all chemical route to design a hybrid battery-type supercapacitor based on ZnCo_2O_4 / CdS composite nanostructures, *Curr. Appl. Phys.*, 2020, **20**, 1416–1423.

117 D. Yang, Y. Wang, Q. Wang, W. Wang, T. Wei and Y. Sun, Preparation and supercapacitive properties of hierarchical ZnCo_2O_4 @ Ni_3S_2 core/shell nanowire arrays on Ni foam, *Mater. Lett.*, 2018, **213**, 222–226.

118 H. Xuan, H. Li, J. Gao, Y. Guan, Z. Xie, X. Liang, H. Li, P. Han and Y. Wu, Construction of hierarchical core–shell ZnCo_2O_4 @Ni–Co–S nanosheets with a microsphere structure on nickel foam for high-performance asymmetric supercapacitors, *Appl. Surf. Sci.*, 2020, **513**, 145893.

119 Y. n Meng, D. Yu, Y. Teng, H. Qi, X. Liu, Y. Wu, X. Zhao and X. Liu, Coating of the NiMoO_4 nanosheets on different-morphology ZnCo_2O_4 nanoarrays on Ni foam and their application in battery-supercapacitor hybrid devices, *J. Energy Storage*, 2020, **29**, 101195.

120 J. Wang, S. Wang, Y. Tian, X. Jin and J. Dong, 3D heterogeneous ZnCo_2O_4 @ NiMoO_4 nanoarrays grown on Ni foam as a binder-free electrode for high-performance energy storage, *J. Energy Storage*, 2020, **32**, 101899.

121 C. Chen, S. Wang, X. Luo, W. Gao, G. Huang, Y. Zeng and Z. Zhu, Reduced ZnCo_2O_4 @ $\text{NiMoO}_4\cdot\text{H}_2\text{O}$ heterostructure electrodes with modulating oxygen vacancies for enhanced aqueous asymmetric supercapacitors, *J. Power Sources*, 2019, **409**, 112–122.

122 Y. n Meng, D. Yu, Y. Teng, X. Liu and X. Liu, A high-performance electrode based on the ZnCo_2O_4 @ CoMoO_4 core–shell nanosheet arrays on nickel foam and their application in battery-supercapacitor hybrid device, *Electrochim. Acta*, 2020, **347**, 136278.

123 L. Xie, Y. Liu, H. Bai, C. Li, B. Mao, L. Sun and W. Shi, Core–shell structured ZnCo_2O_4 @ ZnWO_4 nanowire arrays on nickel foam for advanced asymmetric supercapacitors, *J. Colloid Interface Sci.*, 2018, **531**, 64–73.

124 L. Ma, Z. Chang, L. Guo, T. Li, G. Li and K. Wang, String-like core–shell ZnCo_2O_4 @ NiWO_4 nanowire/nanosheet arrays on Ni foam for binder-free supercapacitor electrodes, *Ionics*, 2020, **26**, 2537–2547.

125 Y. Anil Kumar, S. Sambasivam, S. Ahmed Hira, K. Zeb, W. Uddin, T. N. V. Krishna, K. Dasha Kumar, I. M. Obaidat and H.-J. Kim, Boosting the energy density of highly efficient flexible hybrid supercapacitors via selective integration of hierarchical nanostructured energy materials, *Electrochim. Acta*, 2020, **364**, 137318.

126 X. Han, Y. Yang, J.-J. Zhou, Q. Ma, K. Tao and L. Han, Metal–Organic Framework Tempted 3D Hierarchical ZnCo_2O_4 @ Ni(OH)_2 Core–Shell Nanosheet Arrays for High-Performance Supercapacitors, *Chem. – Eur. J.*, 2018, **24**, 18106–18114.

127 X. Bai, D. Cao and H. Zhang, Constructing ZnCo_2O_4 @LDH Core–Shell hierarchical structure for high performance supercapacitor electrodes, *Ceram. Int.*, 2019, **45**, 14943–14952.

128 M. Li, W. Yang, Y. Huang and Y. Yu, Hierarchical mesoporous Co_3O_4 @ ZnCo_2O_4 hybrid nanowire arrays supported on Ni foam for high-performance asymmetric supercapacitors, *Sci. China Mater.*, 2018, **61**, 1167–1176.

129 L. Wu, L. Sun, X. Li, Q. Zhang, H. Si, Y. Zhang, K. Wang and Y. Zhang, Mesoporous ZnCo_2O_4 -CNT microflowers as bifunctional material for supercapacitive and lithium energy storage, *Appl. Surf. Sci.*, 2020, **506**, 144964.

130 J. Bao, Z. Wang, W. Liu, L. Xu, F. Lei, J. Xie, Y. Zhao, Y. Huang, M. Guan and H. Li, ZnCo_2O_4 ultrathin nanosheets towards the high performance of flexible supercapacitors and bifunctional electrocatalysis, *J. Alloys Compd.*, 2018, **764**, 565–573.

131 A. Kathalingam, S. Ramesh, H. M. Yadav, J.-H. Choi, H. S. Kim and H.-S. Kim, Nanosheet-like ZnCo_2O_4 @nitrogen doped graphene oxide/polyaniline composite for supercapacitor application: Effect of polyaniline incorporation, *J. Alloys Compd.*, 2020, **830**, 154734.

132 X. Wei, H. Wu and L. Li, 3D N-doped carbon continuous network supported P-doped ZnCo_2O_4 nanosheets with rich oxygen vacancies for high-performance asymmetric pseudocapacitor, *J. Alloys Compd.*, 2021, **861**, 158544.

133 S. J. Patil, D. P. Dubal and D.-W. Lee, Gold nanoparticles decorated rGO- ZnCo_2O_4 nanocomposite: A promising positive electrode for high performance hybrid supercapacitors, *Chem. Eng. J.*, 2020, **379**, 122211.

134 J. Bhagwan, G. Nagaraju, B. Ramulu and J. S. Yu, Promotive Effect of MWCNT on ZnCo_2O_4 Hexagonal Plates and Their Application in Aqueous Asymmetric Supercapacitor, *J. Electrochem. Soc.*, 2019, **166**, A217–A224.

135 M. Sharma and A. Gaur, Designing of Carbon Nitride Supported ZnCo_2O_4 Hybrid Electrode for High-Performance Energy Storage Applications, *Sci. Rep.*, 2020, **10**, 2035.

136 V. Shanmugavalli, O. V. Saravanan, K. Vishista and R. Saravanan, A study of charge density distribution and



enhanced electrochemical properties of zinc cobaltite/polyaniline nanocomposite for supercapacitor application, *Ionics*, 2019, **25**, 4393–4408.

137 Z. Gao, L. Zhang, J. Chang, Z. Wang, D. Wu, F. Xu, Y. Guo and K. Jiang, ZnCo₂O₄-reduced graphene oxide composite with balanced capacitive performance in asymmetric supercapacitors, *Appl. Surf. Sci.*, 2018, **442**, 138–147.

138 D. Kong, Y. Wang, S. Huang, J. Hu, Y. V. Lim, B. Liu, S. Fan, Y. Shi and H. Y. Yang, 3D self-branched zinc-cobalt Oxide@N-doped carbon hollow nanowall arrays for high-performance asymmetric supercapacitors and oxygen electrocatalysis, *Energy Storage Mater.*, 2019, **23**, 653–663.

139 M. Yan, F. Jiang, Y. Liu, L. Sun, H. Bai, F. Zhu and W. Shi, Flexible mixed metal oxide hollow spheres/RGO hybrid lamellar films for high performance supercapacitors, *Colloids Surf., A*, 2021, **612**, 125902.

140 A. Asghari, S. H. Kazemi and M. Khanmohammadi, Facile and binder-free synthesis of N-doped carbon/ZnCo₂O₄ hybrid nanostructures on nickel foam for high-performance solid-state asymmetric supercapacitor, *J. Mater. Sci.: Mater. Electron.*, 2020, **31**, 4354–4363.

141 Z. Wang, S. Lu, G. He, A. Lv, Y. Shen and W. Xu, In situ construction of dual-morphology ZnCo₂O₄ for high-performance asymmetric supercapacitors, *Nanoscale Adv.*, 2019, **1**, 3086–3094.

142 J. Qi, J. Mao, A. Zhang, L. Jiang, Y. Sui, Y. He, Q. Meng, F. Wei and X. Zhang, Facile synthesis of mesoporous ZnCo₂O₄ nanosheet arrays grown on rGO as binder-free electrode for high-performance asymmetric supercapacitor, *J. Mater. Sci.*, 2018, **53**, 16074–16085.

143 Y. Lu, L. Wang, M. Chen, Y. Wu, G. Liu, P. Qi, M. Fu, H. Wu and Y. Tang, Rationally designed hierarchical ZnCo₂O₄/C core-shell nanowire arrays for high performance and stable supercapacitors, *J. Alloys Compd.*, 2021, **876**, 160037.

144 J. Zhu, Y. Wang, X. Zhang and W. Cai, MOF-derived ZnCo₂O₄@NiCo₂S₄@PPy core-shell nanosheets on Ni foam for high-performance supercapacitors, *Nanotechnology*, 2021, **32**, 145404.

145 J. Gao, H. Xuan, Y. Xu, T. Liang, X. Han, J. Yang, P. Han, D. Wang and Y. Du, Interconnected network of zinc-cobalt layered double hydroxide stick onto rGO/nickel foam for high performance asymmetric supercapacitors, *Electrochim. Acta*, 2018, **286**, 92–102.

146 P. Chen, C. Yang, P. Gao, X. Chen, Y.-J. Cheng, J. Liu and K. Guo, Distinctive Formation of Bifunctional ZnCoS-rGO 3D Hollow Microsphere Flowers with Excellent Energy Storage Performances, *Chem. Mater.*, 2022, **34**, 5896–5911.

147 M. Xu, M. Sun, S. u Rehman, K. Ge, X. Hu, H. Ding, J. Liu and H. Bi, One-pot synthesis of CoO-ZnO/rGO supported on Ni foam for high-performance hybrid supercapacitor with greatly enhanced cycling stability, *Chin. Chem. Lett.*, 2021, **32**, 2027–2032.

148 J. B. Goodenough and K.-S. Park, The Li-Ion Rechargeable Battery: A Perspective, *J. Am. Chem. Soc.*, 2013, **135**, 1167–1176.

149 X. Liu, J.-Q. Huang, Q. Zhang and L. Mai, Nanostructured Metal Oxides and Sulfides for Lithium–Sulfur Batteries, *Adv. Mater.*, 2017, **29**, 1601759.

150 B. Xu, D. Qian, Z. Wang and Y. S. Meng, Recent progress in cathode materials research for advanced lithium ion batteries, *Mater. Sci. Eng., R*, 2012, **73**, 51–65.

151 S. Goriparti, E. Miele, F. De Angelis, E. Di Fabrizio, R. Proietti Zaccaria and C. Capiglia, Review on recent progress of nanostructured anode materials for Li-ion batteries, *J. Power Sources*, 2014, **257**, 421–443.

152 J. Zhang, R. Chu, Y. Chen, H. Jiang, Y. Zhang, N. M. Huang and H. Guo, In-situ grown hierarchical ZnCo₂O₄ nanosheets on nickel foam as binder-free anode for lithium ion batteries, *Ceram. Int.*, 2018, **44**, 16219–16226.

153 Z. Li, D. Wang, A. Gu, W. Wei, H. Lv, Z. Lou and Q. Zhou, Ethylene glycol combustion strategy towards 3D mesoporous ZnCo₂O₄ as anodes for Li-ion batteries, *Solid State Ionics*, 2020, **356**, 115461.

154 R. A. Adams, V. G. Pol and A. Varma, Tailored Solution Combustion Synthesis of High Performance ZnCo₂O₄ Anode Materials for Lithium-Ion Batteries, *Ind. Eng. Chem. Res.*, 2017, **56**, 7173–7183.

155 M. Wang, Y. Huang, Y. Zhu, N. Zhang, J. Zhang, X. Qin and H. Zhang, Synthesis of porous Zn_xCo_{3-x}O₄ hollow nano-boxes derived from metal-organic frameworks for lithium and sodium storage, *Electrochim. Acta*, 2020, **335**, 135694.

156 J. Du, Y. Tang, Y. Wang, P. Shi, J. Fan, Q. Xu and Y. Min, A MOF-derived method to construct well-arranged porous nanosheets for lithium ion batteries, *Dalton Trans.*, 2018, **47**, 7571–7577.

157 Y. Song, M. Zhao, Z. Pan, L. Jiang, Y. Jiang, B. Fu, J. Xu and L. Hu, Thermal transformation of ZnCo_{1.5}(OH)_{4.5}Cl_{0.5}·0.45H₂O into hexagonal ZnCo₂O₄ nanosheets for high-performance secondary ion batteries, *J. Alloys Compd.*, 2019, **783**, 455–459.

158 H. Xu, Y. Zhang, X. Song, X. Kong, T. Ma and H. Wang, Synthesis of porous ZnCo₂O₄ micro-cube with large tap density and its application in anode for lithium-ion battery, *J. Alloys Compd.*, 2020, **821**, 153289.

159 L. Wang, M. Zhen, F. Hu, H. Wang, H. Jia and M. Wei, Construction of three-dimensional ZnCo₂O₄ hierarchical nanocubes for enhanced lithium storage performances, *Mater. Lett.*, 2021, **286**, 129231.

160 Z. Chen, F. Chen, Y. Wang and Y. Jiang, Facile template-free one-pot fabrication of ZnCo₂O₄ nanospheres for advanced lithium storage capability, *Ionics*, 2017, **23**, 3323–3328.

161 J. Deng, X. Yu, X. Qin, B. Li and F. Kang, Carbon sphere-templated synthesis of porous yolk-shell ZnCo₂O₄ spheres for high-performance lithium storage, *J. Alloys Compd.*, 2019, **780**, 65–71.

162 Y. Gu, Y. Xuan, H. Zhang, X. Deng, Y. Sun and L. Wang, A facile route to prepare mixed transition metal oxide yolk-shell microspheres for enhanced lithium storage, *Dalton Trans.*, 2019, **48**, 10604–10609.

163 H. Liu and Q. Hu, Novel secondary assembled micro/nano porous spheres ZnCo₂O₄ with superior electrochemical



performances as lithium ion anode material, *Nanotechnology*, 2018, **29**, 325603.

164 D. Xue, F. Xue, X. Lin, F. Zong, J. Zhang and Q. Li, Coordination polymer derived general synthesis of multi-shelled hollow metal oxides for lithium-ion batteries, *Nanoscale*, 2019, **11**, 17478–17484.

165 H. Liu, X. Wang, H. Xu, J. Wang, Q. Ma, W. Yu, Y. Yang, X. Dong, G. Liu and Y. Zhao, Controllable synthesis of nanostructured $ZnCo_2O_4$ as high-performance anode materials for lithium-ion batteries, *RSC Adv.*, 2018, **8**, 39377–39383.

166 B. Liu, H. Liu, M. Liang, L. Liu, Z. Lv, H. Zhou and H. Guo, Controlled synthesis of hollow octahedral $ZnCo_2O_4$ nanocages assembled from ultrathin 2D nanosheets for enhanced lithium storage, *Nanoscale*, 2017, **9**, 17174–17180.

167 S. Cheng, Q. Ru, P. Liu, H. Yan, Z. Shi, X. Hou, S. Su, L. Zhao and F. Chi-Chung, Ling, Micro-emulsion strategy used to prepare soybean oil-tailored 1D porous $ZnCo_2O_4$ cuboid morphology providing a durable performance of the anodes of lithium ion batteries, *J. Alloys Compd.*, 2019, **809**, 151703.

168 J. Deng, X. Yu, X. Qin, B. Liu, Y.-B. He, B. Li and F. Kang, Controlled synthesis of anisotropic hollow $ZnCo_2O_4$ octahedrons for high-performance lithium storage, *Energy Storage Mater.*, 2018, **11**, 184–190.

169 L. Zhang and S. Zhu, Hollow polyhedral $ZnCo_2O_4$ anode materials for lithium-ion batteries, *Mater. Lett.*, 2019, **236**, 337–341.

170 H. Du, K. Huang, W. Dong and B. Geng, A general gelatin-assisted strategy to hierarchical porous transition metal oxides with excellent lithium-ion storage, *Electrochim. Acta*, 2018, **279**, 66–73.

171 J. Liu, Y. Xuan, D. G. D. Galpaya, Y. Gu, Z. Lin, S. Zhang, C. Yan, S. Feng and L. Wang, A high-volumetric-capacity and high-areal-capacity $ZnCo_2O_4$ anode for Li-ion batteries enabled by a robust biopolymer binder, *J. Mater. Chem. A*, 2018, **6**, 19455–19462.

172 M.-H. Jung, The two-dimensional to three-dimensional transition structures of $ZnCo_2O_4$ for the application of lithium-ion batteries, *Appl. Surf. Sci.*, 2018, **427**, 293–301.

173 C. R. Mariappan, V. Kumar, R. Azmi, L. Esmezjan, S. Indris, M. Bruns and H. Ehrenberg, High electrochemical performance of 3D highly porous $Zn_{0.2}Ni_{0.8}Co_2O_4$ microspheres as an electrode material for electrochemical energy storage, *CrystEngComm*, 2018, **20**, 2159–2168.

174 Y. Mo, J. Liu, S. Wang, M. Xiao, S. Ren, D. Han and Y. Meng, Low-Carbon and Nanosheathed $ZnCo_2O_4$ Spheroids with Porous Architecture for Boosted Lithium Storage Properties, *Research*, 2019, **2019**, 1354829.

175 D. Darbar, M. R. Anilkumar, V. Rajagopalan, I. Bhattacharya, H. I. Elim, T. Ramakrishnappa, F. I. Ezema, R. Jose and M. V. Reddy, Studies on spinel cobaltites, MCo_2O_4 ($M = Mn$, Zn , Fe , Ni and Co) and their functional properties, *Ceram. Int.*, 2018, **44**, 4630–4639.

176 M. Carbone, Zn defective $ZnCo_2O_4$ nanorods as high capacity anode for lithium ion batteries, *J. Electroanal. Chem.*, 2018, **815**, 151–157.

177 S. Guo, J. Liu, Q. Zhang and H. Wang, 3D porous $ZnCo_2O_4$ / Co_3O_4 composite grown on carbon cloth as high-performance anode material for lithium-ion battery, *Mater. Lett.*, 2020, **267**, 127549.

178 F. Li, M. Zheng, Y. You, D. Jiang, H. Yuan, Z. Zhai, W. Zhang, L. Ma and W. Shen, Hierarchical Hollow Bimetal Oxide Microspheres Synthesized through a Recrystallization Mechanism for High-Performance Lithium-Ion Batteries, *ChemElectroChem*, 2020, **7**, 3468–3477.

179 W. Song, K. Ji, A. Aguadero, P. R. Shearing, D. J. L. Brett, F. Xie and D. J. Riley, Co_3O_4 hollow nanospheres doped with $ZnCo_2O_4$ via thermal vapor mechanism for fast lithium storage, *Energy Storage Mater.*, 2018, **14**, 324–334.

180 H. Mao, P. Shen, G. Yang, L. Zhao, X. Qiu, H. Wang and Q. Jiang, 3D highly oriented metal foam: a competitive self-supporting anode for high-performance lithium-ion batteries, *J. Mater. Sci.*, 2020, **55**, 11462–11476.

181 H. Xin, D. Li, L. Shi, M. Ji, Y. Lin, J. Yu, B. Yang, C. Li and C. Zhu, A simple approach to fabricate of $Ni-NiCo_2O_4@ZnCo_2O_4$ yolk-shell nano-tetrahedron composite as high-performance anode material for lithium-ion batteries, *Chem. Eng. J.*, 2018, **341**, 601–609.

182 L. Wang and Q. Yang, $ZnCo_2O_4$ nanoflakes loaded on a Cu-supported Fe_2O_3 -C network as an integrated lithium-ion battery anode, *J. Alloys Compd.*, 2019, **792**, 750–758.

183 X. Deng, S. Li, J. Wang, D. Nan, J. Dong and J. Liu, Nitrogen-doped zinc/cobalt mixed oxide micro-/nanospheres for high-rate lithium-ion battery anode, *J. Mater. Res.*, 2019, **34**, 3204–3211.

184 J. Deng, X. Yu, X. Qin, D. Zhou, L. Zhang, H. Duan, F. Kang, B. Li and G. Wang, Co-B Nanoflakes as Multifunctional Bridges in $ZnCo_2O_4$ Micro-/Nanospheres for Superior Lithium Storage with Boosted Kinetics and Stability, *Adv. Energy Mater.*, 2019, **9**, 1803612.

185 L. Zhang, S. Zhu, X. Li, H. Fang, L. Wang, Y. Song and X. Jia, 3D porous $ZnCo_2O_4@NiO$ on nickel foam as advanced electrodes for lithium storage, *Ionics*, 2020, **26**, 2157–2164.

186 J. Yu, Y. Wang, L. Mou, D. Fang, S. Chen and S. Zhang, Nature-Inspired 2D-Mosaic 3D-Gradient Mesoporous Framework: Bimetal Oxide Dual-Composite Strategy toward Ultrastable and High-Capacity Lithium Storage, *ACS Nano*, 2018, **12**, 2035–2047.

187 Z. Zhang, Y. Huang, X. Liu, X. Wang and P. Liu, Yolk-shell structured $ZnCo_2O_4$ spheres anchored on reduced graphene oxide with enhance lithium/sodium storage performance, *Electrochim. Acta*, 2020, **342**, 136104.

188 H. Ren, W. Wang, S. Woo Joo, Y. Sun and C. Gu, Preparation of $ZnCo_2O_4@$ reduced graphene oxide nanocomposite for high-capacity Li-ion battery anodes, *Mater. Res. Bull.*, 2019, **111**, 34–42.

189 Q. Feng, Y. Du, S. Liang and H. Li, Reduced graphene oxide supported quasi-two-dimensional $ZnCo_2O_4$ nanosheets for lithium ion batteries with high electrochemical stability, *Nanotechnology*, 2019, **31**, 045402.

190 Q. Ru, Z. Wang, S. Cheng, P. Liu, X. Hou, S. Su and F. C.-C. Ling, Self Assembled Rice Ball-Like $ZnCo_2O_4$ Inlaid on rGO



as Flexible Anodes with High Lithium Storage Capability and Superior Cycling Stability, *Energy Technol.*, 2018, **6**, 1899–1903.

191 X. Wang, Q. Chen, P. Zhao and M. Wang, Synthesis of interconnected mesoporous $ZnCo_2O_4$ nanosheets on a 3D graphene foam as a binder-free anode for high-performance Li-ion batteries, *RSC Adv.*, 2018, **8**, 33717–33727.

192 L. Li, Z. Xie, G. Jiang, Y. Wang, B. Cao and C. Yuan, Efficient Laser-Induced Construction of Oxygen-Vacancy Abundant Nano- $ZnCo_2O_4$ /Porous Reduced Graphene Oxide Hybrids toward Exceptional Capacitive Lithium Storage, *Small*, 2020, **16**, 2001526.

193 H. Cao, X. Zhou, W. Deng, Z. Ma, Y. Liu and Z. Liu, Layer structured graphene/porous $ZnCo_2O_4$ composite film for high performance flexible lithium-ion batteries, *Chem. Eng. J.*, 2018, **343**, 654–661.

194 Y. Yang, Z. Li, S. Xu, Y. Tang, C.-S. Lee and W. Zhang, Hierarchically nanostructured $ZnCo_2O_4$ particles in 3D graphene networks for high-rate and long-life lithium ion batteries, *Mater. Today Energy*, 2019, **12**, 46–52.

195 Z. Zhao, G. Tian, V. Trouillet, L. Zhu, J. Zhu, A. Missiul, E. Welter and S. Dsoke, In Operando analysis of the charge storage mechanism in a conversion $ZnCo_2O_4$ anode and the application in flexible Li-ion batteries, *Inorg. Chem. Front.*, 2019, **6**, 1861–1872.

196 T. Huang, Z. Lou, Y. Lu, R. Li, Y. Jiang, G. Shen and D. Chen, Metal-Organic-Framework-Derived MCo_2O_4 ($M = Mn$ and Zn) Nanosheet Arrays on Carbon Cloth as Integrated Anodes for Energy Storage Applications, *ChemElectroChem*, 2019, **6**, 5836–5843.

197 T. Liu, W. Wang, M. Yi, Q. Chen, C. Xu, D. Cai and H. Zhan, Metal-organic framework derived porous ternary $ZnCo_2O_4$ nanoplate arrays grown on carbon cloth as binder-free electrodes for lithium-ion batteries, *Chem. Eng. J.*, 2018, **354**, 454–462.

198 P. Huang, M. Zhang, J. Kang, H. Feng, Q. Su, G. Du, Y. Yu and B. Xu, Rapid microwave-irradiation synthesis of $ZnCo_2O_4/ZnO$ nanocrystals/carbon nanotubes composite as anodes for high-performance lithium-ion battery, *J. Mater. Sci.*, 2018, **54**, 4154–4167.

199 Y. Wang, X. Zhu, D. Liu, H. Tang, G. Luo, K. Tu, Z. Xie, J. Lei, J. Li, X. Li and D. Qu, Synthesis of MOF-74-derived carbon/ $ZnCo_2O_4$ nanoparticles@CNT-nest hybrid material and its application in lithium ion batteries, *J. Appl. Electrochem.*, 2019, **49**, 1103–1112.

200 X. Tang, M. Liang, Y. Zhang, W. Sun and Y. Wang, Ultrafine ternary metal oxide particles with carbon nanotubes: a metal-organic-framework-based approach and superior lithium-storage performance, *Dalton Trans.*, 2019, **48**, 4413–4419.

201 H. Liang, J. Wu, M. Wang, H. Fan and Y. Zhang, Pseudo-capacitance-dominated high-performance and stable lithium-ion batteries from MOF-derived spinel $ZnCo_2O_4/ZnO/C$ heterostructure anode, *Dalton Trans.*, 2020, **49**, 13311–13316.

202 C. Ding, W. Xu, X. Zeng, M. Wang, W. Wang and Z. Qing, Citrate-directed hydrothermal synthesis of $ZnCo_2O_4$ -in-carbon porous microspheres for highly reliable lithium-ion batteries, *Ionics*, 2019, **26**, 703–710.

203 L. Wang, D. Li, J. Zhang, C. Song, H. Xin and X. Qin, Porous flower-like $ZnCo_2O_4$ and $ZnCo_2O_4@C$ composite: a facile controllable synthesis and enhanced electrochemical performance, *Ionics*, 2020, **26**, 4479–4487.

204 C. Ding, W. Xu, M. Wang, X. Zeng and W. Wang, Microstructure controlled $ZnCo_2O_4/C$ microhydrangea nanocomposites as highly reliable anodes for lithium-ion batteries, *Int. J. Energy Res.*, 2019, **44**, 977–987.

205 H. Li, S. Wang, M. Feng, J. Yang and B. Zhang, MOF-derived $ZnCo_2O_4/C$ wrapped on carbon fiber as anode materials for structural lithium-ion batteries, *Chin. Chem. Lett.*, 2019, **30**, 529–532.

206 Z. Dai, Z. Long, R. Li, C. Shi, H. Qiao, K. Wang and K. Liu, Metal–Organic Framework-Structured Porous $ZnCo_2O_4/C$ Composite Nanofibers for High-Rate Lithium-Ion Batteries, *ACS Appl. Energy Mater.*, 2020, **3**, 12378–12384.

207 R. Sun, Z. Qin, Z. Li, H. Fan and S. Lu, Binary zinc-cobalt metal-organic framework derived mesoporous $ZnCo_2O_4@NC$ polyhedron as a high-performance lithium-ion battery anode, *Dalton Trans.*, 2020, **49**, 14237–14242.

208 X. Wu, M. Zeng, L. Wang and J. Li, CTAB-assisted synthesis of $ZnCo_2O_4$ nanoparticles embedded in N-doped carbon as superior anode materials for lithium-ion battery, *J. Alloys Compd.*, 2019, **780**, 897–906.

209 W. Zhao, Z. Shi, Y. Qi and J. Cheng, The Carbon-Coated $ZnCo_2O_4$ Nanowire Arrays Pyrolyzed from PVA for Enhancing Lithium Storage Capacity, *Processes*, 2020, **8**, 1501.

210 Q. Han, X. Zhang, W. Zhang, Y. Li and Z. Zhang, Preparation of multifunctional structural $P-CF@ZnCo_2O_4$ composites used as structural anode materials, *J. Alloys Compd.*, 2020, **842**, 155743.

211 H. Xiao, G. Ma, J. Tan, S. Ru, Z. Ai and C. Wang, Three-dimensional hierarchical $ZnCo_2O_4@C_3N_4-B$ nanoflowers as high-performance anode materials for lithium-ion batteries, *RSC Adv.*, 2020, **10**, 32609–32615.

212 P. Pan, Y. Hu, K. Wu, Z. Cheng, Z. Shen, L. Jiang, J. Mao, C. Ni, Y. Ge and Z. Wang, Growth of $ZnCo_2O_4$ nanocubes on flexible biochar substrate derived from natural silk waste fabric for lithium-ion battery anode, *J. Alloys Compd.*, 2020, **814**, 152306.

213 H. Li, L. Lv, W. Wang, X. Huang and D. Chen, A network of porous carbon/ $ZnCo_2O_4$ nanotubes derived from shell-hybridized worm-like micelles for lithium storage, *J. Mater. Chem. A*, 2019, **7**, 22642–22649.

214 J. Deng, X. Yu, J. Tang, L. Zhang, K. Zhang, S. Lin and B. Li, Highly reversible lithium storage in a conversion-type $ZnCo_2O_4$ anode promoted by $NiCl_{2-x}F_x$ hydrate, *J. Mater. Chem. A*, 2020, **8**, 2356–2363.

215 A. Ghaffar, G. Ali, S. Zawar, M. Hasan, G. M. Mustafa, S. Atiq and S. M. Ramay, Electrochemical performance of Li^+ insertion/extraction in Ni-substituted $ZnCo_2O_4$ as an emerging highly efficient anode material, *RSC Adv.*, 2020, **10**, 28550–28559.

216 C. Liu, B.-H. Chen, W.-R. Liu and J.-G. Duh, Synthesis and theoretical calculations of N-doped $ZnCo_2O_4$ anode for lithium-ion anode via gradient pressure-induced processes



and theoretical calculations, *J. Alloys Compd.*, 2019, **797**, 978–985.

217 W.-T. Koo, H.-Y. Jang, C. Kim, J.-W. Jung, J. Y. Cheong and I.-D. Kim, MOF derived ZnCo_2O_4 porous hollow spheres functionalized with Ag nanoparticles for a long-cycle and high-capacity lithium ion battery anode, *J. Mater. Chem. A*, 2017, **5**, 22717–22725.

218 W. Zhao, Y. Qi, J. Dong, J. Xu, P. Wu and C. Zhang, New insights into the structure-property relation in ZnCo_2O_4 nanowire and nanosheet arrays, *J. Alloys Compd.*, 2020, **817**, 152692.

219 X. Cao, Y. Yang and A. Li, Facile Synthesis of Porous ZnCo_2O_4 Nanosheets and the Superior Electrochemical Properties for Sodium Ion Batteries, *Nanomaterials*, 2018, **8**(6), 377, DOI: [10.3390/nano8060377](https://doi.org/10.3390/nano8060377).

220 X. Yang, P. Wang, Y. Tang, C. Peng, Y. Lai, J. Li and Z. Zhang, Bimetallic ZIF-derived polyhedron ZnCo_2O_4 anchored on the reduced graphene oxide as an anode for sodium-ion battery, *Ionics*, 2019, **25**, 2945–2950.

221 J. Xu, B. Yan, H. Maleki Kheimeh Sari, Y. Hao, D. Xiong, S. Dou, W. Liu, H. Kou, D. Li and X. Li, Mesoporous ZnCo_2O_4 /rGO nanocomposites enhancing sodium storage, *Nanotechnology*, 2019, **30**, 234005.

222 J. Liu, J. Wu, C. Zhou, P. Zhang, S. Guo, S. Li, Y. Yang, K. Li, L. Chen and M. Wang, Single-phase ZnCo_2O_4 derived $\text{ZnO}-\text{CoO}$ mesoporous microspheres encapsulated by nitrogen-doped carbon shell as anode for high-performance lithium-ion batteries, *J. Alloys Compd.*, 2020, **825**, 153951.

223 T. Huang, Z. Lou, Y. Lu, R. Li, Y. Jiang, G. Shen and D. Chen, Metal-Organic-Framework-Derived MCo_2O_4 ($\text{M} = \text{Mn}$ and Zn) Nanosheet Arrays on Carbon Cloth as Integrated Anodes for Energy Storage Applications, *ChemElectroChem*, 2019, **6**, 5836–5843.

224 A. K. Geim and K. S. Novoselov, The rise of graphene, *Nat. mater.*, 2007, **6**, 183–191.

225 C. N. Rao, A. K. Sood, K. S. Subrahmanyam and A. Govindaraj, Graphene: the new two-dimensional nanomaterial, *Angew. Chem., Int. Ed.*, 2009, **48**, 7752–7777.

226 C. N. Rao, K. S. Subrahmanyam, H. S. Ramakrishna Matte, B. Abdulhakeem, A. Govindaraj, B. Das, P. Kumar, A. Ghosh and D. J. Late, A study of the synthetic methods and properties of graphenes, *Sci. Technol. Adv. Mater.*, 2010, **11**, 054502.

227 C.-H. Park, F. Giustino, C. D. Spataru, M. L. Cohen and S. G. Louie, Angle-Resolved Photoemission Spectra of Graphene from First-Principles Calculations, *Nano Lett.*, 2009, **9**, 4234–4239.

228 S. Sahoo, S.-H. Bae, Y.-S. Lee, J.-M. Lee, J.-M. Ahn, C.-G. Kim and I.-K. Oh, Defect-engineered mesoporous ternary nanoarchitecture of zinc-cobalt-oxide/nitrogen-doped graphene as anode material in lithium ion batteries, *Carbon*, 2015, **94**, 455–463.

229 X. Song, X. Li, Z. Bai, B. Yan, D. Xiong, L. Lin, H. Zhao, D. Li and Y. Shao, Rationally-designed configuration of directly-coated $\text{Ni}_3\text{S}_2/\text{Ni}$ electrode by RGO providing superior sodium storage, *Carbon*, 2018, **133**, 14–22.

230 J. M. Gonçalves, P. R. Martins, M. I. da Silva, J. G. Ruiz-Montoya, L. V. Quispe-Garrido and A. Lucio, in *Handbook of Energy Materials*, ed. R. Gupta, Springer Nature Singapore, Singapore, 2022, pp. 1–46, DOI: [10.1007/978-981-16-4480-1_19-1](https://doi.org/10.1007/978-981-16-4480-1_19-1).

231 N. Yabuuchi, K. Kubota, M. Dahbi and S. Komaba, Research Development on Sodium-Ion Batteries, *Chem. Rev.*, 2014, **114**, 11636–11682.

232 C. Yuan, H. B. Wu, Y. Xie and X. W. Lou, Mixed Transition-Metal Oxides: Design, Synthesis, and Energy-Related Applications, *Angew. Chem., Int. Ed.*, 2014, **53**, 1488–1504.

233 J. Muldoon, C. B. Bucur and T. Gregory, Quest for Non-aqueous Multivalent Secondary Batteries: Magnesium and Beyond, *Chem. Rev.*, 2014, **114**, 11683–11720.

234 C. Pan, R. Zhang, R. G. Nuzzo and A. A. Gewirth, $\text{ZnNixMnxCo}_{2-2x}\text{O}_4$ Spinel as a High-Voltage and High-Capacity Cathode Material for Nonaqueous Zn-Ion Batteries, *Adv. Energy Mater.*, 2018, **8**, 1800589.

235 A. Baby, B. Senthilkumar and P. Barpanda, Low-Cost Rapid Template-Free Synthesis of Nanoscale Zinc Spinel for Energy Storage and Electrocatalytic Applications, *ACS Appl. Energy Mater.*, 2019, **2**, 3211–3219.

236 K. Shimokawa, T. Atsumi, M. Harada, R. E. Ward, M. Nakayama, Y. Kumagai, F. Oba, N. L. Okamoto, K. Kanamura and T. Ichitsubo, Zinc-based spinel cathode materials for magnesium rechargeable batteries: toward the reversible spinel–rocksalt transition, *J. Mater. Chem. A*, 2019, **7**, 12225–12235.

237 P. G. Bruce, S. A. Freunberger, L. J. Hardwick and J. M. Tarascon, $\text{Li}-\text{O}_2$ and $\text{Li}-\text{S}$ batteries with high energy storage, *Nat. Mater.*, 2011, **11**, 19–29.

238 M. Du, Q. Li, Y. Zhao, C.-S. Liu and H. Pang, A review of electrochemical energy storage behaviors based on pristine metal–organic frameworks and their composites, *Coord. Chem. Rev.*, 2020, **416**, 213341.

239 X. Ji, K. T. Lee and L. F. Nazar, A highly ordered nanosstructured carbon–sulphur cathode for lithium–sulphur batteries, *Nat. Mater.*, 2009, **8**, 500–506.

240 M. Yan, W.-P. Wang, Y.-X. Yin, L.-J. Wan and Y.-G. Guo, Interfacial design for lithium–sulfur batteries: From liquid to solid, *EnergyChem*, 2019, **1**, 100002.

241 G. Zhou, Y. Zhao and A. Manthiram, Dual-Confined Flexible Sulfur Cathodes Encapsulated in Nitrogen-Doped Double-Shelled Hollow Carbon Spheres and Wrapped with Graphene for Li–S Batteries, *Adv. Energy Mater.*, 2015, **5**, 1402263.

242 Q. Sun, B. Xi, J.-Y. Li, H. Mao, X. Ma, J. Liang, J. Feng and S. Xiong, Nitrogen-Doped Graphene-Supported Mixed Transition-Metal Oxide Porous Particles to Confine Poly-sulfides for Lithium-Sulfur Batteries, *Adv. Energy Mater.*, 2018, **8**, 1800595.

243 J. S. Yeon, T. H. Park, Y. H. Ko, P. Sivakumar, J. S. Kim, Y. Kim and H. S. Park, 2D spinel ZnCo_2O_4 microsheet-coated functional separator for promoted redox kinetics and inhibited polysulfide dissolution, *J. Energy Chem.*, 2021, **55**, 468–475.



244 F. Wu, J. Bai, J. Feng and S. Xiong, Porous mixed metal oxides: design, formation mechanism, and application in lithium-ion batteries, *Nanoscale*, 2015, **7**, 17211–17230.

245 H. Zhang, J. Liu, X. Lin, Y. Zhong, J. Ren, Z. Wang, T. Han and J. Li, A metal organic foam-derived zinc cobalt sulfide with improved binding energies towards polysulfides for lithium–sulfur batteries, *Ceram. Int.*, 2020, **46**, 14056–14063.

246 M. A. Rahman, X. Wang and C. Wen, High Energy Density Metal–Air Batteries: A Review, *J. Electrochem. Soc.*, 2013, **160**, A1759–A1771.

247 Q. Wang, L. Shang, R. Shi, X. Zhang, G. I. N. Waterhouse, L.-Z. Wu, C.-H. Tung and T. Zhang, 3D carbon nanoframe scaffold-immobilized Ni_3FeN nanoparticle electrocatalysts for rechargeable zinc–air batteries’ cathodes, *Nano Energy*, 2017, **40**, 382–389.

248 M. Dong, X. Liu, L. Jiang, Z. Zhu, Y. Shu, S. Chen, Y. Dou, P. Liu, H. Yin and H. Zhao, Cobalt-doped Mn_3O_4 nanocrystals embedded in graphene nanosheets as a high-performance bifunctional oxygen electrocatalyst for rechargeable Zn–Air batteries, *Green Energy Environ.*, 2020, **5**, 499–505.

249 Q. Wang, L. Shang, R. Shi, X. Zhang, Y. Zhao, G. I. N. Waterhouse, L.-Z. Wu, C.-H. Tung and T. Zhang, NiFe Layered Double Hydroxide Nanoparticles on Co,N-Codoped Carbon Nanoframes as Efficient Bifunctional Catalysts for Rechargeable Zinc–Air Batteries, *Adv. Energy Mater.*, 2017, **7**, 1700467.

250 Y. Huang, Y. Wang, C. Tang, J. Wang, Q. Zhang, Y. Wang and J. Zhang, Atomic Modulation and Structure Design of Carbons for Bifunctional Electrocatalysis in Metal–Air Batteries, *Adv. Mater.*, 2019, **31**, 1803800.

251 J.-C. Kim, G.-H. Lee, S. Lee, S.-I. Oh, Y. Kang and D.-W. Kim, Tailored Porous ZnCo_2O_4 Nanofibrous Electrocatalysts for Lithium–Oxygen Batteries, *Adv. Mater. Interfaces*, 2018, **5**, 1701234.

252 J. M. Costa, M. P. Clark, A. F. de Almeida Neto and D. G. Ivey, In-situ transformation of electrodeposited W–Co oxide to ZnCo_2O_4 nanoparticles as an effective bifunctional catalysts in Zn–air batteries, *Int. J. Hydrogen Energy*, 2020, **45**, 16122–16132.

253 Z. Mai, W. Duan, K. Wang, Z. Tang and S. Chen, Integrating ZnCo_2O_4 submicro/nanospheres with CoxSey nanosheets for the oxygen evolution reaction and zinc–air batteries, *Sustainable Energy Fuels*, 2020, **4**, 2184–2191.

254 N. Xu, Q. Nie, J. Liu, H. Huang, J. Qiao and X.-D. Zhou, Insert Zn^{2+} in Tetrahedral Sites of Bi-metal Zn–Co Spinel Oxides with High Oxygen Catalytic Performance for Liquid and Flexible Zinc–Air Batteries, *J. Electrochem. Soc.*, 2020, **167**, 050512.

255 L. Yan, Z. Xu, W. Hu, J. Ning, Y. Zhong and Y. Hu, Formation of sandwiched leaf-like CNTs–Co/ ZnCo_2O_4 @NC–CNTs nanohybrids for high-power-density rechargeable Zn–air batteries, *Nano Energy*, 2021, **82**, 105710.

256 Y.-P. Deng, Y. Jiang, D. Luo, J. Fu, R. Liang, S. Cheng, Z. Bai, Y. Liu, W. Lei, L. Yang, J. Zhu and Z. Chen, Hierarchical Porous Double-Shelled Electrocatalyst with Tailored Lattice Alkalinity toward Bifunctional Oxygen Reactions for Metal–Air Batteries, *ACS Energy Lett.*, 2017, **2**, 2706–2712.

257 W. Yan, X. Cao, J. Tian, C. Jin, K. Ke and R. Yang, Nitrogen/sulfur dual-doped 3D reduced graphene oxide networks-supported CoFe_2O_4 with enhanced electrocatalytic activities for oxygen reduction and evolution reactions, *Carbon*, 2016, **99**, 195–202.

258 T.-W. Chen, P. Kalimuthu, G. Anushya, S.-M. Chen, R. Ramachandran, V. Mariappan and D. C. Muthumala, High-Efficiency of Bi-Functional-Based Perovskite Nanocomposite for Oxygen Evolution and Oxygen Reduction Reaction: An Overview, *Materials*, 2021, **14**, 2976, DOI: [10.3390/ma14112976](https://doi.org/10.3390/ma14112976).

259 J. H. Li, M. Y. Liu, Y. Li, L. Yuan, P. Zhang, Z. Cai, H. Chen and J. L. Zou, ZIF-8@ZIF-67-derived ZnCo_2O_4 @nitrogen-doped carbon/carbon nanotubes wrapped by a carbon layer: a stable oxygen reduction catalyst with a competitive strength in acid media, *Mater. Today Energy*, 2021, **19**, 100574.

260 N. Tao, J. Liu, B. Wang, C. Liang, S. Lin, Y. Du, D. Fan, H. Yang, Y. Wang and K. Huang, Hydrothermal two-dimensionalisation to porous ZnCo_2O_4 nanosheets non-platinum ORR catalyst, *Micro Nano Lett.*, 2019, **14**, 665–668.

261 S. Chakrabarty, A. Mukherjee, W.-N. Su and S. Basu, Improved bi-functional ORR and OER catalytic activity of reduced graphene oxide supported ZnCo_2O_4 microsphere, *Int. J. Hydrogen Energy*, 2019, **44**, 1565–1578.

262 T. V. M. Sreekanth, P. C. Nagajyothi, K. C. Devarayapalli, J. Shim and K. Yoo, Lilac flower-shaped ZnCo_2O_4 electrocatalyst for efficient methanol oxidation and oxygen reduction reactions in an alkaline medium, *CrystEngComm*, 2020, **22**, 2849–2858.

263 Y. Liu, H. Jiang, J. Hao, Y. Liu, H. Shen, W. Li and J. Li, Metal–Organic Framework-Derived Reduced Graphene Oxide-Supported $\text{ZnO}/\text{ZnCo}_2\text{O}_4/\text{C}$ Hollow Nanocages as Cathode Catalysts for Aluminum– O_2 Batteries, *ACS Appl. Mater. Interfaces*, 2017, **9**, 31841–31852.

264 Y. Zheng, Y. Jiao, Y. Zhu, Q. Cai, A. Vasileff, L. H. Li, Y. Han, Y. Chen and S.-Z. Qiao, Molecule-Level $\text{g-C}_3\text{N}_4$ Coordinated Transition Metals as a New Class of Electrocatalysts for Oxygen Electrode Reactions, *J. Am. Chem. Soc.*, 2017, **139**, 3336–3339.

265 Y. P. Zhu, T. Y. Ma, M. Jaroniec and S. Z. Qiao, Self-Templating Synthesis of Hollow Co_3O_4 Microtube Arrays for Highly Efficient Water Electrolysis, *Angew. Chem., Int. Ed.*, 2017, **56**, 1324–1328.

266 J. Béjar, L. Álvarez-Contreras, J. Ledesma-García, N. Arjona and L. G. Arriaga, Electrocatalytic evaluation of Co_3O_4 and NiCo_2O_4 rosettes-like hierarchical spinel as bifunctional materials for oxygen evolution (OER) and reduction (ORR) reactions in alkaline media, *J. Electroanal. Chem.*, 2019, **847**, 113190.

267 J. Ge, W. Zhang, J. Tu, T. Xia, S. Chen and G. Xie, Suppressed Jahn–Teller Distortion in $\text{MnCo}_2\text{O}_4@\text{Ni}_2\text{P}$ Heterostructures to Promote the Overall Water Splitting, *Small*, 2020, **16**, 2001856.



268 Y. Tan, C. Wu, H. Lin, J. Li, B. Chi, J. Pu and L. Jian, Insight the effect of surface Co cations on the electrocatalytic oxygen evolution properties of cobaltite spinels, *Electrochim. Acta*, 2014, **121**, 183–187.

269 T. W. Kim, M. A. Woo, M. Regis and K.-S. Choi, Electrochemical Synthesis of Spinel Type $ZnCo_2O_4$ Electrodes for Use as Oxygen Evolution Reaction Catalysts, *J. Phys. Chem. Lett.*, 2014, **5**, 2370–2374.

270 K. Xiang, D. Wu, Y. Fan, W. You, D. Zhang, J.-L. Luo and X.-Z. Fu, Enhancing bifunctional electrodes of oxygen vacancy abundant $ZnCo_2O_4$ nanosheets for supercapacitor and oxygen evolution, *Chem. Eng. J.*, 2021, **425**, 130583.

271 S. Sun, Y. Sun, Y. Zhou, J. Shen, D. Mandler, R. Neumann and Z. J. Xu, Switch of the Rate-Determining Step of Water Oxidation by Spin-Selected Electron Transfer in Spinel Oxides, *Chem. Mater.*, 2019, **31**, 8106–8111.

272 D. Zhang, Z. Wang, J. Li, C. Hu, X. Zhang, B. Jiang, Z. Cao, J. Zhang and R. Zhang, MOF-derived $ZnCo_2O_4$ porous micro-rice with enhanced electro-catalytic activity for the oxygen evolution reaction and glucose oxidation, *RSC Adv.*, 2020, **10**, 9063–9069.

273 A. Amirzhanova, N. Akmanşen, I. Karakaya and Ö. Dag, Mesoporous $MnCo_2O_4$, $NiCo_2O_4$, and $ZnCo_2O_4$ Thin-Film Electrodes as Electrocatalysts for the Oxygen Evolution Reaction in Alkaline Solutions, *ACS Appl. Energy Mater.*, 2021, **4**, 2769–2785.

274 G. M. Tomboc, F. O. Agyemang and H. Kim, Improved electrocatalytic oxygen evolution reaction properties using PVP modified direct growth Co-based metal oxides electrocatalysts on nickel foam, *Electrochim. Acta*, 2018, **263**, 362–372.

275 D. Zhao, M. Dai, H. Liu, X. Zhu and X. Wu, PPy film anchored on $ZnCo_2O_4$ nanowires facilitating efficient bifunctional electrocatalysis, *Mater. Today Energy*, 2021, **20**, 100637.

276 J. Liu, Y. Xie, Y. Nan, G. Gou, X. Li, Y. Fang, X. Wang, Y. Tang, H. Yang and J. Ma, $ZnCo_2O_4$ nanoparticles derived from dual-metal-organic-frameworks embedded in Multi-walled Carbon Nanotubes: a favorable electrocatalyst for the water splitting, *Electrochim. Acta*, 2017, **257**, 233–242.

277 M. Dai, H. Liu, D. Zhao, X. Zhu, A. Umar, H. Algarni and X. Wu, Ni Foam Substrates Modified with a $ZnCo_2O_4$ Nanowire-Coated $Ni(OH)_2$ Nanosheet Electrode for Hybrid Capacitors and Electrocatalysts, *ACS Appl. Nano Mater.*, 2021, **4**, 5461–5468.

278 J. Pan, F. Wang, L. Zhang, S. Song and H. Zhang, Clean synthesis of $ZnCo_2O_4@ZnCo$ -LDHs yolk-shell nanospheres composed of ultra-thin nanosheets with enhanced electrocatalytic properties, *Inorg. Chem. Front.*, 2019, **6**, 220–225.

279 R. Que, S. Liu, Y. Yang and Y. Pan, High catalytic performance of core-shell structure $ZnCo_2O_4@NiFe$ LDH for oxygen evolution reaction, *Mater. Lett.*, 2021, **298**, 129982.

280 Z. Yu, Y. Bai, N. Zhang, W. Yang, J. Ma, Z. Wang, W. Sun, J. Qiao and K. Sun, Metal-organic framework-derived heterostructured $ZnCo_2O_4@FeOOH$ hollow polyhedrons for oxygen evolution reaction, *J. Alloys Compd.*, 2020, **832**, 155067.

281 H. Cheng, C.-Y. Su, Z.-Y. Tan, S.-Z. Tai and Z.-Q. Liu, Interacting $ZnCo_2O_4$ and Au nanodots on carbon nanotubes as highly efficient water oxidation electrocatalyst, *J. Power Sources*, 2017, **357**, 1–10.

282 T. Xiong, Z. Tan, Y. Mi, Q. Huang, Y. Tan, X. Yin and F. Hu, On-site generated metal organic framework-deriving core/shell $ZnCo_2O_4/ZnO$ nanoarray for better water oxidation, *Nanotechnology*, 2019, **30**, 495405.

283 C. Zhang, Y. Pan, C. Ouyang, X. Li, X. Quan, Z. Hong and M. Zhi, Template-Free Synthesis of Zinc Cobalt Oxides/Phosphides ($Co_2P/CoO/ZnCo_2O_4$) Hollow Sub-Micron Boxes as Hydrogen Evolution Reaction Catalysts, *ChemistrySelect*, 2021, **6**, 1685–1691.

284 S. Debata, S. Patra, S. Banerjee, R. Madhuri and P. K. Sharma, Controlled hydrothermal synthesis of graphene supported $NiCo_2O_4$ coral-like nanostructures: An efficient electrocatalyst for overall water splitting, *Appl. Surf. Sci.*, 2018, **449**, 203–212.

285 C. Shenghai, S. Liping, K. Fanhao, H. Lihua and Z. Hui, Carbon-coated $MnCo_2O_4$ nanowire as bifunctional oxygen catalysts for rechargeable Zn-air batteries, *J. Power Sources*, 2019, **430**, 25–31.

286 X. Jia, S. Gao, T. Liu, D. Li, P. Tang and Y. Feng, Controllable Synthesis and Bi-functional Electrocatalytic Performance towards Oxygen Electrode Reactions of Co_3O_4/N -RGO Composites, *Electrochim. Acta*, 2017, **226**, 104–112.

287 A. Rebekah, S. Anantharaj, C. Viswanthan and N. Ponpandian, Zn-substituted $MnCo_2O_4$ nanostructure anchored over rGO for boosting the electrocatalytic performance towards methanol oxidation and oxygen evolution reaction (OER), *Int. J. Hydrogen Energy*, 2020, **45**, 14713–14727.

288 D. Tang, Y. Han, W. Ji, S. Qiao, X. Zhou, R. Liu, X. Han, H. Huang, Y. Liu and Z. Kang, A high-performance reduced graphene oxide/ $ZnCo$ layered double hydroxide electrocatalyst for efficient water oxidation, *Dalton Trans.*, 2014, **43**, 15119–15125.

289 J. M. Gonçalves, P. R. Martins, L. Angnes and K. Araki, Recent advances in ternary layered double hydroxide electrocatalysts for the oxygen evolution reaction, *New J. Chem.*, 2020, **44**, 9981–9997.

290 J. P. Kumar, S. D. Giri and A. Sarkar, Mesoporous NiO with different morphology: Synthesis, characterization and their evaluation for oxygen evolution reaction, *Int. J. Hydrogen Energy*, 2018, **43**, 15639–15649.

291 M. Kashif, M. Fiaz and M. Athar, One-step hydrothermal synthesis of ZnO nanorods as efficient oxygen evolution reaction catalyst, *Inorg. Nano-Met. Chem.*, 2022, **52**, 101–107.

292 N. Kim, D. Lim, Y. Choi, S. E. Shim and S.-H. Baeck, Hexagonal β - $Ni(OH)_2$ nanoplates with oxygen vacancies as efficient catalysts for the oxygen evolution reaction, *Electrochim. Acta*, 2019, **324**, 134868.

293 X. Du, Z. Yang, Y. Li, Y. Gong and M. Zhao, Controlled synthesis of $Ni(OH)_2/Ni_3S_2$ hybrid nanosheet arrays as



highly active and stable electrocatalysts for water splitting, *J. Mater. Chem. A*, 2018, **6**, 6938–6946.

294 M. I. da Silva, I. R. Machado, H. E. Toma, K. Araki, L. Angnes and J. M. Gonçalves, Recent progress in water-splitting and supercapacitor electrode materials based on MOF-derived sulfides, *J. Mater. Chem. A*, 2022, **10**, 430–474.

295 L. Zhang, Q. Fan, K. Li, S. Zhang and X. Ma, First-row transition metal oxide oxygen evolution electrocatalysts: regulation strategies and mechanistic understandings, *Sustainable Energy Fuels*, 2020, **4**, 5417–5432.

296 T. G. Ritter, A. H. Phakatkar, M. G. Rasul, M. T. Saray, L. V. Sorokina, T. Shokuhfar, J. M. Gonçalves and R. Shahbazian-Yassar, Electrochemical synthesis of high entropy hydroxides and oxides boosted by hydrogen evolution reaction, *Cell Rep. Phys. Sci.*, 2022, **3**, 100847.

297 L. Yu, T. Liu, R. Amine, J. Wen, J. Lu and K. Amine, High Nickel and No Cobalt—The Pursuit of Next-Generation Layered Oxide Cathodes, *ACS Appl. Mater. Interfaces*, 2022, **14**(20), 23056–23065, DOI: [10.1021/acsmami.1c22091](https://doi.org/10.1021/acsmami.1c22091).

298 J. M. Gonçalves, P. Roberto Martins, D. P. Rocha, T. A. Matias, M. S. Julião, R. A. Abarza Munoz and L. Angnes, Recent trends and perspectives in electrochemical sensors based on MOF-derived materials, *J. Mater. Chem. C*, 2021, **9**(28), 8718–8745, DOI: [10.1039/d1tc02025k](https://doi.org/10.1039/d1tc02025k).

